Photolithographic micro-structuring of artificial 3-dimensional hydrogel environments for cell migration studies

Miriam Balles

München 2018

Photolithographic micro-structuring of artificial 3-dimensional hydrogel environments for cell migration studies

Miriam Balles

Dissertation
an der Fakultät für Physik
der Ludwig–Maximilians–Universität
München

vorgelegt von
Miriam Balles, geb. Dietrich
aus Miltenberg

München, den 27.09.2018

Erstgutachter: Prof. Dr. Joachim O. Rädler

Zweitgutachter: Prof. Dr. Chase P. Broedersz

Tag der mündlichen Prüfung: 30.11.2018

Zusammenfassung

Die extrazelluläre Matrix (ECM) der Zellen *in vivo* besteht aus einer komplizierten Biopolymermischung, die Netzwerke mit unterschiedlicher Steifigkeit und Maschenweite bildet und Signalmoleküle in gelöster sowie matrixgebundener Form enthält. Aufgrund dieser Komplexität ist noch nicht vollständig verstanden welche Faktoren die Zellmigration in solchen Netzwerken beeinflussen. Um die Untersuchung von chemotaktischen und durotaktischen Migrationsmechanismen zu erleichtern werden künstliche ECM Nachbildungen, deren Eigenschaften und Zusammensetzung genau bestimmt werden können, benötigt.

In dieser Doktorarbeit wurden photo-polymerisierbare, synthetische Hydrogelmikrostrukturen entwickelt um eine auf die wesentlichen Bestandteile reduzierte ECM nachzubilden. Vierarmige Polyethylenglykol (PEG) Monomere wurden entweder mit linearen PEG Molekülen vernetzt, wodurch nicht-migrierbare Netzwerke entstehen, oder mit einem Vernetzer bestehend aus einem Peptid, welches durch Matrix-Metalloproteinasen (MMPs) gespalten werden kann und so die proteolytische Zellmigration in dem Gel ermöglicht. Der Zusatz eines kleinen Peptids, welches eine RGD-Sequenze enthält, vermittelt die Zelladhäsion an das ansonsten bioinerte PEG Netzwerk. Die biokompatible Polymerisation, welche durch kurze Belichtung mit UV Licht induziert wird, erlaubt den Einschluss von lebenden Zellen in das Gel. Durch Photolithographie können außerdem kleine Gelstrukturen in Kanalsystemen hergestellt werden.

Um das Hydrogelsystem und seine Quelleigenschaften genau zu charakterisieren wurden "Particle Image Velocimetry"(PIV) Analysen durchgeführt. Die Deformationsfelder zeigen ein anisotropes Quellen des Gels aufgrund der Begrenzung in einem Kanal. Im mittleren Bereich der Struktur quillt der dünne Streifen nur in Richtung der Streifenbreite. Durch Veränderung des Lösungsmittels und Quellmediums, der Art und Menge des verwendeten Vernetzers, sowie der Kanalhöhe und anfänglichen Streifenbreite, kann die Stärke des natürlichen Quellens beeinflusst werden.

Um zu untersuchen wie Zellen affine Deformationen in ihrer Umgebung wahrnehmen und darauf reagieren, wurden mikrostrukturierte, künstliche Hydrogele genutzt um gedehnte, zersetzbare Netzwerke herzustellen. Das zuvor erwähnte anisotrope Quellen führt zu einem monoaxial gedehnten Hydrogelstreifen. Die Untersuchung der Zellmigration von HT-1080 Zellen in solchen Strukturen zeigt eine bevorzugte Migration entlang der Quellrichtung. Für mittlere Dehnungsstärken ist diese Ausrichtung maxi-

mal. Um den Zusammenhang zwischen der Migrationsrichtung und der Dehnung zu verstehen wurde im Rahmen einer Kooperation ein theoretisches Model realisiert. Die Simulation einer proteolytischen, durotaktischen Zellmigration auf einem 2D Gitter ergab die selbe nicht-monotone Reaktion auf die monoaxialen Dehnung, die auch in den Experimenten beobachtet wurde. Untersuchungen der Steifigkeit innerhalb des Modells zeigten eine anisotrope Versteifung der Matrix unter Dehnung, was der Grund für das anisotrope Zellverhalten ist. Durch offenlegen dieses grundlegenden Mechanismus der Zellorientierung in gedehnten, makroskopisch linear elastischen Netzwerken, wurde gezeigt, dass die Dehnungsversteifung auf der mikroskopischen Ebene entscheidend für das Zellverhalten ist.

Das natürliche Quellen der Mikrostrukturen wurde desweiteren dafür genutzt unter Druck stehende Hydrogel-Hydrogel Grenzflächen, sogenannte "sponge clamps", herzustellen, um ein System zu etablieren mit dem Proteolyse-unabhängige Zellmigration in vordefinierten Spalten untersucht werden kann. Das Quellen paralleler Streifen füllt den Raum zwischen den Strukturen und bildet dadurch einen unter Druck stehenden Spalt in einem passivierten Kanalsystem. Durch Veränderung des Abstands zwischen den Streifen und der verwendeten Gelzusammensetzung kann die Gelkompression in dem System eingestellt werden. Dadurch wird die Eindringeffizienz der Krebszellen beeinflusst. Der anfängliche Streifenabstand, aber auch die Matrixsteifigkeit sind entscheidende Regulatoren für die Zellmigration in den Spalten.

Die Ergebnisse dieser Doktorarbeit zeigen, wie photostrukturierbare artifizielle ECMs und ihr natürliches Quellverhalten dazu genutzt werden können, fortschrittliche 3D Systeme zur Migrationsanalyse herzustellen um grundlegende Einflussfaktoren in der proteolytischen und nicht-proteolytischen Tumorzellmigration aufzudecken.

Summary

The extracellular matrix (ECM) of cells *in vivo* is a complex mixture of biopolymers that form a network of varying stiffness and mesh sizes, containing soluble and matrix bound signaling molecules. Due to this complexity, it is not fully understood which cues guide cell migration in such networks. To facilitate the analysis of chemotactic or durotactic migration mechanisms, artificial ECM mimics, whose properties and composition can be fine-tuned, are needed.

In this thesis photo-polymerizable, synthetic hydrogel micro-structures were developed to mimic a minimal ECM for cell migration studies. 4-armed polyethylene glycol (PEG) monomers were cross-linked with either linear PEG molecules, which results in a non-degradable network, or with a peptide cross-linker which can be cleaved by matrix-metalloproteinases (MMPs) and allows the proteolytic cell migration within the gel. Addition of a small RGD-containing peptide sequence mediates cell adhesion to the otherwise bioinert PEG network. The biocompatible polymerization induced by short illumination with UV light permits the direct encapsulation of living cells and the micro-structuring of small gel strips inside channel systems using photo-lithography.

To carefully characterize the hydrogel system and its swelling properties, particle image velocimetry (PIV) was used. The obtained displacement fields show an anisotropic swelling of the gel due to the confinement in a channel. In the longitudinal middle section, the thin strips swell only in the direction of the strip width. The magnitude of the inherent gel swelling can be tuned by changing the solvent and swelling media, the type and amount of cross-linker used for the polymerization, as well as the dimensions of the channel and strip.

To study how cells perceive and react to affine deformations in their surroundings, a micro-structured artificial hydrogel was used to form a strained, degradable matrix. The aforementioned anisotropic swelling uniaxially strained the gel strips. Analysis of HT-1080 cell migration in such structures showed a preferred migration parallel to the swelling direction, with a maximal alignment at intermediate strain levels. To understand the relationship between cell migration directionality and strain, a theoretical model was implemented within the framework of a collaboration. With the simulation of a proteolytic, durotactic cell movement on a 2D lattice, the same non-monotonic response to uniaxial strain as seen in the experiments was obtained. Stiffness analysis within the model showed an anisotropic stiffening of the matrix upon strain, which

leads to the anisotropic cell migration. The unraveling of this fundamental mechanism as cell guidance cue in strained networks of macroscopically linear elastic materials demonstrates that strain stiffening on the microscopic scale is crucial for the cell behavior.

The inherent swelling of the gel micro-structures was furthermore used to create pressurized hydrogel-hydrogel interfaces, so called sponge clamps, to establish an assay for analyzing non-proteolytic cell migration into predefined clefts. The swelling of parallel hydrogel strips fills the space in between the structures and thereby generates pressurized clefts inside a passivated channel system. By varying the gap size as well as the gel composition, the gel compression in the system can be tuned, which influences the invasion efficiency of cancer cells. Initial strip distance, but also matrix stiffness are key regulators of cell migration in the clefts.

The results of this thesis illustrate how photo-structurable artificial ECM mimics and their inherent swelling enable the generation of advanced 3D migration assays to unravel fundamental guidance cues in proteolytic and non-proteolytic cancer cell migration.

Contents

1. Introduction

Cancer invasion and metastasis are cellular migration events that are life threatening for the affected organism [1]. In cancer metastasis cells leave the primary tumor site and penetrate the neighboring extracellular space. They eventually encounter blood and lymphatic vessels, which they invade. Thereby they reach distant sites where they form secondary tumors. In the process, cells encounter a variety of extracellular matrix (ECM) proteins, growth factors, other cells, and higher ordered structures like nerve bundles that influence and guide cell movement [2, 3]. The extracellular space is not a static construct, but is constantly remodeled by embedded cells. For example, in the vicinity of a tumor the behavior of stromal cells, including fibroblasts and macrophages, is altered by signals released by the tumor cells. Theses activated stromal cells thereafter remodel the ECM, secrete or release growth factors and thereby influence the behavior of the cancer cells. This results in a highly dynamic cycle of guidance mechanisms inducing and facilitating tumor growth and cancer cell invasion into the ECM [4–6]. Analyzing and understanding how these different factors interact and which guidance cues are important in cell migration is therefore a crucial task in cancer research.

Cell migration is also important in non-malignant processes in multicellular organisms, including leukocyte movement in immune response and the growth of neuronal axons in embryogenesis [7–10]. Chemotaxis, the directed movement of cells towards a chemical stimuli, was already observed for leukocytes in the mid 19th century and is a very well studied cell guidance mechanism [11, 12]. Other guidance cues, including matrix bound growth factors, aligned fibers in a matrix, or the stiffness of the matrix are further parameters that influence cell migration, but are less well understood than chemotaxis. Often, these factors interplay to orchestrate the movement of cells, as was already demonstrated almost 100 years ago for axon growth *in vitro* [13].

To analyze such guidance and understand the underlaying mechanisms of cell migration, suitable model systems have to be established. 2D set-ups on coated glass or plastic surfaces are often used due to their relatively low complexity. Micro-structuring of such substrates to examine single cell behavior and thereby increase the statistics is one important development that not only facilitates the migration analysis but can also help to unravel migration mechanisms [14–17]. However, most cells *in vivo* are embedded in a 3D matrix and do not migrate in a 2D environment. They receive

signals all around the cell surface, can interact with a substrate to all sites, and encounter constrictions or aligned fibers within the matrix. This ultimately influences cell migration in a way that cannot be reflected in 2D experiments, which explains discrepancies observed between 2D and 3D assays [18]. Fibroblasts in 2D, for example, show a flat morphology, whereas cultures in 3D have a more rounded or spindle like phenotype. Furthermore, the conclusion drawn from 2D experiments that cells tend to move towards stiffer substrates [19] might not hold completely true for 3D scenarios, where macroscopically stiffer matrices most often also consist of denser networks [20]. A denser substrate, however, hampers migration.

Culturing cells within naturally derived gels, like collagen or Matrigel, increases the complexity of the model system and is closer to *in vivo* conditions compared to 2D experiments, but also complicates the analysis and the interpretation of the results. Naturally derived matrices are non-linear elastic and have a heterogeneous network structure with varying mesh sizes and formed fibers [21, 22]. In the case of Matrigel, they also have an undefined composition, including an unknown multitude of growth factors, which might alter cell behavior [23]. Therefore, to reduce the complexity of 3D models and facilitate the interpretation of study results, artificial hydrogels are used as culture matrices in many 3D experiments [24, 25].

Artificial matrices can be formed from different materials, ranging from self-assembled peptide gels [26], electrospun fiber networks [27, 28], to highly cross-linked matrices [29]. Often, the backbone of the gels is bioinert, thereby controlling cell-matrix interactions through the incorporation of small peptide sequences into the matrix. This not only enables the study of adhesion ligand density on cell behavior independent of the overall matrix structure, but also the test of peptide libraries to identify the best ligands for cell adhesion or matrix digestion [30–32]. Especially polyethylen glycol (PEG) is intensively used as matrix material due to its highly bioinert properties. In comparison to peptide gels or electronspun fibers, highly cross-linked gels have a very small mesh size, which impedes the non-proteolytic migration of embedded cells [33, 34]. Thus, suitable cleavage sites have to be incorporated in these matrices to enable cell migration. Most often, peptide sequences derived from collagen, which can be cleaved by matrix metalloproteinases (MMPs) are used as cross-linkers in such gels [35, 36].

A further advantage of artificial gels is that many different mechanisms can be used to form the networks. Naturally derived matrices mostly gel after changing the temperature or pH of the solution, whereas covalently cross-linked synthetic gels can additionally be polymerized by illumination or by addition of a cross-linker. The photo-induced polymerization bears the advantage that the reaction can be controlled temporally as well as spatially. Hence, the geometry of the formed gel can be varied. Moreover, if the reaction is very fast, which can be achieved by using a radically induced polymerization in combination with a suitable light source, embedded cells are evenly distributed in

the gel. In temperature induced gelation, cells might sink to the bottom of the gel due to the relatively long gelation times. Photo-induced polymerization of artificial ECMs can be used to form more complex matrix structures compared to other techniques [37, 38]. Therefore, it provides the opportunity to combine defined matrix properties with the simulation of advanced migration structures *in vitro*.

Consequently, this thesis concentrates on two main tasks. As a first step, photo-polymerizable artificial matrix mimics were established to easily create advanced migration matrices. The implemented set-ups were subsequently used to systematically analyze the guided migration and invasion of cancer cells in 3D environments. Hence, this work is structured as following:

In **chapter 2**, the fundamental principles of cell migration are described and a short overview of systems used for migration studies is given, with a special emphasis on cross-linked artificial matrices. To understand cell migration, the cytoskeleton and the extracellular matrix (ECM) are described followed by different modes of migration and cell guidance. Afterwards, 2D and 3D set-ups formed from synthetic and naturally derived hydrogels are discussed. A closer look at photo-structurable gels and their inherent swelling behavior completes this chapter.

Chapter 3 introduces the modular hydrogel set-up established in this work. The monomers used to form the hydrogel are described together with an explanation of the photo-induced polymerization procedure inside channel slides.

Before using the established system to form advanced migration assays, the hydrogel is carefully characterized in **chapter 4**. The inherent swelling of thin hydrogel micro-structures inside the channels was characterized by particle image velocimetry (PIV) analysis to visualize and quantify the magnitude of swelling. Swelling in the longitudinal middle section of the strip is anisotropic and only deforms the gel in the direction of the strip width. The swelling magnitude can be tuned by changing the composition of the gel, the dimensions of the strip and channel, as well as the solvent and swelling media used when forming the gels. By changing the cross-linker ratio in the gel also the stiffness of the gels change. To ensure high survival rates of cells in the gel, live-dead staining of embedded cells was performed and yielded very good results for low monomer concentrations.

In **chapter 5**, the guidance mechanism of cell migration in strained synthetic hydrogels is identified. The anisotropic swelling of thin hydrogel strips in channel slides was used to form uniaxially strained environments. Cell migration in such gels is anisotropic with the main migration direction depending non-monotonically on the strain magnitude. In the framework of a collaboration, a theoretical model of a durotactic, proteolytic active cell was implemented and validated against experimental data. The simulation shows very similar migration behavior to the experiments. Within the model, the cell migration direction only depends on the local matrix stiffness, which increases

anisotropically with increasing strain.
In **chapter 6**, the inherent swelling of micro-structured hydrogel strips in channels is used to analyze cell invasion into pressurized gel clefts. Parallel structuring of strips in close proximity, together with the swelling of hydrogel strips after polymerization forms so called sponge clamps, pressurized hydrogel-hydrogel clefts. Depending on the used cross-linker ratio in the gel and the initial strip to strip distance before swelling, gels are compressed to different degrees. This set-up was used to perform proof-of-concept experiments with two cancer cell lines. The invasion of these cells into the pressurized clefts depends on the gel compression and the cross-linker ratio used to form the gels.
An outlook is given in **chapter 7**, where variations and future applications of the modular hydrogel in general and the established set-ups in particular are exemplified.
A detailed description of the methods used in this work is given in **appendix A**.

2. Basic Concepts

2.1. Cell migration is a highly complex process guided by the interplay of the cell with its environment

Cell migration plays a pivotal role in many biological processes, starting from embryogenesis, where cells move to form higher structural entities, like the nervous system [10, 39], to daily mechanisms like immune response and wound healing [8, 40], up to disease states in e.g. malignant tumor environments [1, 41]. Consequently, understanding how cells migrate, which components influence migration and how all of this plays together to guide migration is a crucial task in many scientific disciplines. In the following, the main components involved in migration in the cell and its surrounding are presented, followed by a closer look at different modes of cell migration as well as guidance mechanisms.

2.1.1. Cytoskeleton and adhesion machinery

The cytoskeleton of cells is a highly dynamic network of different polymers and fibers which in large parts is responsible for the shape and mechanical stability of a cell. Furthermore, it helps to organize the content of a cell and the ordered transport of molecules in the cytoplasm, enables the connection of the cell to the surrounding, and can generate forces necessary to change the cell shape and move the cell [42]. The cytoskeleton mainly consists of three different polymers: microtubules, actin filaments, and intermediate filaments (see figure 2.1). Microtubules as well as actin polymers have a polarized structure, with two distinct ends where a dynamic polymerization and depolymerization of the structures occurs. This not only enables the directed transport of small molecules along the fibers by motor proteins like myosins along actin filaments or kinesins along microtubules, but also helps to coordinate force generation in the cell by directed extension of the polymers in the migration direction [43, 44].
Microtubules are the stiffest of the three polymers and are important in cell division, where they form the spindle apparatus, and in cell migration, helping to maintain the cell polarization and actin assembly [45, 46]. The intermediate filaments are a group of polymers that can be cross-linked to each other, but also to actin filaments and microtubules. They are softer than the other cytoskeleton polymers and can be

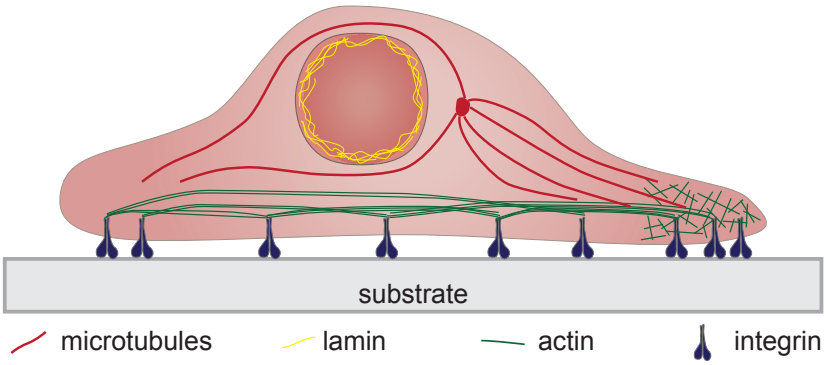

Figure 2.1.: Schematic of the most important cytoskeletal components. The cytoskeleton is mainly composed of microtubules (red fibers), intermediate filaments like lamin (yellow fibers), and actin (green fibers). The cytoskeleton is linked to the extracellular space through adhesions mediated by e.g. integrins.

stretched up to several times of their original length [47–49]. Examples are among others keratins or vimentins. Nuclear lamins are intermediate filaments as well and are responsible for the structural integrity and stiffness of the nucleus. Therefore, they are especially relevant for cell migration through small pores and in constrictions, as there, the nucleus as most rigid cell organelle is the limiting factor for cell movement [50–53].

Actin structures in the cell are continuously polymerized and depolymerized, making it a highly dynamic structure. The actin assembly on the leading edge of cells can lead to rather diverse structures. In lamellipodia the actin fibers are highly branched forming an actin-rich network. In filopodia actin bundles are formed to increase the stiffness of the structures [54–56]. With myosin motors acting on actin fibers, the cell can contract its cytoskeleton [57, 58]. However, to be able to interact with the cell environment as well as to perceive matrix stiffness and tensions, actin has to be coupled to the extracellular matrix (ECM) by an adhesion machinery [59–61].

One of the most important groups of molecules that mediate between the cell environment and the cytoskeleton are integrins. These transmembrane proteins consist of two subunits, an α and a β chain, which determine the integrin-ligand interactions. Depending on the combination of different α and β chains, ECM proteins can be bound or even cell-cell interactions can be built. Among others, fibronectin, which contains a RGD peptide sequence that is important for many integrins, can be bound, as well as collagen or laminin [59, 62, 63]. A stable binding of multiple integrins to the ECM and thereafter recruitment of many molecules important for the adhesion machinery, bigger adhesion clusters, so called focal adhesions, are built that stably connect the cell environment to the cell cytoskeleton. This not only enables the adhesion of cells, but also provides a possibility for signaling. Integrins are considered key players in mechanotransduction, the conversion of mechanical information from the cell environment into internal cell stimuli [64, 65]. Together with other signaling receptors, which

e.g. detect soluble growth factor gradients, integrins are crucial in the guidance of directed cell migration.

2.1.2. Extracellular matrix composition

Cells in the body are not only surrounded by other cells but reside in an ECM composed of a variety of different polymers and smaller molecules that interact and influence cell behavior (see figure 2.2). The ECM is not a static mixture but a highly dynamic composition of mainly two classes of macromolecules: proteoglycans and fibrous proteins [66–68]. They are produced by cells and exocytosed into the extracellular space, where they can be remodeled, modified or degraded by cells. Therefore, cells are constantly shaping and changing the composition and organization of their own ECM. Even though the fundamental components of the ECM are mainly the same for different organs and tissues, the composition and thereby the properties vary widely from e.g. very stiff bone tissue to soft brain mass.

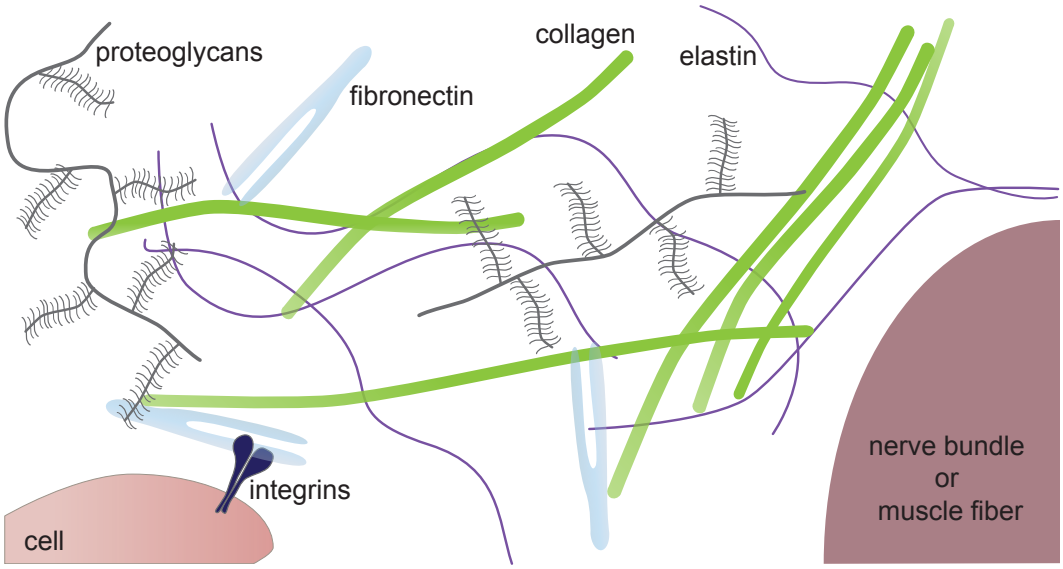

Figure 2.2.: Schematic overview of the main components of the extracellular matrix. The ECM is a mixture of different fiber proteins (e.g. fibronectin, collagens or elastin) in a hydrogel formed by proteoglycans. The exact composition of the ECM is different for distinct tissues. Proteins are not homogeneously distributed in the matrix and can be reorganized by the residing cells, e.g. collagen fibers can be aligned to form bigger bundles. Furthermore, higher ordered structures like nerve bundles or muscle fibers are part of the extracellular space and can play an important role in cell migration.

The most abundant proteins in the ECM and the human body in general are the fiber proteins of the collagen family. Over 25 different collagen types are identified that can be grouped according to their overall structure, from fibrillar collagens as collagen I to short chain collagen VIII. Collagens can build higher ordered structures. Most collagens start from three single chains that form the triple helical tropocollagen, which aggregates into supramolecular complexes like long collagen micro-fibrils. By

exerting a force on collagen fibrils, cells are able to further arrange collagen to form thicker bundles. In the basal membrane, however, other collagens, like collagen IV, form network structures rather than long fibers [69, 70]. Furthermore, collagens can be digested by various collagenases and matrix metalloproteinases (MMPs). MMPs play a pivotal role in proteolytic cell migration by digesting collagens, remodeling the matrix and opening up space for the cell body displacement [71, 72].

Another macromolecule, elastin, is a very elastic fibrous protein in the ECM. It forms highly cross-linked networks and associates with collagen fibers. This combination is crucial for the mechanical integrity of the ECM. Due to elastin, a matrix can be stretched to a very high extent without breakage and recoils upon release of the tension. Elastin thereby is responsible for the elastic part, whereas the collagen fibers limit the extension of the matrix to ensure matrix integrity [73, 74].

Fibronectin, a very important fibrous protein in the ECM, can also be elongated far beyond its rest length by forces exerted by cells. Thereby, cryptic integrin binding sites are exposed, which is why fibronectin is assumed to be one key player in extracellular mechanoregulation [75, 76]. Besides the already mentioned binding site for cellular interaction via integrins, fibronectin has a variety of binding sites for various other ECM components.

These and more fibrous polymers are embedded in the ECM in a network of proteoglycans, the second major component of the extracellular space. This very heterogeneous group of molecules all have a highly glycosylated protein structure and are divided in different groups according to their glycosamyloglycan (GAG) side chains [77]. Due to the GAG chains, all these macromolecules are negatively charged and highly hydrophilic and thus form a hydrogel that yields the embedded cells from strong compressions. Furthermore, the hydrophilic nature of the polymers and distinct binding sites present in the protein backbone enable the proteoglycan network to store growth factors secreted by cells. It is therefore a reservoir for small molecules which can be released upon specific stimuli or matrix degradation and thereby influence cell migration [78–80]. Thus, a lot of cell secreted growth factors and signaling molecules are not available to the cells in their soluble form, but rather in a matrix associated construct.

The extracellular space is not completely composed of a homogeneous network of ECM, but rather consists of networks of pores or fiber bundles which can be used by cells as migration tracks. Furthermore, higher structures, like vessels or nerve bundles are embedded in the ECM and provide a quasi 2D surface. On inner body surfaces that are covered with endothelial or epithelial cells, cell migration depends more on cell-cell rather than cell-matrix interactions. Along basement membrane interfaces small gaps and cell tracks are present which can be used for cell movement along nerve tracks or adipocytes. At these interfaces, no or only very little matrix remodeling is necessary for cell migration in contrast to a migration through dense fiber networks [81, 82].

In summary, the ECM is not just a network of fibers where cells reside, but a highly complex collection of macromolecules, small growth factors, and higher ordered structures that interplay and change over time. The interaction between different ECM components and the cells is crucial for cell function and strongly influences cell behavior.

2.1.3. Different modes of cell migration

The variety of ECM structures encountered by cells strongly affects cell migration. Depending on the cell and its environment, different migration strategies are possible. In general, one can distinguish between single and collective cell migration, where a cell either moves independently and spatially separated from other cells or together, in contact with neighboring cells [2]. In the following, different modes of migration and how they are influenced or triggered by the cell environment are described.

Single cell migration on a 2D surface can be divided in five basic steps (see figure 2.3) [43]. First, the cell has to polarize by establishing spatially asymmetric concentrations of e.g. signaling receptors, integrins, and cytoskeleton components. The cell develops a polarized morphology with a distinguishable leading edge and cell rear. Furthermore, microtubules are polarized towards the front, which further enhances and stabilizes the cell polarization due to the directed transport of intracellular molecules along the microtubule fibers. Thereby, new membrane extensions in the form of lamellipodia and filopodia are formed at the leading edge, as actin polymerization is strongly enhanced towards the cell front. The newly formed protrusions next start to interact with their surrounding and couple the cytoskeleton to the ECM. Through the established links, often formed by integrins that cluster to mature focal adhesions, mechanosensing and force generation can be established. With the motor protein myosin acting on the actin skeleton, tension is built in the cell [58]. As a last step, the adhesions at the trailing edge of the cell are dissociated and the cell body moves towards the cell front, resulting in a displacement of the whole cell.

If a cell is embedded in a 3D environment rather than on a flat 2D substrate, and the surrounding ECM network is dense, additional steps are necessary to enable cell displacement. As already mentioned in the previous chapter, cells can remodel the ECM. If the network pores are to small for the cell to squeeze through, matrix proteolysis by MMPs or other proteases opens migration tracks by cleaving fiber proteins like collagen or fibronectin (see figure 2.3 step 3a). This cleavage is located slightly rearward from the leading edge to ensure a spatial separation from force generation at the cell front and the matrix breakdown slightly behind [83].

The polarized, adhesion-mediated 3D cell migration, where cells digest the matrix to move through the ECM is called the mesenchymal migration mode of single cells. Such

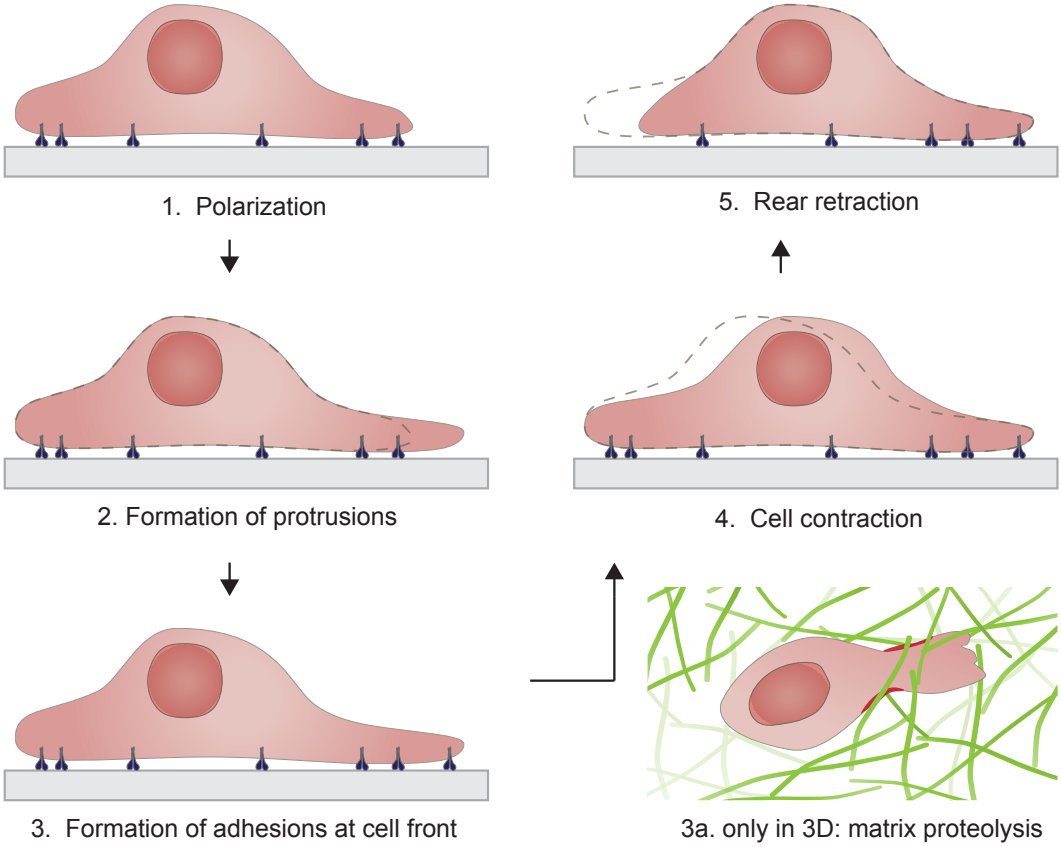

Figure 2.3.: Basic steps of cell migration. The migration process of a cell is generally divided in five steps. (1) Cells have to polarize by anisotropic distribution of cytoskeleton components in the cell to (2) form a protrusion in the direction of movement. Upon (3) the formation of new adhesion sites at the cell front, cells can (4) contract their cytoskeleton and (5) after deletion of adhesions at the cell rear, the cell body displaces. In a 3D environment, an additional matrix proteolysis step (step 3a) is necessary if the surrounding is to dense for the cell to displace.

cells adopt an elongated, spindle shaped morphology and remodel their matrix, leaving migration tracks behind, which can be used by other following cells. Sometimes cells cannot digest the matrix because the network itself is non-degradable or because the cells lack the ability to cleave the network components. If the mesh sizes or gaps in these matrices are very small, cells get stuck in the matrix. However, if the spacing in the ECM is big enough for cells to squeeze through the network, an amoeboid migration can be adapted by some cells [81]. Here cells have a rounded morphology, but can strongly deform to squeeze through the matrix. If the cells are able to form weak adhesions and exert small forces, they form small filopodia that interact with the network. If no adhesions can be formed between the matrix and the cell, blebs and lateral intercalation mediate the translocation of the cell body, resulting in a blebbing motion driven by the cortical actomyosin contractility [84]. Depending on the matrix encountered, a lot of cancer cells are able to switch their mode of migration to ensure an invasion into distant locations. Furthermore, cells were shown to switch their mirgation

mode due to changed external stimuli, either secreted from their microenvironment or induced by e.g. a chemotherapeutic agent [85–88].

Rather than migrating as single cells, small groups or whole sheets of cells can migrate as a collective. This is only possible, if cell-cell interactions via adhesion molecules are established, which couple the cells together. Collective migration is important in processes like wound healing or morphogenesis and also cancer cells often migrate as connected cell clusters and streams along matrix structures with leading cells guiding the collective [89, 90]. As described before for the transition between different single cell migration modes, cells can also lose their cell-cell contacts and change from collective migration to single cell migration in cancer metastasis [81, 91]. An invasive cancer will most probably not only show one distinct migration mode, but the invading cells will adapt their migration behavior depending on the encountered barriers of the ECM and the received external stimuli.

2.1.4. Guidance mechanisms in cell migration

The composition of the matrix does not only influence the mode of cell migration, but can also guide migration in a distinct direction. This is the case in many processes like embryogenesis or metastasis, cancer cell migration towards vessels, where specific guidance cues are anisotropically distributed in the cell environment.

One guidance mechanism already indirectly mentioned in the previous section is contact guidance along topological structures like collagen fibers, nerve bundles, or artificially structured surfaces in *in vitro* experiments containing grooves or pillars [82, 92, 93]. Cancer cells *in vivo* often use preexisting structures to escape from their primary site. However, this is not pure contact guidance, as often along these structures ECM density is lower or zero, which further facilitates cell migration in 3D. In *in vitro* experiments grooves perpendicular to a wound increase the wound closure without the need for cell adhesion to the structures and tilted pillars polarized and guided the movement of normal human dermal fibroblasts [94, 95].

The stiffness of the encountered matrix can guide cell migration as well, a mechanism called durotaxis. Lo et al. were the first to describe the phenomenon of single cells migrating from a soft surface towards a stiffer substrate of the same adhesion properties [19]. Many other followed and describe the behavior of cells on different stiffness gradients [12]. The steepness of the gradient and the overall stiffness is thereby critical for effective cell guidance [96, 97]. The exact mechanism of how the stiffness of the surrounding is processed after the cell couples to the substrate through its mechanosensitive adhesion machinery is still under debate [12]. It is believed that cells pull on their surrounding and perceive the induced deformation and thereby determine the substrate rigidity. It is possible that the mechanical information is then processed into chemical

signaling inside the cell which directs cell migration. In durotaxis, also a direct transfer of stiffness to directed movement is possible when the cell pulls on the substrate and the stiffer matrix is deformed less. This can directly result in a net movement from soft towards stiff regions.
If the concentration of signaling molecules guides cell migration it is called haptotaxis or chemotaxis, depending on if the molecules are matrix bound or soluble. In haptotaxis not only matrix bound growth factors or signaling molecules guide migration but also the concentration of adhesion linkers provided by e.g. collagen or fibronectin or receptors presented by neighboring cells are important [98–100]. Major processes in an organism including embryogenesis, immune response and cancer metastasis are well studied concerning the role of chemotactic guidance. Many signaling pathways have been identified that transform the concentration gradient of signaling molecules first sensed by cell-surface receptors into a polarization of the cells in the direction of higher chemoattractant concentration [101–103].
When thinking about guidance in cell migration one has to consider that seldom only one mechanism is likely to act on its own, but rather different guidance cues influence the cell behavior. In cancer cell migration, soluble chemotactic gradients can guide the migration direction, however, preexisting structures like nerve bundles or protein fibers in the ECM will influence the cell movement as well. Another example is the guidance of axons in embryogenesis. There, the growth cone not only is directed by chemical signals, both attractive and repulsive, but also by the mechanics of the matrix. Together these signals orchestrate the directed growth of the axons to their designated destination [104, 105].

2.2. Systems used for in vitro migration studies

2.2.1. 2D and 3D systems

Many studies analyzing cell migration *in vitro* are conducted in 2D due to the relatively simple set-up compared to 3D experiments. Often glass or plastic substrates are coated with ECM proteins to enable cell adhesion and cells are seeded on top. This surface coating can also be micro-structured to facilitate migration analysis or applied on a thin layer of hydrogel, mostly cross-linked polyacrylamide (PA), to analyze cells on softer substrates [14–16, 19, 96]. Even though a lot has been learned from 2D experiments about the fundamental signaling cascades and how cell migration can be influenced [63, 106], 2D cultivation is a highly artificial set-up for most cells. The majority of cells in the body is embedded in a 3D matrix surrounded from all sides by matrix proteins, signaling molecules or other cells. Therefore, it is not surprising that differences between experiments performed in 2D and such performed in 3D set-ups or

in *in vivo* experiments have been observed [18, 107, 108].

Adherent cells like fibroblasts seeded on a substrate, especially rigid surfaces like glass or plastic, are well spread with a lot of membrane protrusions and focal adhesions. Cells in 3D have less protrusions and focal adhesions but can interact with their surrounding all around the cell surface [108]. As discussed before (see section 2.1.3) cells in 3D matrices either have to deform the cell body and squeeze through pores in the matrix or digest matrix components to enable cell displacement. In 2D experiments, such constrictions are nonexistent, which completely omits a fundamental step in *in vivo* cell migration [109]. Glass and plastic substrates are, furthermore, very stiff compared to the native ECM of cells, which, with the increasing awareness that cells are mechanosensitive, influences cell responses and hampers the translation of results obtained on such substrates to *in vivo* behavior.

However, in 3D approaches the cell environment and thus cues affecting cell behavior are more complex than in 2D assays, which often impedes the interpretation of the results and the uncoupling of multiple influences on the cell. It is therefore important before conducting an experiment to critically think about which format is best suited for the scientific question that should be investigated.

2.2.2. Synthetic vs. naturally derived hydrogels as 3D matrix

When using a 3D environment to analyze cell migration, either gels formed from naturally derived proteins can be used or synthetic macromolecules can form hydrogels to embed cells. Both approaches have advantages and drawbacks that will be discussed in this section.

Naturally derived gels formed from fiber ECM proteins like collagen I or fibrin are widely used in biological research [110, 111]. Collagen I readily forms a stable fibrilar gel in which cells can be embedded in. The overall structure, stiffness and pore sizes achieved with collagen gels can vary widely depending on the collagen extraction procedure and gelation condition used [22, 70]. The gel can be mixed with other ECM components, e.g. fibronectin, to closer mimic the ECM. Yet, through the formation of fibers, the formed matrix is highly heterogeneous, which on the one hand resembles *in vivo* conditions and mimics the complexity of the ECM, but, on the other hand, hinders the detection of fundamental guidance mechanisms by presenting many different cues at once. Moreover, in collagen gels, the amount of adhesion and cell signaling sites depends on the protein concentration, which determines the stiffness of the gels. Hence, the concentration of adhesion sites cannot be altered without also changing the stiffness of the substrate.

Matrigel, a matrix extracted from Engelbreth-Holm-Swarm mouse sarcoma cells, is another naturally derived matrix used in cell culture [112, 113]. Besides the use in

angiogenesis assays, cancer invasion assays are often performed with this basement membrane mimic as many cells grow very well in and on this substrate. A drawback of this matrix is its very complex composition that is not completely itemized. It contains a lot of growth factors, signaling molecules, and matrix proteins whose concentration have a high batch to batch variability [23, 114]. This impedes the widespread use of Matrigel in many applications due to the lack of reproducibility.

So overall, naturally derived gels can, to a certain extent, capture the complexity of the ECM of cells *in vivo*, concerning the fibrous, heterogeneous structure, its stiffness and pore sizes. However, if controlled and defined conditions are needed to analyze basic guidance mechanisms in cell migration, the variety of different cues presented at once by can impede such studies or hamper their interpretation. Therefore, more and more synthetic materials are used in cell migration studies whose properties are specifically tailored to the conducted research, reducing the complexity of the matrix encountered by cells.

Artificial gels can be produced by a variety of different materials. To mimic the fiber structure of the ECM, electrospun polymer fibers made from polystyren, polyvinylalcohol or similiar bioinert materials can be incorporated in a matrix [28, 115, 116]. Their diameter can vary from a few nm to several µm depending on the material used and the desired application. Peptide amphiphiles are another group of molecules that can form a fibrous matrix for cell migration. Small peptide sequences are conjugated to fatty acid chains which can self-assemble into worm-like micelles. These long micelles then entangle to form hydrogels [117, 118].

Polyethylene glycol (PEG) is a bioinert material that is widely used as backbone substrate in highly cross-linked synthetic hydrogels. Linear and multi-arm PEG monomers are cross-linked using different reaction schemes and form a relatively homogeneous network. Depending on the chemistry used for the polymerization, gelation of the gel can occur spontaneously (e.g. Michael-type addition of vinylsulfone and thiols) [119], upon temperature change (e.g. hydrophobic interactions of poly(propyleneoxid)) [120] or, which is often used in biological applications, upon illumination (radical polymerization including thiol-ene or acrylate reactions) [121–123]. Through the addition of small peptides, adhesion motifs or cleavage sites can be incorporated in the gel [29, 124]. Different versions of the fibronectin derived RGD peptide sequence are often used as ligands and bound to the backbone to enable cell migration. By varying the monomer concentration or the amount of cross-linker used to form the gels, the rigidity of the hydrogel can be tuned and tailored to the biological problem analyzed, independent of the ligand concentration in the gel [125, 126]. A disadvantage of such highly cross-linked polymer gels is the small mesh size of a few tens of nm, which is considerably smaller than pores in the natural ECM. This is a relevant difference to *in vivo* conditions that can alter the migration behavior [127].

2.3. Photo-polymerizable artificial hydrogels as construction kits for 3D cell environments

In this work a radical reaction induced by illumination with UV light was used to polymerize a PEG-based hydrogel. For this reason, a short overview of applications and micro-structures that are realized with photo-polymerized synthetic hydrogels are described in this chapter, followed by an examination of the most important physical properties of such gels.

2.3.1. Photo-induced polymerization of micro-structured hydrogels

When comparing photo-induced polymerization techniques with spontaneous or temperature-induced hydrogel formation, two major advantages stand out; temporal and spatial control of the polymerization. The radical polymerization reaction is very fast, between a few seconds and a few minutes, which ensures a homogeneous distribution of embedded cells, without gravitational settling of cells. Furthermore, the reaction only occurs locally, where the monomer solution is illuminated, which enables the structured polymerization of hydrogels. However, the illumination time, light intensity and wavelength used, as well as the cytotoxicity of the monomers and the photo-initiator have to be taken into consideration, when cells are encapsulated in such hydrogels.
To start the radical polymerization reaction, photo-initiators are necessary. Depending on the absorption spectrum of the initiator, light of different wavelengths has to be used for the illumination. Most initiators have their absorption maximum in the ultraviolet (UV) region, which can be problematic for the survival of cells. 1-[4-(2-hydroxyethoxy)-phenyl]-2-hydroxy-2-methyl-1-propanone (I2959) and lithium phenyl-2,4,6-trimethylbenzoylphosphinate (LAP) are two widely used initiators, which absorb light with a wavelength around 300–365nm and are cytocompatible [121, 128, 129]. Upon light absorption, they are both cleaved into two radicals that start the polymerization reaction. If UV light is not desirable in an application, eosin-Y, a photo-initiator absorbing light around 516nm, can be used to start the reaction [130, 131].
The majority of hydrogels polymerized by a photo-induced reaction in the presence of cells use poly-acrylates or thiols with ene-components like norbornenes or vinyls as functional groups [131–133]. The two systems differ in their polymerization mechanisms, which influences the structure of the formed hydrogel (see figure 2.4). The chain-growth mechanism of poly-acrylates forms a more heterogeneous network compared to thiol-ene reactions, where one thiol reacts with one ene [121, 133, 134]. Therefore, thiol-ene polymerization enables a controlled and homogeneous incorporation of cross-linker molecules. A further advantage is the very easy incorporation of peptide sequences using the thiol-ene reactions. The amino acid cysteine has a thiol in its side

chain, which reacts with ene-groups and thereby peptide sequences with one or two cysteines can be covalently bound to the network or used as cross-linker, respectively [30, 35, 135].

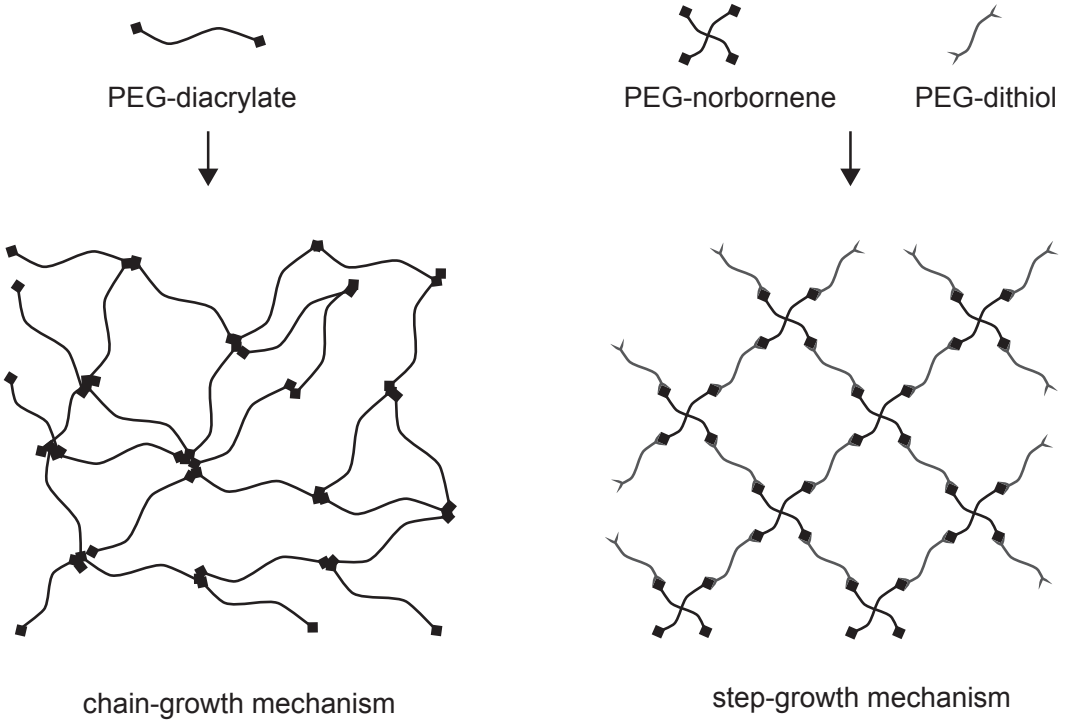

Figure 2.4.: Idealized comparison between networks formed from chain-growth and step-growth mechanism. PEG-diacrylates polymerize via a chain-growth radical reaction that results in an inhomogeneous network with a high variety in mesh sizes. PEG-norbornenes react with PEG-dithiols in a step-growth mechanism. Here one thiol can only react with exactly one norbornene group which produces a homogeneous network.

Due to the spatial control in photo-induced polymerization, advanced hydrogel structures can be achieved by photo-patterning techniques. By polymerizing bulk gels and consecutive diffusion of adhesion ligands into the gel followed by a structured illumination of specific hydrogel areas, cell adhesive patterns are generated in an otherwise non-adhesive surrounding [37, 136, 137]. This can also be done with other small molecules that ought to be bound to the hydrogel or with cross-linkers, which then alters the mechanical and diffusive properties of the gel [38, 138]. It is furthermore possible to directly micro-structure hydrogels to form complex 3D structures or simply to form small micro-patterns inside channel slides [139–141]. In contrast to spontaneously polymerizing gels, where micro-structuring is mostly achieved through micro-molding, photo-polymerizable gels can be directly structured inside channel systems. There, small hydrogel structures can be exposed to fluid flows, media can be easily exchanged and a good optical accessesability facilitates experiments. Furthermore, Beebe and coworkers showed that micro-structured gels in channels together with the inherent swelling of gels (see next section for detailed description of the swelling properties of

synthetic hydrogels) can be used to form dynamic structures [142].

2.3.2. Swelling as inherent hydrogel property

Hydrogels are networks of hydrophilic polymer chains which are highly hydrated and therefore, more than 90% of the gels can be water or other solvent molecules (see figure 2.5). The amount of water that can be stored in the polymer network depends strongly on the gel composition and the ambient conditions. Parameters that can change the amount of water uptake are e.g. the chemical composition and concentration of polymers in the gel, the cross-linking degree, ionic strength or pH of the solvents and the temperature [36, 143].

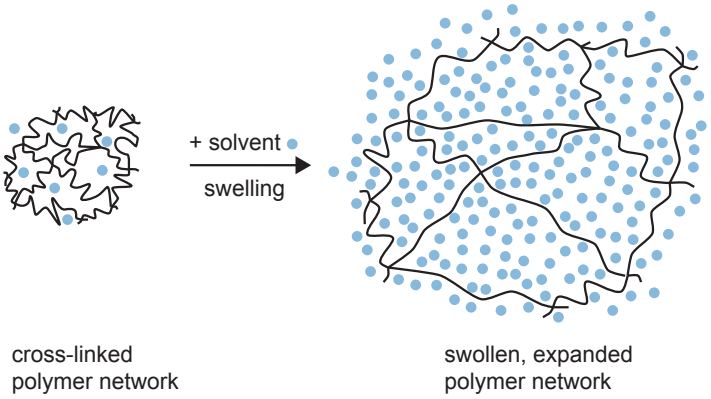

Figure 2.5.: Schematic presentation of the swelling process. The coiled cross-linked polymer network swells upon addition of a solvent, e.g. water. The mesh expands and the polymer chains become elongated.

To quantify the amount of fluid that can be retained by the gel network and thereby describe an important property of hydrogels, a mass swelling ratio Q_m is normally defined in the literature by comparing the dry mass of the polymer network m_d with the weight of the swollen polymer network m_s [144, 145]:

$$Q_m = \frac{m_\mathrm{s}}{m_\mathrm{d}}. \tag{2.1}$$

Another possibility is to use the weighted masses and the known densities of the polymer ρ_p and the solvent ρ_s, normally deionized water, to calculate a volumetric swelling ratio [146]:

$$Q_v = \frac{\frac{(m_s - m_d)}{\rho_s} + \frac{m_d}{\rho_p}}{\frac{m_d}{\rho_p}} = 1 + \frac{\rho_p}{\rho_s}\left(\frac{m_s}{m_d} - 1\right). \tag{2.2}$$

The gels used for these characterizations are swollen freely floating in the swelling solution to reach equilibrium swelling. A restriction of the swelling by physical constrains, like covalently immobilizing a gel on a surface or between to parallel plates, will alter the swelling behavior and reduce the overall swelling [147].

To better grasp how the swelling ratio is influenced by gel composition and solvent properties, the underlying mechanisms and driving forces for the water uptake have to be elucidated. Many theoretical approaches have been described in the last decades concerning hydrogel swelling, e.g. reviewed in [148]. Most of them are based on the fundamental work of Flory and Rehner [149, 150]. However, these theories have limitations for non-ideal gels as certain assumptions or simplifications are used in the calculations. Nonetheless, a short overview of the basic underlying principles of gel swelling will be presented in the following according to the Flory-Rehner theory with one extension, the influence of ionic groups localized on the polymer backbone.

In the theory implemented by Flory and Rehner in 1943, the swelling of an uncharged gel consisting of tetrahedral building units, which results in affine network deformations, is discussed. Two important processes have to be considered to understand the swelling process. When solvents enter the polymer network in the swelling process, polymer and solvent molecules mix and the network expands. For non-cross-linked polymers, this dilution of the chains can be infinite. For cross-linked gels, the uptake of solvent molecules results in an expansion of the network. This leads to an elongation of the polymer chains, which results in a retractive force. At equilibrium, these two effects (the mixing free energie, ΔF_{mix}, and the elastic retraction energy, ΔF_{el}) counterbalance and the change of the free energy ΔF is zero.

$$\Delta F = \Delta F_{mix} + \Delta F_{el} \tag{2.3}$$

If, as in the case of peptide-functionalized hydrogels, charges are present in the polymer, the ionic interaction between the network and the solvent has also to be accounted for and equation 2.3 expands to:

$$\Delta F = \Delta F_{mix} + \Delta F_{el} + \Delta F_{ion} \tag{2.4}$$

The first factor, ΔF_{mix}, the mixing free energy of polymer and solvent, can be described by the thermodynamic theory of polymer solutions. The entropy of mixing is always positive as the mixing of two components increases the number of possible arrangements in the system. An expression for the entropy of mixing was independently derived by Huggins and Flory [151–153]. They adapted the mixing entropy of ideal solutions to systems where one component is a polymer consisting of n sub-molecules which have the same size as a solvent molecule. Compared to the ideal solutions, in polymer solutions the distributions of the n sub-molecules in the lattice model (see figure2.6) are not independent of each other as they form linear chains. This greatly effects the calculation of the mixing entropy ΔS_{mix}

$$\Delta S_{mix} = -k_b N_s ln(1 - \varphi_p) \tag{2.5}$$

with k_b the Boltzmann's constant, N_s the number of solvent molecules, φ_p the polymer volume fraction, which is the reciprocal of the volumetric swelling ratio, Q_v.

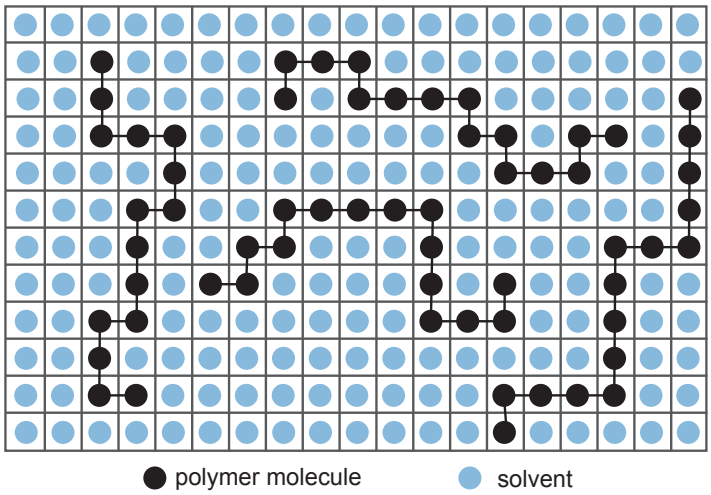

Figure 2.6.: Lattice model used as basic concept in the mixing theory by Flory and Huggins. The lattice is occupied by solvent (blue circles) and polymer (black circles) molecules of the same size. n polymer molecules form a polymer chain.

To calculate the free energy change of mixing, ΔF_{mix}, also the mixing heat, ΔH_{mix}, has to be included. There, the internal interaction energies of polymer and solvent molecules, as well as the interaction energies of solvent-polymer pairs are considered.

$$\Delta H_{mix} = N_s k_b T \chi \varphi_p \tag{2.6}$$

with T the absolute temperature and χ the polymer solvent interaction parameter. χ combines the interaction energies of solvent-solvent, polymer-polymer and polymer-solvent pairs and describes if a mixing of two components is energetically favorable compared to an unmixed state ($\chi < 0$) or energetically unfavorable ($\chi > 0$). For hydrogels, the interaction parameter is negative, thus the change in the mixing free energy is negative and is a driving force of the swelling process.
Combining equation 2.5 and 2.6, the free energy change of mixing can be calculated:

$$\Delta F_{mix} = k_b T N_s [ln(1 - \varphi_p) + \chi \varphi_p] \tag{2.7}$$

The second factor of the free energy change, the elastic retraction energy, ΔF_{el} is dominated by the entropy change from a system of coiled, entangled polymers in the unswollen polymer network and the elongated polymer chains in the swollen gel:

$$\Delta S_{el} = \frac{3 N_c k_b}{2} (ln\alpha - \alpha^2 + 1) \tag{2.8}$$

with N_c the number of chains in the network and α the linear swelling ratio, which can be calculated from the volumetric swelling ratio Q_v in isotropically swollen gels according to

$$\alpha = Q_v^{1/3} \tag{2.9}$$

In the unswollen state the chains can have various different conformations by rotating bonds in the polymer backbone. Upon swelling and expansion of the network, the polymer chains are elongated, which decreases the possible chain conformations. The stronger the chain deformation, the bigger the entropy loss and thus, the elastic retraction energy countervails the swelling process.
The third factor of the free energy change, the ionic interactions of solvent and polymer, was not accounted for in the theory of Flory and Rehner, however, it plays an important part in charged gels. Most gels used for biological applications have small peptides or other charged groups incorporated in the polymer backbone to facilitate cell-network interactions. Often, the Donnan theory [154] is used to describe the swelling of such charged polymers [155–157]. As the polymer charges are fixed on the network backbone, the interaction between the swelling polymer and the surrounding pure solution can be described analogous to two solutions separated by a semi-permeable membrane (see figure 2.7). Ions from the solution A_s^- and C_s^+ can diffuse into the network and counterbalance the fixed charges P_{fix}^{z+} in the polymer. This results in uneven concentrations of the mobile ions in the polymer ($[A^-]_{gel}$ and $[C^+]_{gel}$) and the ions in the solution and a Donnan coefficient r_D can be calculated:

$$\frac{[C^+]_s}{[C^+]_{gel}} = \frac{[A^-]_{gel}}{[A^-]_s} = r_D \tag{2.10}$$

Thus, a difference in the potential, the Donnan potential, is built up between the two sides. This potential is the reason for the osmotic pressure, $\Delta\phi$, that increases the swelling of charged polymer networks.

$$\Delta\phi = \frac{RT}{F} ln(r_D) \tag{2.11}$$

with R the universal gas constant, and F the Faraday constant. As, within one compartment, the ionic charges counterbalance, equation 2.12 and 2.13 together with 2.10 and 2.11 can be used to describe the Donnan potential depending on the concentration of the fixed charges (see 2.14).

$$[C^+]_s - [A^-]_s = 0 \tag{2.12}$$

$$[C^+]_{gel} - [A^-]_{gel} + z[P^{z+}]_{fix} = 0 \tag{2.13}$$

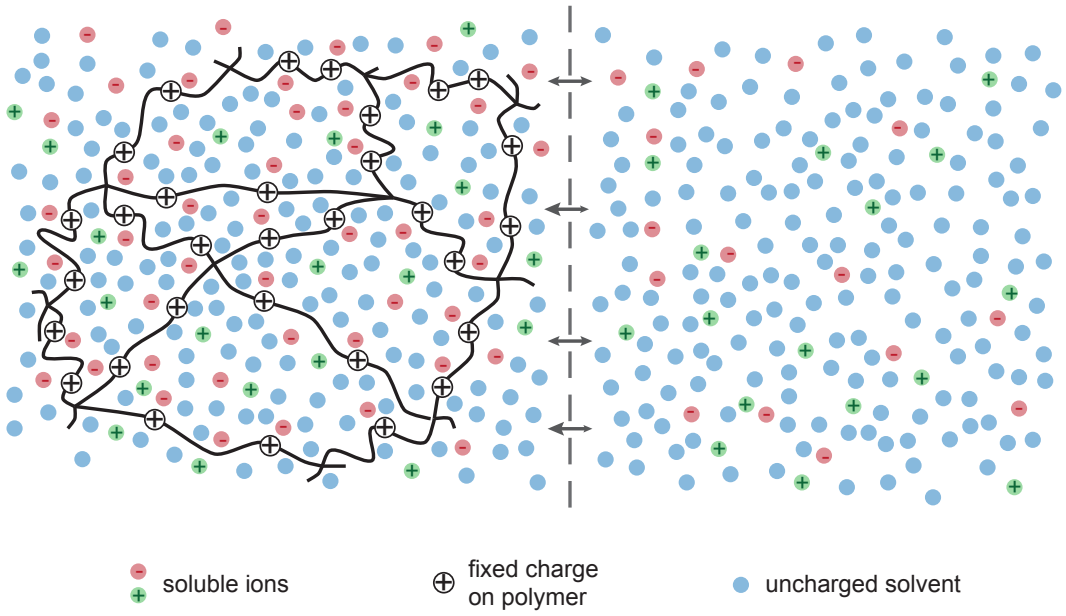

Figure 2.7.: Schematic presentation of the Donnan equilibrium of a cationic polymer network. In charged matrices, the mobile ions of the solvent are unevenly distributed between the network and the surrounding solution. This system can be described as two solvent compartments separated by a semi-permeable membrane.

$$\Delta\phi = \frac{RT}{2F} ln(1 + \frac{z[P^{z+}]_{fix}}{[C^{+}]_{gel}}) \tag{2.14}$$

If the ionic strength of the swelling solution is small (small $[C^+]$), the osmotic pressure increases and the gels swell strongly. If the concentration of the ions in the solution is high (big $[C^+]$), the difference is smaller and the gels swell less. Many immobilized charges in the polymer (big $[P^{z+}]_{fix}$) increases the swelling.

To conclude, different mechanism that influence and drive the swelling of hydrogels were assessed in this section. In this simplified approach it was assumed that the different contributions to the free energy are independent of each other. However, of course, this is not the case for real networks. For example, charges in the polymer not only influence the osmotic pressure, but also change the interaction energies of the polymer. Nonetheless, the examination of the driving forces for hydrogel swelling enable the understanding of how and why changing e.g. the cross-linker concentration or chemical composition in a network or increasing the ionic strength of the swelling solution influences the swelling behavior.

With the theory of Flory and Rehner as fundamental description of polymer swelling, further analysis of the polymer network are possible. Mesh size calculations or estimates of the mechanical properties of the network can be performed [158]. As in this work mainly non freely swollen gels are used and thus, the swelling theory of Flory and Rehner cannot be adapted to the system, these aspects will not be further discussed here.

3. Photo-Lithographic Structuring of Synthetic Hydrogels in Channel Slides

In this work, a synthetic hydrogel system was adapted that has been previously described in several publications as being well suited for cancer cell migration studies [125, 145, 159, 160]. 20kDa 4-armed polyethylene glycol with a norbornene group at each end of the arms (PEG-NB) is polymerized with linear cross-linkers containing thiol groups at each end (see figure 3.1 for a schematic overview). As cross-linkers either a 1kDa PEG-dithiol is used if the gel should not be digested by cells, or a peptide sequence that can be degraded by cell secreted matrix-metalloproteinases (MMPs) is used. This degradability of the network is indispensable if cells should migrate through the gel, due to the small mesh size of just a few tens of nm [30, 128, 159]. A cystein containing short RGD-peptide sequence is present in the mixture to enable cell adhesion via integrins. To embed cells in the gel, a cell suspension in PBS is mixed with the pre-polymer solution. To be able to start the radical polymerization reaction with UV-light, a photo-initiator, LAP, is supplemented in the pre-polymer solution.

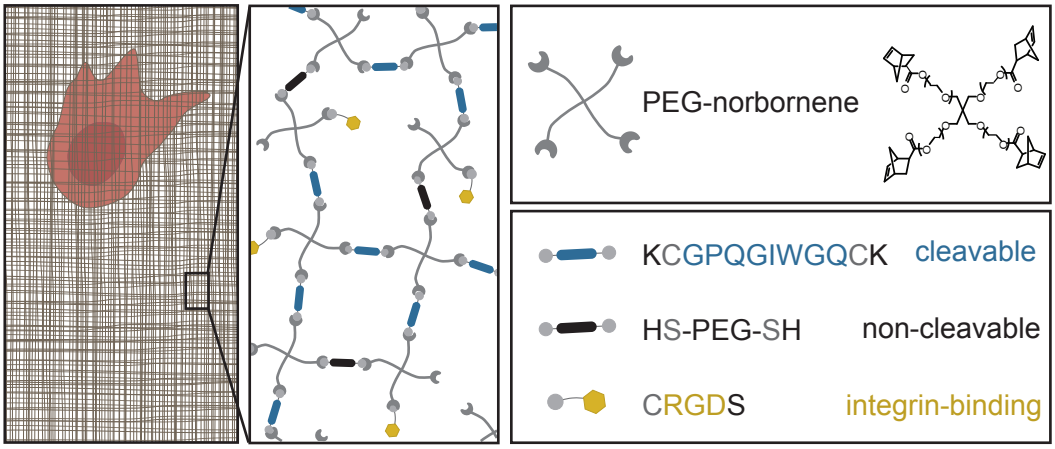

Figure 3.1.: Schematic overview of the gel components used to form the synthetic hydrogel. PEG-NB is cross-linked with a linear cross-linker containing two thiols. It can either be a peptide sequence which can be cleaved by MMPs, or a bioinert, linear PEG. An RGD-peptide sequence is covalently bound to the network to enable cell adhesion. The figure is adapted from [161] with permission from the Royal Society of Chemistry.

When illuminated with light of a wavelength around 365nm the photo-initiator absorbs the light and dissociates into two radicals. The formed molecules are highly reactive and abstract hydrogen atoms from surrounding molecules, especially hydrogens from the thiol group of the cross-linker present in the solution (see left panel of figure 3.2). The now formed thiyl radical enters the radical step-growth polymerization cycle and reacts with the alkene group of the PEG-NB monomers to form a carbon-centered radical. Hydrogen abstraction from another thiol group results in a stable thioether linkage and a new thiyl radical (see right panel of figure 3.2). Through such a step-growth polymerization uniform polymer networks are created [160].

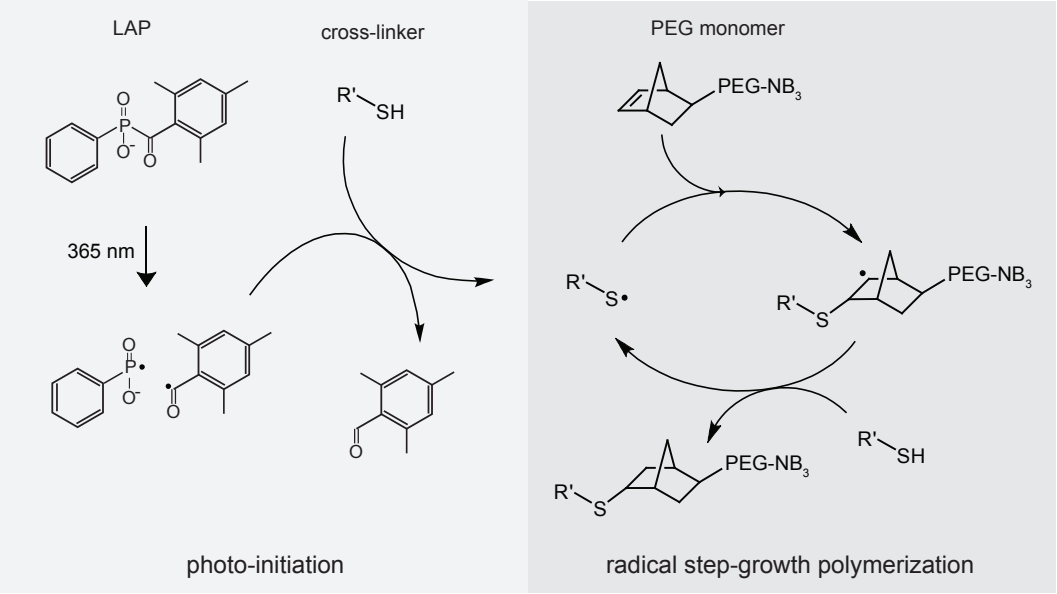

Figure 3.2.: Radical thiol-ene polymerization reaction used to form covalently cross-linked hydrogels. A photo-initiator, which dissociates into two radicals upon illumination with 365nm light is essential to start the step-growth polymerization. It reacts with a thiol to form a thiyl radical. This radical reacts with the alkene group of the norbornene forming a stable thioether bond after abstraction of a hydrogen atom from another thiol group.

As the degree of cross-linking in the hydrogel network influences gel properties like swelling and stiffness, the amount of cross-linker used to form the gels is defined as cross-linker ratio r_c according to equation 3.1.

$$r_c = \frac{2c_{\text{cross-linker}}}{4c_{\text{PEG-NB}}} \tag{3.1}$$

r_c describes the ratio of total amount of functional groups of the cross-linker (containing two thiol groups per molecule) to the total amount of functional groups of the PEG-NB monomers (4 norbornene groups per monomer), using $c_{\text{cross-linker}}$ and $c_{\text{PEG-NB}}$, the concentration of the cross-linker and PEG-NB monomer in the pre-polymer solution, respectively. A cross-linker ratio of one indicates that every norbornene present in the solution can react with one thiol group from the cross-linkers, resulting in a completely

cross-linked gel.

The advantage of a photo-induced radical reaction is that the formation of the network can be controlled temporally and spatially. In this work, a 365nm LED lamp equipped with a collimator to parallelize the light is used to polymerize the hydrogel. The reaction is very fast and therefore, prevents settling of suspended cells and ensures a homogeneous cell distribution over the entire gel volume.

To form hydrogel micro-structures inside channel systems, photo-lithography is used. A chromium mask containing the micro-structures (parallel strips of 100–400µm width and 5mm length with a strip to strip distance of 30–600µm) ensures that the channel system is only partially illuminated by the parallel light. The polymerization procedure is illustrated in figure 3.3. In this thesis, the pre-polymer solution was injected in different µ-channel slides from ibidi and illuminated through a chromium mask. Where the light passes through the mask and enters the gel, the network is formed. The unpolymerized pre-polymer solution in the unexposed channel areas is subsequently washed out of the channel with PBS or cell culture medium, leaving micron-sized gel structures in the channel. Due to the inherent swelling properties of synthetic polymer gels, the formed structures swell within the first hours after polymerization.

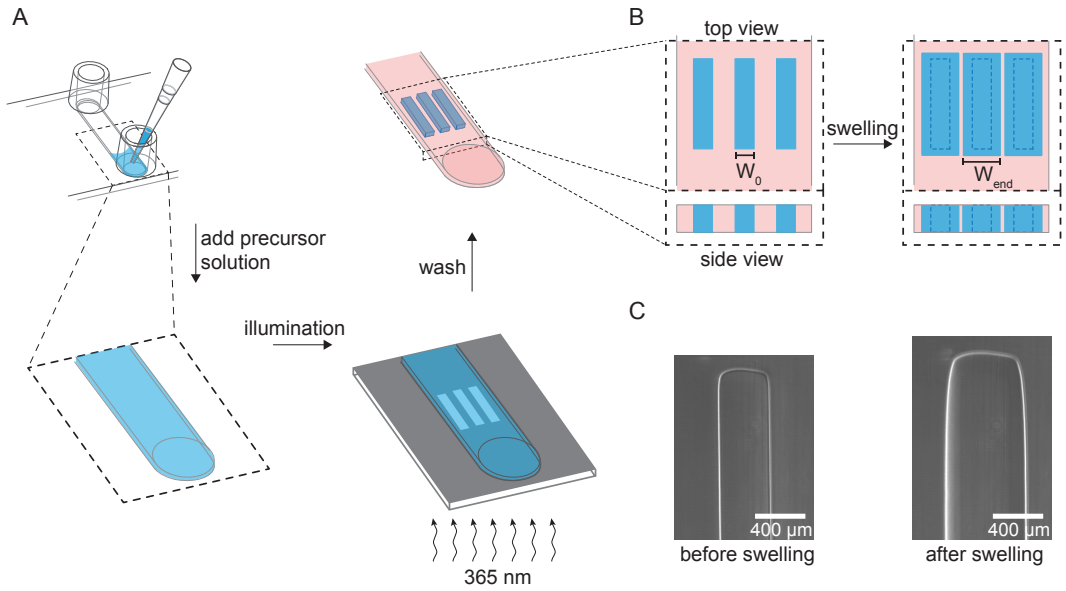

Figure 3.3.: Schematic illustration of the photo-lithographic micro-structuring of hydrogels in channel slides. (A) The pre-polymer solution is pipetted in a channel slide and illuminated through a chromium mask with 365nm light. The gel polymerizes in the illuminated areas and forms small micro-structures in the channel. The unpolymerized solution is washed out of the slide. (B) Schematic top and side view of hydrogel strips in channel slides. The polymerized structures with an initial strip width W_0 swell to reach their final dimensions (width W_{end}) after a few hours. (C) Phase-contrast images of a degradable MMP-hydrogel strip (3mM PEG-NB and a cross-linker ratio of 0.9) directly after illumination (left) and after 3h of swelling in PBS (right).

4. Characterization of the Synthetic Hydrogel System

When using a matrix to study cell migration, one has to consider the influence that matrix properties have on the cell behavior. In synthetic hydrogels, different parameters, like monomer and cross-linker concentration and size, concentration of adhesion molecules or solvent conditions, can be used to tune matrix properties [36, 162]. The illumination time used for the polymerization can also be varied to optimize the formed gel for cell migration studies.
A special characteristic of the hydrogels used in this work is the polymerization of small gel strips inside plastic channels. This confinement of the gel by the channel bottom and top influences the swelling behavior of the gel and impedes a direct comparison to literature data, as swelling ratios are normally calculated from freely swollen gels. Additionally, with this swelling in confined conditions the question arises if the channel and gel dimensions themselves influence the swelling behavior, a phenomenon not seen in freely swollen gels. Hence, not only gel composition, but also the influence of channel and gel dimensions on the swelling behavior is analyzed in the next section, followed by bulk stiffness tests and cell viability studies for micro-structured hydrogel strips inside channel slides.

4.1. Particle image velocimetry analysis of the swelling process

In classical hydrogel swelling experiments, the swelling ratio, an important parameter describing hydrogels, is calculated by comparing the weight or volume of the swollen hydrogel with the initial dry monomer weight or volume. However, these measurements are bulk analysis of gels swollen while freely floating in the swelling media. In this work gels are polymerized as small gel strips inside channel systems. This confinement does not only influence the equilibrium swelling of the gel, but it makes it impossible to calculate the swelling ratio in the classical way. As the gel is micro-structured in the channel, weighting the gel or assessing the volume of the dry polymer would only be possible with the entire slide, which is not feasible. To find another adequate measure

for the swelling behavior of small gel strips within a channel system, the swelling process itself has to be carefully analyzed.

With particle image velocimetry (PIV) analysis, the displacement of the polymer network while the gel swells can be assessed. PIV is a pattern matching technique where consecutive images of a time series are compared to retrieve overall movement of objects in the observation area. Originally, PIV was used in flow experiments, analyzing turbulences and flow profiles [163]. However, PIV was already used in other applications, e.g. in analyzing dynamics of migrating cell sheets or assessing strains induced in collagen gels [164–166] . In classical tracking experiments, the position of single objects like cells or beads are tracked at every time point of an experiment. In contrast, in PIV analysis, the field of view is divided in sub-areas and through cross-correlating the intensity values within these areas of consecutive time points, a displacement for every sub-region can be calculated. This results in a displacement field, which, by knowing the time between two consecutive images, can be converted into a velocity field.

In this thesis, 400µm wide strips are polymerized in 400µm high channels and swollen in PBS while time-lapse series of the strip are recorded in 2min intervals. PIV analyses of the time-series result in velocity vector fields describing the swelling process. After 2h no significant overall gel displacement was observed in the PIV analysis, which indicates completed swelling of the small strips (see figure 4.1). The analysis furthermore shows that less cross-linked gels have a higher overall gel displacement and swell for a longer time, which is more pronounced in the 2mM PEG-NB gels compared to 3mM gels.

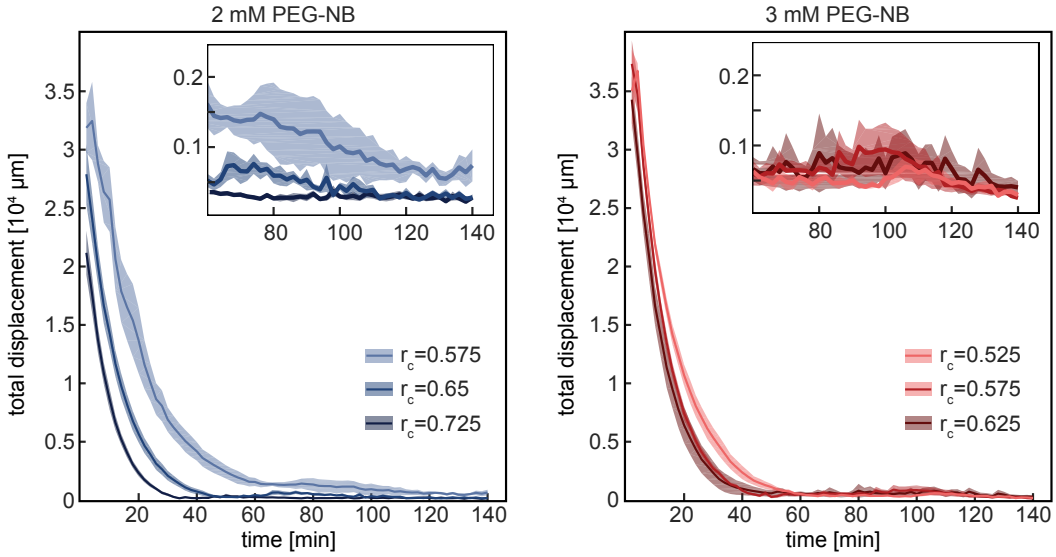

Figure 4.1.: Overall displacement in swelling gel strips over time. The sum over all displacements within an observed strip region is displayed for the first hours after gel polymerization. Different hydrogel compositions were analyzed (gels containing 2mM PEG-NB in blue, gels with 3mM PEG-NB in red). Inlays show a close-up of the displacement starting 1h after hydrogel polymerization. Shaded areas represent the standard deviation of the mean of 3 independent experiments.

The sum over 2h of the velocity fields for a 2.5mM PEG-NB gel with a cross-linker ratio of 0.55 is shown in figure 4.2. The analysis shows that the swelling at the end of a hydrogel strip (red box in figure 4.2) and in the longitudinal middle section of the strip (green box in figure 4.2) differs. In both positions, the swelling results in a displacement towards open, non-polymerized space in the slide. At the ends of the micro-structures, this means a swelling parallel as well as perpendicular to the short axis of the strip. In the middle part the gel is surrounded by more gel in the direction of the strip length. Therefore, a gel displacement is only possible in direction parallel to the short axis of the strip.

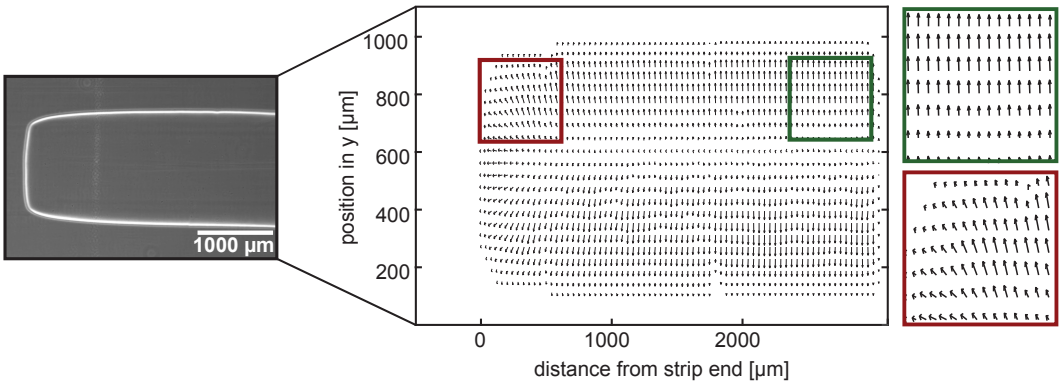

Figure 4.2.: Particle image velocimetry analysis of the swelling process of gel strips. On the left a phase-contrast image of the part of the hydrogel strip analyzed with PIV is shown. In the middle, the velocity vector field received from the swelling process, as sum over the first 2h is displayed. Close-ups from the longitudinal middle part of the strip (green box) and from the end of the strip (red box) show a movement of the gel in the outward directions. For the middle part of the strip, this outward movement results in a uniaxial deformation of the gel.

The swelling was further analyzed in the longitudinal middle part of gels of different compositions, showing that the uniaxial swelling in the strip middle occurs in all tested gels (see figure 4.3).

This anisotropic swelling can be explained by frictions between the channel bottom or top and the hydrogel. For a homogeneous swelling of the strip, outer hydrogel sections have to be displaced so that the inner hydrogel can expand. Along the length of the strip (total length of 5mm), much more hydrogel would have to be displaced to enable the swelling of the middle strip part in contrast to a displacement along the short axis of the strip (400µm width). Thus, in the longitudinal middle part of the strip, swelling of the hydrogel results in a gel displacement only parallel to the short axis of the strip. As the initial strip width and the strip width in the middle 20% of the longitudinal section of the strip after swelling are easily assessable by light microscopy, the ratio between these two widths is hereon used to describe the swelling of the small hydrogel strips in confinement.

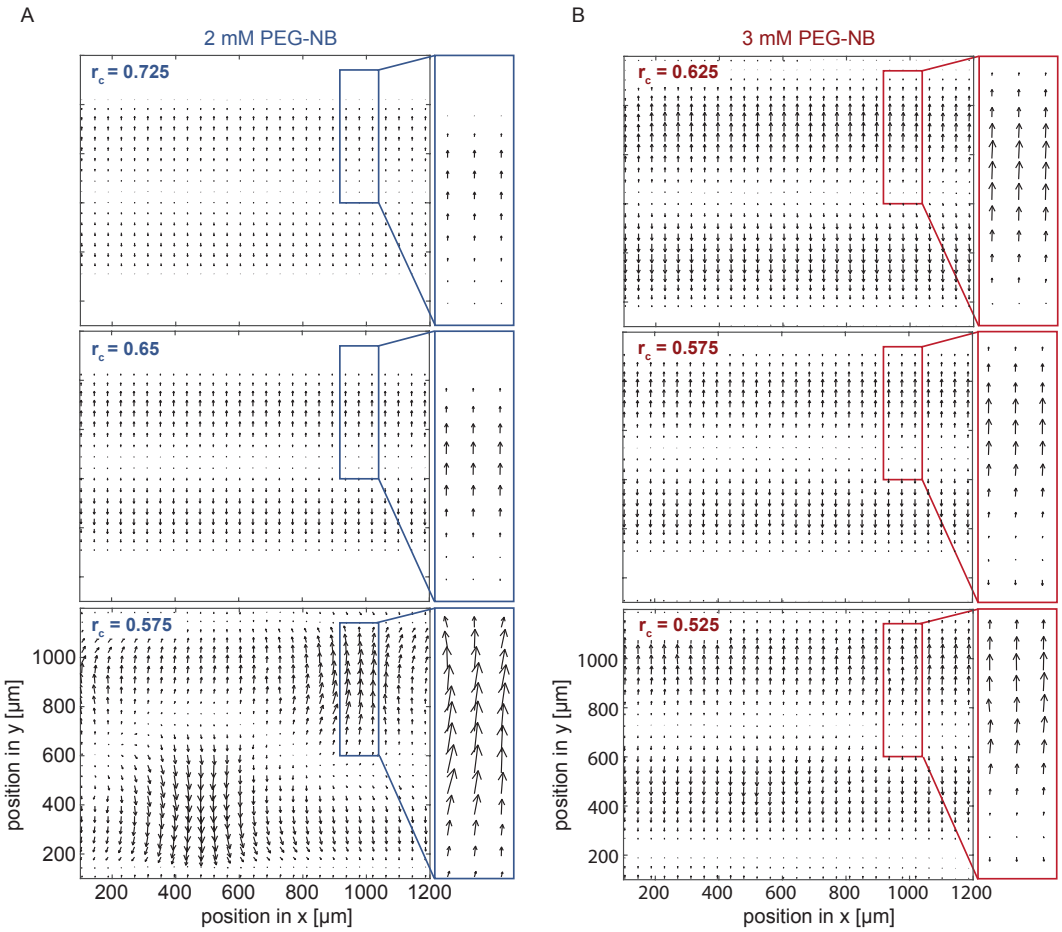

Figure 4.3.: PIV analysis of the longitudinal middle section of strips of different composition. PIV measurements of the swelling process of gels with a PEG-NB concentration of (A) 2mM and (B) 3mM and three different cross-linker ratios. Close-ups show the uniaxial deformation of the gel parallel to the short axis of the strip. The figure is adapted from [161] with permission from the Royal Society of Chemistry.

4.2. Tuning the swelling behavior of micro-structured gels in confinement

As discussed in subsection 2.3.2, all cross-linked synthetic polymer gels swell after the polymer network is formed. The swelling behavior thereby depends on the composition of the polymer network. Given that the swelling of micro-structured gels in confinement is used in this work to form complex migration environments for cells, the swelling behavior of such gels is carefully analyzed in this section to optimize the gel. A first step in the optimization of the polymerization conditions is measuring the amount of light needed to complete the radical polymerization reaction as well as the concentration of photo-initiator that has to be present in the solution. To ensure a good work flow and cell survival throughout the polymerization, short illumination times are favored. We used a 365nm LED with a power density of $10\,\mathrm{mW/cm^2}$ to form 400µm wide strips and tested different combinations of illumination time and initiator concentration. The

gel strip width directly after the illumination (W_0) and after swelling of the structures in PBS overnight (W_{end}) is measured and the swelling ratio calculated according to equation 4.1.

$$r_{\text{sw}} = \frac{W_{\text{end}}}{W_0} \tag{4.1}$$

It is thereby possible to determine the lowest illumination time and initiator concentration needed to achieve consistent polymerization results. For very short illumination times of 5 and 10s in combination with low LAP concentrations, the anticipated initial strip width of 400µm is not reached (see figure 4.4). However, for all LAP concentrations tested, an illumination of 20s is enough to complete the polymerization reaction. Above 20s, no change in initial strip width or the calculated swelling ratio is visible. The constant swelling ratio indicates that after 20s all monomer molecules reacted and the matrix polymerization is completed. To ensure that the network is completely polymerized and constant swelling ratios can be achieved, at least 2.2mM photo-initiator and an illumination time of 20s is used for further applications.

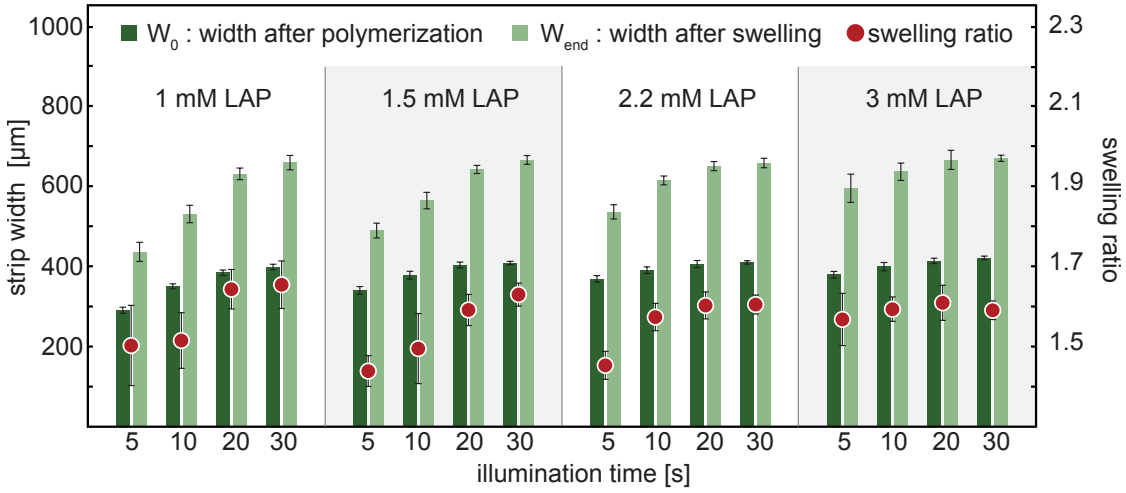

Figure 4.4.: Determination of the illumination time and LAP concentration necessary for completed gel polymerization. Four different LAP concentrations as well as four different illumination times were tested. The initial strip width after polymerization (W_0, dark green) and the strip width after swelling (W_{end}, light green) are displayed and used to calculate the swelling ratio (red dot) according to equation 4.1. Results represent mean and standard deviation of three measurements.

Furthermore, the use of different solvents and swelling media was tested with 400µm gel strips containing either the 1kDa PEG-dithiol (PEG-gels) or the MMP-cleavable peptide (MMP-gels) as cross-linker. As swelling media Milli-Q water, PBS and cell culture medium (DMEM + 10%FBS) were tested, whereas cell culture medium was not used as solvent for the monomers to prevent unspecific covalent immobilization of media or serum components to the hydrogel in the radical polymerization reaction. In figure 4.5 no solvent or swelling media dependency is visible for the PEG-gels,

which show a constant swelling ratio of approximately 1.3. This is in good agreement with the polymer swelling theory of Flory and Rehner described in subsection 2.3.2. For uncharged PEG-gels, the ionic strength of the solutions does not influence the swelling as only mixing and elastic contributions according to equation 2.3 have to be considered. MMP-gels, with a peptide sequence as cross-linker, however, have fixed charges on the polymer backbone (charge of around +2 per cross-linker molecule at pH 7.4). Therefore, an increase in the ionic strength of the swelling solution as well as of the solvent media (Milli-Q water < PBS ≈ cell culture medium) decreases the osmotic pressure according to equation 2.14 and thus results in a lower swelling compared to ion free solutions (see figure 4.5). Such strong dependencies of the swelling behavior on the pH or ionic strength of the solution are used in other applications to e.g. block channels and redirect fluid flows in micro-fluidic set-ups [142].
For later applications in this work, when cells are encapsulated in the gel, changes in the ionic strength of the solution are not favorable. Then, Milli-Q water is not suitable as monomer solvent, but rather PBS should be used to maintain the osmotic balance between the cell and its environment. The same holds true for the swelling media as soon as cells are present in the system.

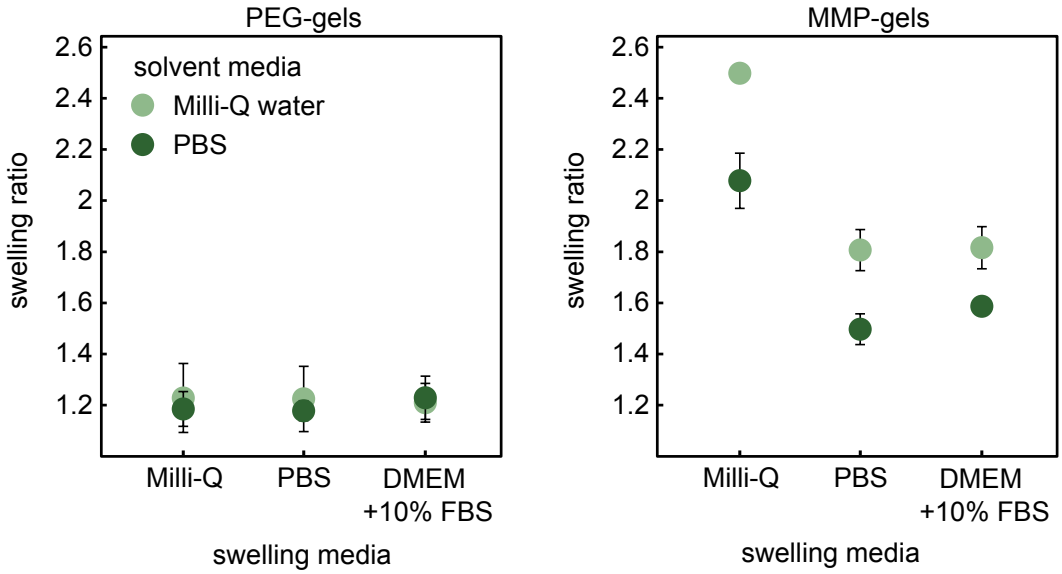

Figure 4.5.: Dependency of the swelling ratio on the polymer solvent and swelling media. 3mM gels cross-linked with PEG-dithiol (PEG-gels, left graph) or the MMP-cleavable peptide cross-linker (MMP-gels, right graph) with a cross-linker ratio of 1 are polymerized in 400 µm high channels with W_0=400 µm. The pre-polymer solutions are either prepared in Milli-Q water (light green circles) or PBS (dark green circles) and swollen at 37°C in different swelling media over night. Results represent mean and standard deviation of three measurements.

In a next step, the influence of the channel height as well as the strip dimensions on the swelling are analyzed. For freely swollen gels at the equilibrium swelling point, the entropy decrease of the polymer chains and their elastic restoring force counterbalance

the mixing energy of solvent molecules with the polymer network. However, in the set-up described in this study the micro-structured gels are confined in their height by the channel bottom and top. Hence, expansion of the gel in direction of the channel height is not possible. Furthermore, an additional force is acting on the gel while swelling: friction between gel and channel surface. For this reason, the channel and gel geometry can have a big impact on the swelling behavior.

In figure 4.6 the swelling ratio of gel strips that have an initial strip width of 100–600µm, polymerized inside 100µm and 400µm high channels, is shown. For gels with a cross-linker ratio of 0.6, the swelling does not show a dependency on the strip width, in both 100 and 400µm high channels. In the 100µm channels gels have a smaller swelling ratio compared to the 400µm channel. Furthermore, if the cross-linker ratio is increased, a higher initial strip width decreases the swelling in both low and high channels.

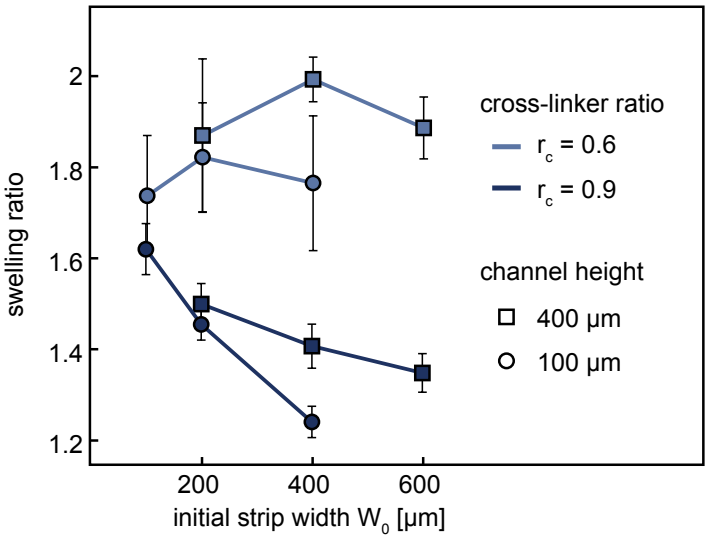

Figure 4.6.: Dependency of the swelling ratio on the height of the channel and the initial strip width. 2mM gels with a cross-linker ratio of 0.6 and 0.9 were polymerized as 100–600µm wide strips in 400µm and 100µm high channels. Results represent mean and standard deviation of three measurements.

In the low channels, the percentage of gel directly neighboring the channel bottom and top is higher compared to 400µm high channels. Thus, the swelling in the low channels is more hindered by the friction. The same principle is applicable when going from small strips to broader strips. If a gel has an initial strip width of 600µm, a big percentage of the hydrogel at the sides of the gel has to be displaced to make room for the inner gel volume to also swell. If the gel is not under confinement, this displacement can easily be achieved and it does not have a energetic difference how big the volume that has to be displaced, is. However, in the confined geometry, a bigger volumetric displacement means more energy lost to the friction between channel and gel. This dependency is not observed in hydrogel slabs that swell while freely floating in the

swelling media, which is why no literature value for this phenomenon can be presented at this point.
The results of the swelling behavior presented here illustrate the many components which influence the swelling of micro-structured hydrogel strips in confinement. Thus, in this work, as many factors as possible are kept constant and only a few are varied to have a good control over the gels. All micro-structured gels discussed in the next chapters are formed by using the gel components dissolved in PBS, with a photo-initiator concentration of 3mM and an illumination time of 20s. As swelling solution, cell culture medium is used when cells have to be kept alive in the system. Otherwise PBS is used as swelling media. Initial hydrogel strip width as well as channel height are kept constant within an experimental set-up, whereby the swelling behavior will only depend on the used concentration of PEG-NB monomer as well as on the cross-linker ratio. Detailed analyses of the swelling behavior in the different experimental set-ups are discussed in the corresponding chapters 5 and 6.

4.3. Stiffness measurements on bulk samples

It is well known that cells can probe their environment not only concerning chemical cues, but are able to test the mechanical properties of the surrounding matrix [105, 167, 168]. This mechanosensitivity guides cell migration, stirring for example cancer cells from soft towards stiffer substrates [19, 169]. Therefore, the mechanical properties of hydrogels used in this work are tested in bulk measurements using a MCR100 plate-plate rheometer as described in section A.4.4. Big hydrogel slabs with a diameter of 2cm and a height of approximately 2mm were polymerized and swollen freely floating in PBS overnight. Gels containing 2mM or 3mM PEG-NB monomer with different cross-linker ratios are tested. The gels are soft, having a storage modulus of less than 100Pa (see figure 4.7). With increasing cross-linker ratio the stiffness increases for both monomer concentrations, with the 3mM gels being slightly more rigid. Similar low stiffnesses were previously reported for biopolymer networks as well as synthetic hydrogels used in *in vitro* migration studies [30, 170].
These bulk measurements can only be seen as an approximation for the stiffnesses of the micro-structured gel in confinement used in this work. The degree of swelling has a big impact on the mechanical properties of hydrogels, as less swelling and thus more compact gels were shown to exhibit a higher stiffness [171, 172]. As demonstrated in the previous section, the swelling of strips inside channels is hindered by the confinement. Consequently, the stiffness of the gel strips would be higher than the measured bulk stiffness. A direct measurement of stiffness properties in the gel strips inside the channel is, however, only possible through microrheological measurements including passive microrheology, magnetic tweezer experiments or optical traps. These techniques use

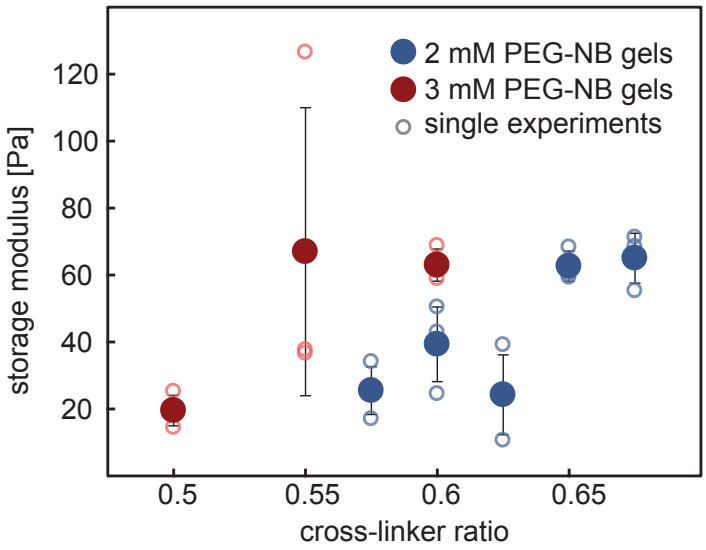

Figure 4.7.: Storage modulus of bulk hydrogels. The storage modulus of bulk hydrogels with 2mM (blue) and 3mM (red) PEG-NB and varying cross-linker ratio are measured in a shear rheometer. Results are the mean with standard deviation of three independent measurements. The figure is adapted from [161] with permission from the Royal Society of Chemistry.

laborious equipment and are restricted, especially in the case of passive rheology, to a limited stiffness range [173–175]. For this reasons, no such microrheological measurements were performed in this thesis. The bulk measurements, nonetheless, give a good approximation of the stiffness range experienced by cells in the gel strips.

4.4. Cell viability studies of encapsulated HT-1080 cells

To ensure that the cells used in this work survive when they are encapsulated in the synthetic hydrogel strips, cell viability stainings were performed. Multiple samples of 400µm strips are prepared for each tested hydrogel composition with HT-1080 cells encapsulated at a concentration of $6.7\text{x}10^5$ cells/ml. A daily media change ensured constant media quality over a four day period. To test the viability, a live-dead staining using propidium iodide (PI) and fluorescein diacetate (FDA) in PBS was performed 3h after gel polymerization and at every consecutive day. The non-fluorescent FDA molecule is taken up by living cells and metabolized into the green fluorescent fluorescein using esterases, thereby only labeling viable cells green. PI cannot penetrate intact cell membranes but intercalates with the DNA in the nucleus if cells are dead and their membranes destroyed, labeling these cell nuclei red. With this staining procedure, the number of viable cells N_{viable} and dead cells N_{dead} in a sample can be counted and an overall viability v calculated according to equation 4.2.

$$v = \frac{N_{\text{viable}}}{N_{\text{viable}} + N_{\text{dead}}} \tag{4.2}$$

When testing gels with different compositions, low PEG-NB concentrations as well as low cross-linker ratios increase the viability of encapsulated cells (figure 4.8). The 2mM gels tested show a viability of nearly 100% over four days. The high survival rate demonstrates, that the small pores of the gel do not hinder media diffusion into the gel and that nutrient supply in the small strips is guaranteed. In all 4mM gels and the 3mM gels with a cross-linker ratio of 0.9, cell viability decreases dramatically. Even only 3h after encapsulation, less than 20% of the cells are alive in these gels. A reason for this can be the increased network density and thus a stronger confinement of the cells in a stiffer gel. Therefore, the forces acting on the cells due to the gel swelling are higher which can explain the increased number of dead cells immediately after the polymerization. However, the low viability in these gels cannot be attributed to smaller mesh sizes in the gels and thus a hindered diffusion of nutrients from the media to the cells. For this limitation to effect cell viability, more time would be necessary and no decrease only 3h after encapsulation would occur. A reduced viability of encapsulated NIH 3T3 cells due to insufficient media supply was observed by Cuchiara et al. in big PEG-DA gels [176]. However, the effect was only observable more than 24h after encapsulation of the cells. The gels with higher polymer concentration tested here are, due to the small viability of encapsulated cells, not suitable for cell migration studies. Hereon, only 2mM gels and 3mM gels with small cross-linker ratio are used for migration experiments with encapsulated cells.

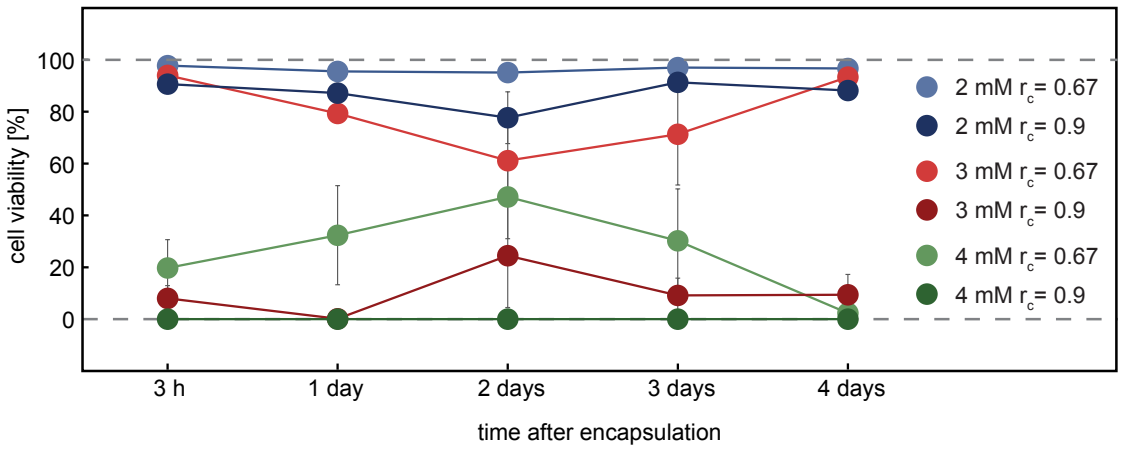

Figure 4.8.: Cell viability of encapsulated HT-1080 cells. HT-1080 cells are encapsulated in hydrogel strips of varying composition for four days. Results represent mean and standard deviation of three measurements.

5. Cell Migration in Strained Synthetic Hydrogels

In the last decades, an increased effort has been made to understand the mechanosensitivity of cells and how cues from the ECM guide cell behavior and influence cell migration. In this chapter, the impact of deformations, created in a 3D synthetic hydrogel environment, on proteolytic cell migration is analyzed. It is well known that cells react to static as well as cyclic deformations of their environment when encapsulated in a matrix or seeded on 2D substrates [177, 178]. In naturally derived gels, like collagen, alignment parallel to an external static strain is explained by fiber alignments and the strain stiffening observed in these gels [179, 180]. However, in highly cross-linked synthetic hydrogels, there are no fibers present which can align and the macroscopic strain stiffening in these gels is very small. Still, it was shown, that cells orient parallel to an external strain in such gels as well [181].
To better understand such cell guidance, a set-up to analyze cell migration in strained synthetic hydrogels is described in this chapter. First, the used system is characterized, followed by cell migration experiments comparing the migration direction of HT-1080 fibrosarcoma cells to the external strain direction. In a next step a theoretical model is implemented and calibrated with experimental data. This model reproduces the experimentally observed migration behavior and explains it by analyzing the matrix stiffness on the cellular scale. This chapter is in large parts based on the publication by Dietrich et al. [161].

5.1. Uniaxially strained gels are prepared by anisotropic swelling of micro-structured hydrogels in confinement

Strained hydrogels are prepared using the photo-lithographic micro-structuring of synthetic hydrogels in channel systems described in chapter 3. Small gel strips of 400 µm width and 5 mm length are polymerized in 400 µm high channels with HT-1080 cells embedded at a concentration of $6.7\text{x}10^5$ cells/ml. As analyzed in section 4.1, these strips

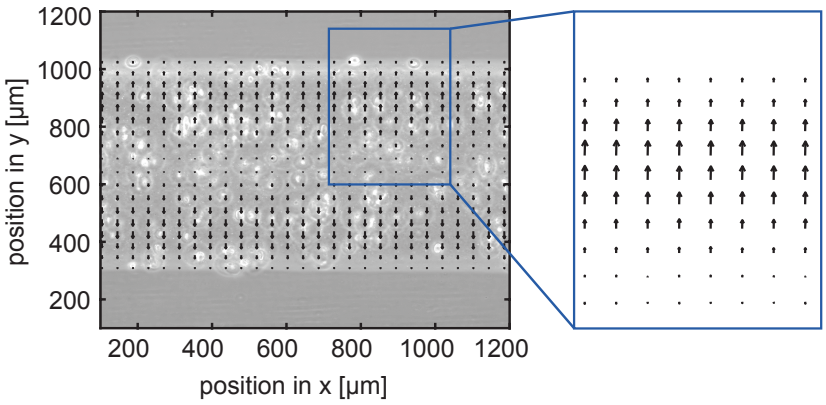

Figure 5.1.: Velocity vector field of the swelling process in the middle part of a strip. A phase-contrast image of the longitudinal middle section of a gel strip is overlayed with the velocity vector field derived from PIV analysis. The accumulated velocity vector field over the first 2h of the swelling process of a 2mM gel with a cross-linker ratio of 0.65 is displayed. The close-up illustrates the displacement of the gel only parallel to the short axis of the strip. The figure is adapted from [161] with permission from the Royal Society of Chemistry.

swell anisotropically. In the middle 20% of the longitudinal section of the strip the gel swells only parallel to the short axis of the gel (see figure 5.1) due to the confinement of the structures in a channel slide.

This anisotropic deformation of the strip creates a uniaxial strain γ_s in the network, which can be calculated according to equation 5.1 by measuring the strip width after swelling (W_{end}) and knowing the initial width of the strip ($W_0 = 400\mu m$). Together with equation 4.1, the swelling strain can be calculated from the swelling ratio r_{sw} :

$$\gamma_s = \frac{W_{end} - W_0}{W_0} = r_{sw} - 1. \tag{5.1}$$

It is known from polymer physics that the cross-linking degree has a big impact on the swelling behavior of polymer networks. With increasing cross-linking, the swelling of networks decreases. Therefore, a broad spectrum of strains is accessible in the set-up used in this work by changing the cross-linker ratio of the polymer solution. In figure 5.2 the measured strain induced in different hydrogel strips through swelling in PBS is shown. With decreasing cross-linker ratio the strain in the gel increases almost linearly for hydrogels containing 2mM and 3mM PEG-NB. A direct comparison with other literature values is not possible, as other publications that analyze swelling of synthetic hydrogels use unconfined bulk samples to calculate the volumetric swelling ratio as previously discussed in section 4.2. For very small cross-linker ratios and thus very high strains, a strain limit of 1.5 is determined by the structures on the chromium mask. Multiple 400µm strips are polymerized parallel to one another. As the initial strip distance is 1000µm, the gel can not reach a width after swelling bigger than that. Thus, strains above 1.5 are not possible in the system used in this work.

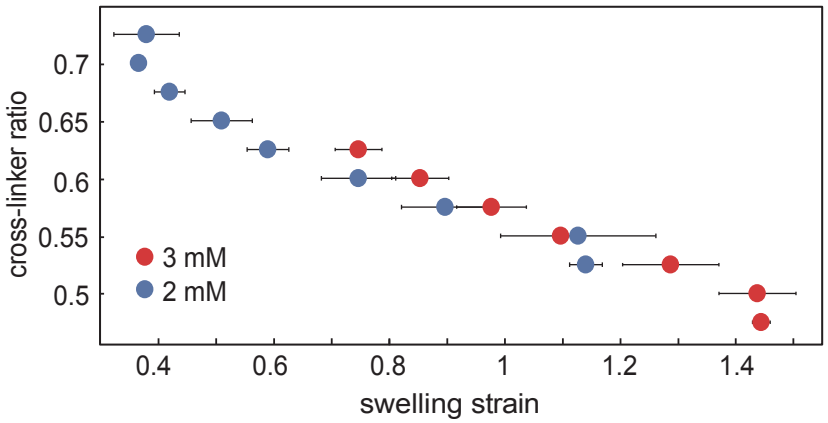

Figure 5.2.: Swelling strains induced in gel strips. 400µm wide hydrogel strips with a different degree of cross-linking and 2mM (blue circles) or 3mM (red circles) PEG-NB swell in confinement and induce a uniaxial strain in the gel. The figure is adapted from [161] with permission from the Royal Society of Chemistry.

A draw-back of the system is that the different strains are realized by changing the gel composition. Varying the cross-linker ratio not only changes the swelling ratio, but also influences the stiffness (see section 4.3) as well as the mesh size of the gels. However, an advantage of the system is that no laborious set-up is needed to strain the gel. In other studies, gels are clamped in devices to stretch the network, using e.g. magnetic fields. Often these set-ups are custom-build, highly complex and hard to combine with simultaneous microscopic monitoring of the cell movement [178, 182, 183]. The set-up in this work, on the contrary, is easy to use, can be easily reproduced in other labs and can be combined with live cell imaging. The used channel slides offer an excellent optical quality and are designed for microscopic imaging. Another advantage of the system is the uniaxial strain field produced in the network. When gels are stretched to induce a strain, complicated strain fields are obtained as a stretch in one direction leads to contraction of the network in the other dimensions of space [178, 183–185]. As the strain in this set-up is induced by an uniaxial swelling of the hydrogel, no simultaneous contraction occurs, which facilitates further migration analysis and their interpretation.

5.2. Alignment of migration direction to the external strain depends non-monotonically on the strain magnitude

To analyze how cells move in strained synthetic hydrogels, HT-1080 fibrosarcoma cells were encapsulated at a concentration of $6.7 \text{x} 10^5$ cells/ml in hydrogels strips containing 2–3mM PEG-NB and an off-stochiometric amount of MMP-degradable peptide cross-

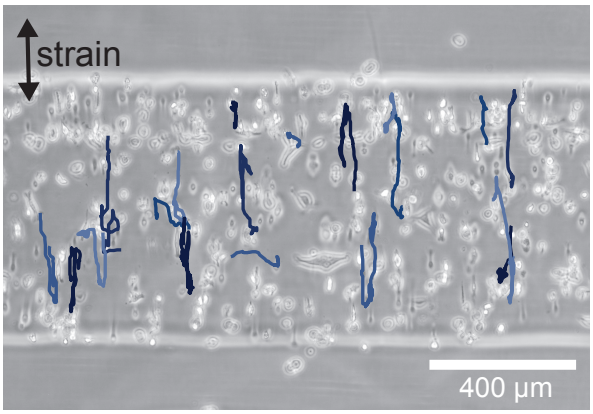

Figure 5.3.: Cell trajectories of HT-1080 cells migrating in 2mM 0.6 gels for 24h. Overlay of a phase-contrast image of the longitudinal middle section of a hydrogel strip (PEG-NB concentration of 2mM and cross-linker ratio of 0.6) with cell trajectories obtained over 24h. The figure is adapted from [161] with permission from the Royal Society of Chemistry.

linker, as well as 1mM CRGDS-peptide to enable cell adhesion. The gels were micro-structured in 400µm wide strips in 400µm high channels. The time-lapse images of the longitudinal middle section of the strips were recorded, starting 3h after hydrogel polymerization to ensure that the gel has reached its equilibrium swelling. By tracking the position of the cells over 24h, cell trajectories are obtained. An overlay of a phase-contrast image of a gel strip with such cell trajectories is displayed in figure 5.3.

With increasing cross-linker ratio, the percentage of migrating cells in the gel strips decreases significantly (see figure 5.4). Higher cross-linking increases the network density, which hampers cell migration in the gel due to the very small mesh size of the synthetic gel. Thus, migration analyses in hydrogels with very low strain are not possible.

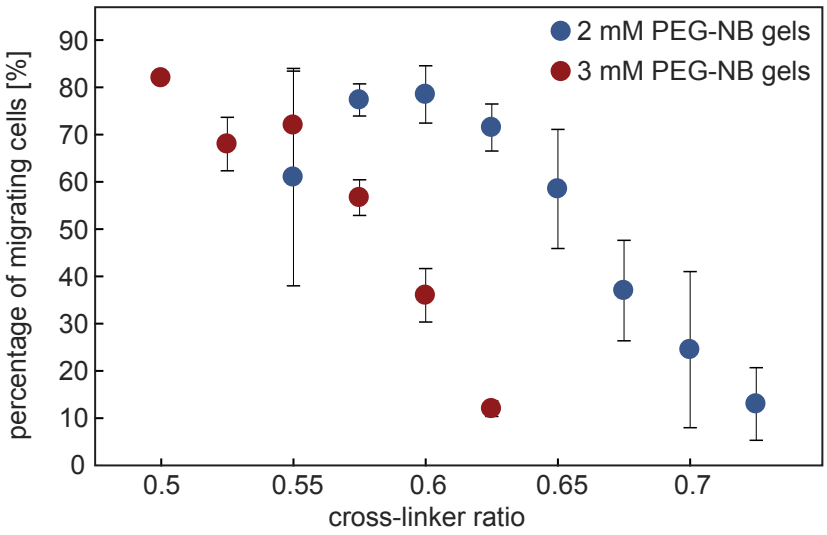

Figure 5.4.: Percentage of migrating HT-1080 cells embedded in hydrogel strips of different composition. All tracked cells which migrated less than 40µm in 24h were considered non-migrating. The figure is adapted from [161] with permission from the Royal Society of Chemistry.

Analyzing the migrating cells shows that embedded HT-1080 cells preferentially migrate parallel to the external strain direction for all strain magnitudes tested (see centered trajectories in figure 5.5). However, higher strains seem to decrease the alignment and result in more isotropic cell migration.

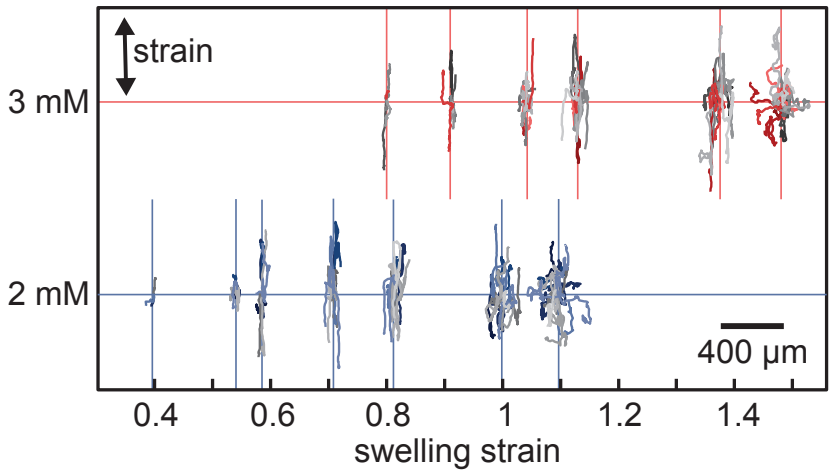

Figure 5.5.: Centered trajectories of HT-1080 cells migrating in various hydrogel strips for 24h. Overview of exemplary trajectories of HT-1080 cells migrating in differently strained hydrogels with a PEG-NB concentration of 2mM (blue) or 3mM (red). The figure is adapted from [161] with permission from the Royal Society of Chemistry.

It was already shown by others that cells align to an external static strain when embedded in a 3D synthetic matrix [181]. The degree of cell alignment thereby can depend on the strain magnitude. Li et al. showed that the orientation of NIH-3T3 cells embedded in a strained synthetic matrix depends on the strain magnitude as well as on the matrix stiffness [178]. However, they did not perform migration analysis, but only analyzed the cell orientation of fixed samples. Furthermore, no explanation is given for the observed behavior in synthetic networks.

In naturally derived gels, cell alignment and cell migration along an external static strain is explained by gel fibers that realign with the external strain and guide cell orientation [180]. Moreover, naturally derived gels are non-linear elastic materials which exhibit a strong strain stiffening [179, 186]. This macroscopic stiffening along the strain direction as well as an observed softening in the compressed direction [187], can lead to a durotactic cell orientation along the strain [19]. On the contrary, highly cross-linked synthetic hydrogels do not show a strong macroscopic strain stiffening [184, 188] and there are no fibers in the network that can align to an external strain. Nonetheless, HT-1080 cells migrate preferentially parallel to the strain in this work. To understand this observation, and the reason for a more isotropic movement at high strains, a theoretical model was implemented in the framework of a collaboration to simulate cell migration in a synthetic network and understand the underlaying guidance mechanism.

5.3. Simple theoretical model of a durotactic, proteolytic cell migration on a 2D lattice

The model described in the following sections was implemented by Hugo LeRoy and David B. Brückner in the group of Prof. Chase P. Broedersz (LMU Munich). It models a proteolytic, durotactic cell migration in a spring network.

The network in the theoretical model

To capture the basic physical processes of cell migration and mechanosensing in strained synthetic hydrogels, a system-level description of a cell moving through an elastic network is used. In this work, the matrix is described by a coarse-grain model of a triangular lattice network with grid nodes connected by linear springs. The elastic energy of this network is given by a Hamiltonian

$$H = \frac{k}{2}\sum_{i=0}^{N}\sum_{\langle ij\rangle}(|r_\mathrm{i} - r_\mathrm{j}| - l_0)^2, \tag{5.2}$$

with r_i and r_j being the vector positions of a node i and its neighbors j, with the sum running over all nearest-neighbor pairs of nodes. The springs in the network have an elastic constant k and a rest length l_0. To introduce intrinsic disorder in the network, random springs are removed with a probability *1-P*, which results in an average number of bonds Z connected to a node of Z=*6P*. If not stated otherwise, a connectivity of Z=4.8 is used in this work, as this connectivity is above the isostatic threshold of 4 for 2D lattices and thus results in a macroscopically rigid network.

As a durotactic cell movement is modeled, the local rigidity of the network is important. In the model, the local network stiffness is defined by a tensorial stiffness of the network nodes:

$$k_{uv}^{(i)} = \frac{f_\mu^{(i)}(\delta x_v)}{(\delta x_v)}. \tag{5.3}$$

The displacement of a node i by a distance δx_v in direction v causes a restoring force of the network $f_\mu^{(i)}(\delta x_v)$ in direction u. For the cell in the model the stiffness magnitude $\bar{k}$, calculated according to equation 5.4, is the relevant local stiffness parameter.

$$\bar{k} = \frac{\parallel f_\mu^{(i)}(\delta x_v) \parallel}{\parallel (\delta x_v) \parallel}. \tag{5.4}$$

To introduce an external strain in the network, the lattice is stretched prior to cell migration simulation. Before stretching, the network is rotated by 15° to avoid an alignment of the stretch direction with a lattice axis.

Cell migration in the model

The cell in the model is a bodyless point moving from lattice node to lattice node. Therefore, trajectories derived from the model are coarse grained versions of a real cell migration. To model cell movement in polymer networks, the key aspects of cell migration have to be considered. Cells adhere to their environment and interact with the network. This enables them to probe the matrix to assess the mechanical properties as well as to exert forces on the network. Movement through the matrix typically drives cells from soft to stiffer regions, a phenomenon called durotaxis. Furthermore, to enable cell migration in matrices where the mesh size is significantly smaller than the cell diameter, cells have to partially digest the environment to create enough space for moving the cell body through the mesh. In collagen networks it was shown that matrix digestion of HT-1080 cells is localized shortly behind the leading edge and near the cell body, thus spatially separated from cell adhesion and force generation [83]. This spatial separation is also transferred to the model by localizing the force generation on the second nearest neighbors of the cell (see yellow dots in figure 5.6 B) and cleaving bonds to the first neighbors (see gray dots in 5.6 B).

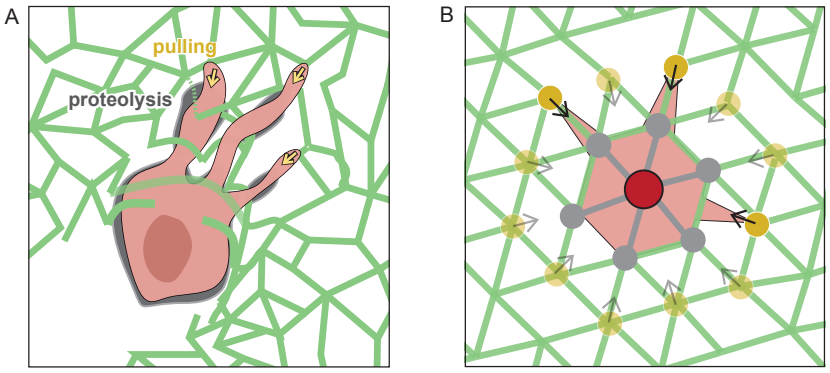

Figure 5.6.: Transfer of cell migration aspects from reality to the model. (A) Illustration of a cell in an inhomogeneous matrix. Adhesion and force generation is illustrated in yellow at the cell front. Proteolysis is depicted in gray behind the leading edge and near the cell body. (B) Schematic overview of the network in the model. The cell center (red dot) sits on a node of a triangular lattice network, pulls on its second nearest neighbors (yellow) and can cleave bonds to the first neighbors (gray). The figure is adapted from [161] with permission from the Royal Society of Chemistry.

Within one computational migration cycle the following steps are performed to mimic cell migration (see also figure 5.7): 1) The cell pulls on its second nearest neighbors and contracts the network. 2) The local stiffness $\bar{k}$ of the nearby lattice nodes is calculated and 3) the cell center moves to the nearest neighbor with the highest local stiffness. 4) Lattice bonds next to the cell are deleted at a fixed proteolytic rate r_{p}. For every modeled cell, if not stated otherwise, 100 of these migration cycles are performed to retrieve a cell trajectory.

Using these four simple steps, the model simulates cell migration on a 2D elastic lattice.

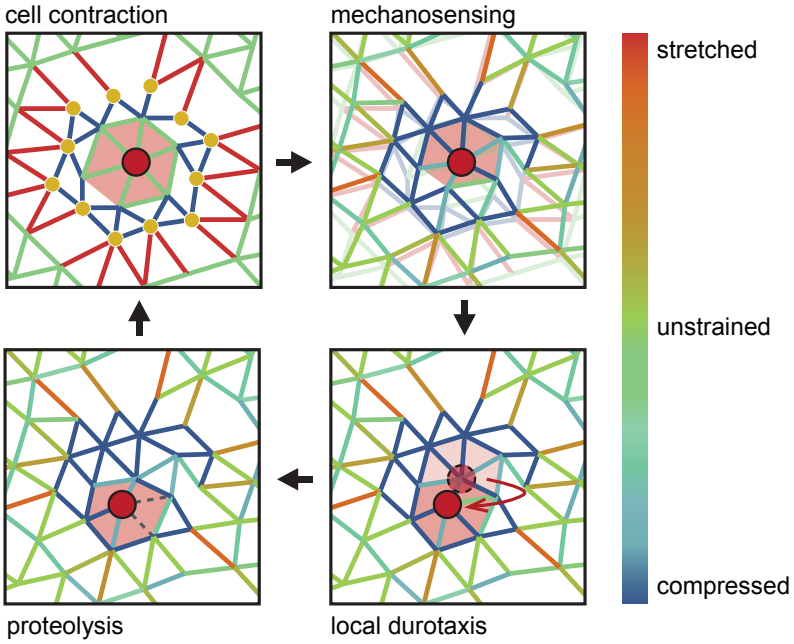

Figure 5.7.: Illustration of the cell migration cycle used in the model. Four basic steps form a migration cycle in the model. 1) Cells contract the network by pulling on neighboring nodes (yellow dots). 2) The local network stiffness is calculated. 3) Cells move to the stiffest nearest neighbor. 4) Some bonds to the nearest neighbors are deleted (dashed lines). The figure is adapted from [161] with permission from the Royal Society of Chemistry.

5.4. Calibration of the model with isotropic experimental migration data

An important parameter of the model is the proteolytic rate r_p, which determines how many bonds on average are cleaved in one computational circle. It can be varied from zero to six. However, very high proteolytic rates result in a complete disintegration of the network. This would impede a good comparison with cell migration in 3D networks. Therefore, by keeping r_p small, the modeled 2D migration can be compared to 3D experiments.

To verify the model and calibrate the proteolytic rate used for further analysis, a comparison of the simulation with isotropic, unstrained migration experiments was performed. For this, big hydrogel slabs were polymerized in an open system and were allowed to swell freely floating in swelling solution and only immobilized on a surface after swelling was completed. Hydrogel slabs with a PEG-NB concentration of 2mM and a cross-linker ratio of 0.6 were used. The degradability of the hydrogels was changed by substituting parts of the MMP-degradable cross-linker with non-degradable PEG-dithiol cross-linker. With increasing PEG-dithiol ratio in the gel, more and more cross-links cannot be cleaved by cells, which makes cell movement more difficult in the matrix. In figure 5.8 cell trajectories of HT-1080 cells moving in gel slabs with different degradability are displayed, illustrating that with decreasing percentage of cleavable

cross-links cell migration is hampered. But even with only 40% degradable bonds, cells are still able to move through the network, but the obtained trajectories are much shorter than in completely degradable conditions.

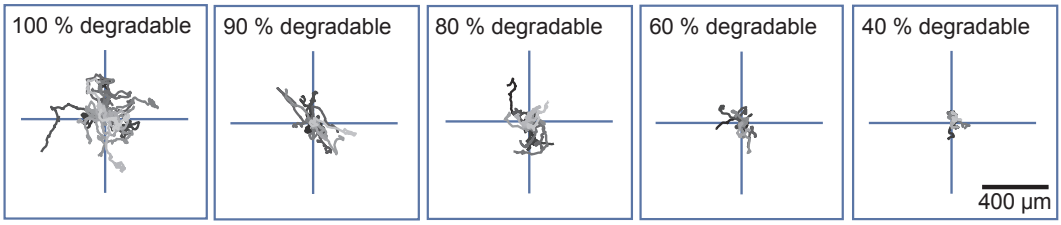

Figure 5.8.: Centered trajectories of HT-1080 cells migrating in isotropically swollen hydrogel slabs of different degradability. HT-1080 migration is monitored for 24h in gels (2mM PEG-NB and a cross-linker ratio of 0.6) with different percentages of degradable to non-degradable cross-linkers. The figure is adapted from [161] with permission from the Royal Society of Chemistry.

To calibrate the model, different proteolytic rates from 0.5 to 3 were tested in the simulation with 50 simulated cells per condition and compared to the isotropic experimental data. Mean square displacement (MSD) as well as velocity autocorrelation function (VACF) analysis are basic migration parameters describing cell migration and are herein used to validate the model. In the simulation as well as the experiments, the MSD increases with time as an approximate power law with an exponent of around 1.4–1.8 (see figure 5.9). This indicates a super-diffusive behavior, which is typical for cell migration [52, 189]. In the experimental data, the exponent does not change with decreasing degradability of the network. However, the overall MSD does slightly decrease. This is in good agreement with the cell trajectories in figure 5.8, where shorter trajectories for gels with a decreased degradability are visualized.
In the model, the exponent of the apparent power law of the MSD increases for increasing proteolytic rates r_p from 1.4 to 1.8. An increase indicates a more persistent migration of the cells. Interestingly, no cell polarization and therefore persistence in cell migration is implemented in the model. This phenomenon arises from the deletion of bonds in the modeled migration cycle. Cleaving bonds decreases the local matrix stiffness of the network, thus the durotactic cell in this model is prone to move away from its previous position. This results in a persistent movement. With a higher proteolytic rate, more bonds are deleted in every cycle which reinforces the persistent migration and explains the higher exponent.
The existence of a persistent migration in the model is also visible in the VACF (see figure 5.10). For the experimental data, as well as the simulation, the VACF decays with a characteristic time, indicating persistent movement of the cells. For very low proteolytic rates the VACF of the simulations seems to slightly oscillate, an artefact from the simulation. Nonetheless, the VACF of the model is very similar to the experimental data.

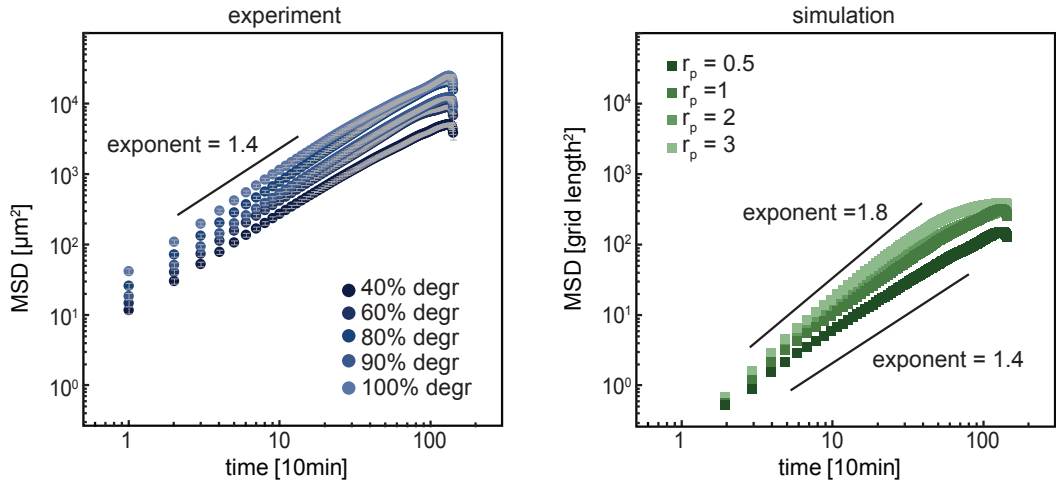

Figure 5.9.: Mean square displacement analysis of experimental and simulated data in unstrained networks. MSD analysis of HT-1080 migration in unstrained hydrogels with different degradability (left graph) is compared with analysis from simulations using different proteolytic rates r_p (right graph). The figure is adapted from [161] with permission from the Royal Society of Chemistry.

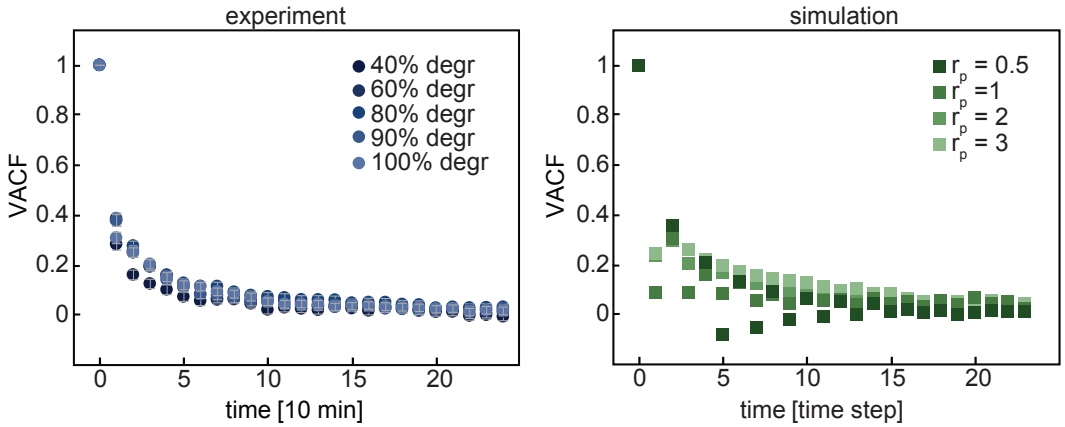

Figure 5.10.: Velocity autocorrelation function of experimental and simulated data in unstrained networks. VACF of HT-1080 migration in unstrained hydrogels with different degradability (left graph) is compared with analysis from simulations using different proteolytic rates r_p (right graph). The figure is adapted from [161] with permission from the Royal Society of Chemistry.

Small differences in the described analyses can be attributed to slightly different set-ups between experiment and model. In the model, the proteolytic rate, which influences the number of bonds that will be cleaved, is changed, whereas in the experiments the percentage of bonds that can be cleaved is varied. This is not an exact comparison, but changing the ratio of cleavable cross-links in the hydrogels can be done in the experiments in a controlled way. Inhibition of the MMP activity, which would resemble a changed proteolytic rate in the experiments, can be done by the addition of inhibitors in the cell culture medium. However, no defined inhibition of e.g. 50% of the MMP activity can be realized and often these inhibitors also slightly change the overall behavior of the cells due to complex inhibitor interactions [190, 191]. Consequently, the more

controlled variation of the gel degradability was used in this work for a comparison with the model.
The quantification of the migration statistics of simulated and experimental data verified the implemented model, showing that in an isotropic system migration behavior similar to experimental observations can be simulated. For further studies in strained systems a proteolytic rate of r_p=1 is used in the model if not stated otherwise and hydrogels are formed using 100% degradable MMP-cross-linkers.

5.5. Analysis of the migration anisotropy in the experimental and theoretical data

After validating the implemented theoretical model in unstrained networks, migration simulations were performed in uniaxially strained networks of varying magnitude. Simulated cell movement in an unstrained and strained network is displayed in figure 5.11A as overlays of lattice networks with the exemplary cell trajectories. A clear distinction between unstrained and strained matrices is visible as the strain leads to higher heterogeneities in the matrix.

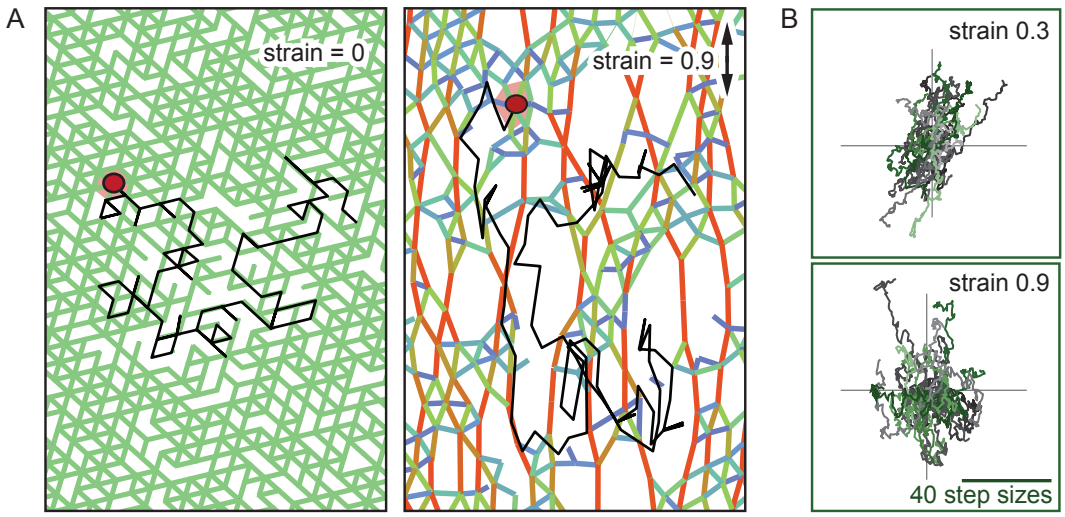

Figure 5.11.: Cell migration tracks of the simulations in strained networks. (A) Overlay of unstrained and strained lattice networks with an exemplary cell trajectory. Cell center is marked with a red dot. (B) Centered trajectories of simulated cells in two differently strained networks. The figure is adapted from [161] with permission from the Royal Society of Chemistry.

As a first comparison between experiments and simulations in uniaxially strained networks, calculations of the MSD were performed. Analysis of the experimental data, introduced in section 5.2, and simulated data are displayed in figure 5.12. For all data sets, the MSD increases over time as an approximate power law with an exponent of around 1.4. This is in good agreement with results obtained from isotropic networks.

The overall MSD does not change for different strains in the simulations and most strains in the experiments. However, the lowest strains in the 2mM and 3mM PEG-NB gels result in a smaller overall MSD. This can be explained by the gel which is used to achieve low strains. As discussed in section 5.1, low strains are obtained from higher cross-linked gels. These hydrogels thus have a higher cross-linker density, smaller mesh sizes and are stiffer than less cross-linked gels. Therefore, it is more laborious for cells to migrate through the network which is reflected in the smaller overall MSD values.

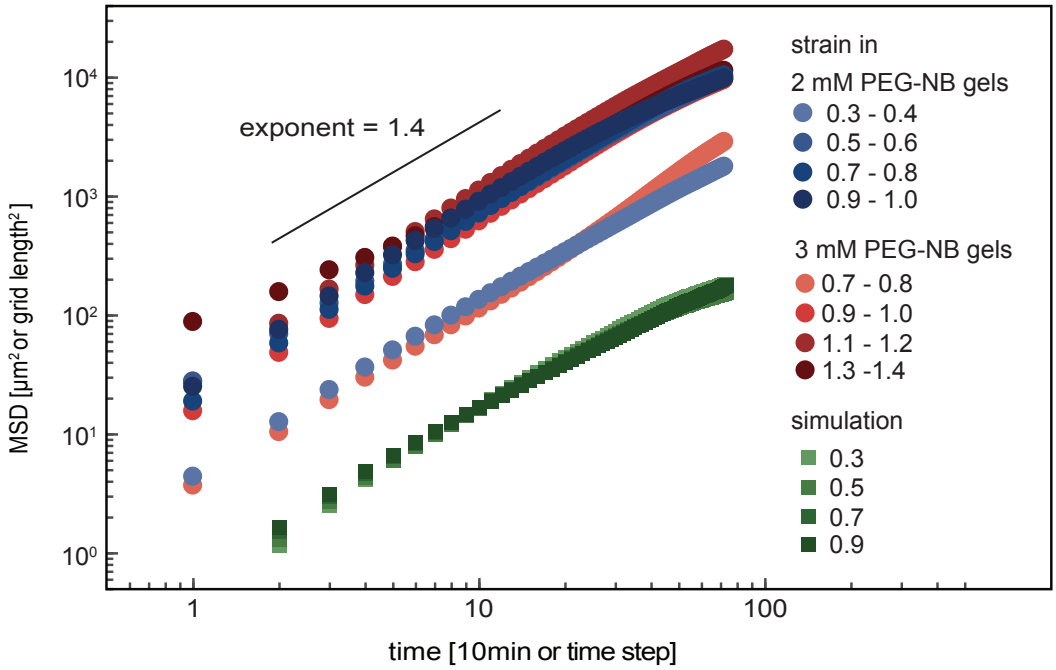

Figure 5.12.: MSD analysis of experimental and simulated cell migration in strained matrices. For the experiments, migration data for different strains were binned and displayed in blue for 2mM PEG-NB hydrogels and red for 3mM PEG-NB gels. Simulated data is displayed in green. The figure is adapted from [161] with permission from the Royal Society of Chemistry.

Having a closer look at the cell tracks in figure 5.11B, cell trajectories in the simulation show a preferred orientation parallel to the external strain direction at intermediate strains and a more isotropic distribution at high strains, as already observed for the experimental data in figure 5.5.

To be able to better compare experimental and simulated data, the degree of anisotropic migration was quantified. For every cell the coordinates at every time point x_{t_i} and y_{t_i} are recorded and the total distance traveled by cells parallel, $D_{\parallel}$, and perpendicular, $D_{\perp}$, to the external strain direction are calculated.

$$D_{\parallel} = \sum_{i=1}^{T} \mid y_{t_{i+1}} - y_{t_i} \mid \tag{5.5}$$

$$D_{\perp} = \sum_{i=1}^{T} \mid x_{t_{i+1}} - x_{t_i} \mid \tag{5.6}$$

An anisotropic migration index (AMI) is defined by comparing the total distance migrated by cells parallel and perpendicular to the external strain direction.

$$AMI = \frac{D_{\parallel} - D_{\perp}}{D_{\parallel} + D_{\perp}} \tag{5.7}$$

The maximum AMI value that can be reached is 1 for cells which only move parallel to the strain, whereas AMI = 0 is calculated for an isotropically moving cell. To correctly compare experiments and simulations, the AMI calculated for the simulated data has to be corrected. First, as the modeled cell moves from lattice node to node, the distance traveled parallel to the strain has to be corrected for the network deformation according to equation 5.8 using the applied strain γ. Otherwise the AMI would be biased towards positive values.

$$D_{\parallel,corrected} = \frac{D_{\parallel,measured}}{\gamma + 1} \tag{5.8}$$

Secondly, as the external strain direction is not aligned with any lattice axis, the simulated cell cannot solely migrate parallel to the strain direction, but its movement always has a perpendicular component as well. Thus, a simulated cell could never reach the maximal AMI of 1. To correct for that, the AMI is normalized to the maximal AMI, AMI_{max}, that can be reached in the simulation.

$$AMI_{normalized} = \frac{AMI_{model}}{AMI_{max}} \tag{5.9}$$

With an angle between the lattice axis best aligned with the external strain and the strain direction of 15° an AMI_{max} of 0.577 is reached. After correcting the simulated AMI accordingly, experiments and simulations can be directly compared (figure 5.13). Experimentally, cell migration in isotropically swollen 2mM gel slabs has an AMI of 0, which indicates isotropic migration as expected. Migration in intermediately strained gels reaches an AMI of 0.6, indicating highly anisotropic migration parallel to the strain direction as already visible in the cell trajectories in figure 5.5. With increasing strain, the calculated AMI decreases and cell migration is more isotropic. The response of cells in 3mM gels is shifted to slightly higher strain levels compared to the 2mM gels, but shows the same tendency. It is known that the stiffness and the mesh size in these gels differ, which might explain the small shift. Nonetheless, in both gels, higher strains lead to a more isotropic migration. Interestingly, this non-monotonic behavior is also observed in the implemented model. Without strain, the simulated cells move isotropically in the network. With increasing strain, cell movement is oriented along

the strain direction before at very high strains, cells migrate more isotropic again (see figure 5.13).
The maximal AMI achieved in the model is, with a value of around 0.4, smaller than values observed in experiments, thus cell migration in the model is less anisotropic than in the experiments. Nonetheless, the model qualitatively captures the non-monotonicity of the anisotropic migration response of HT-1080 cells migrating in strained hydrogels very well.

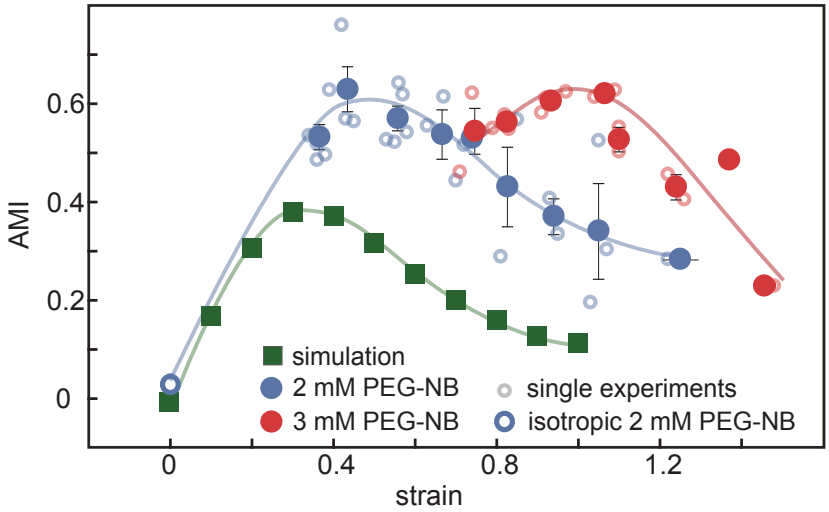

Figure 5.13.: Anisotropic migration index of cells migrating in uniaxially strained matrices. The anisotropic migration index (AMI) of experimental and simulated cells is depicted depending on the strain in the network. Each single experiment is displayed as small circles and binned data by filled circles (blue for 2mM gels, red for 3mM gels). Simulated data is shown in green. Error bars represent standard error of the mean. The figure is adapted from [161] with permission from the Royal Society of Chemistry.

There are some differences between the model and the experiments that can explain the smaller AMI of the simulated data. First of all, cell polarization was neglected in the model. If the cell persistence depends on the strain or stiffness in the system, the implementation of a polarization in the model can increase the achieved AMI. This hypothesis was tested by altering the decision making process in the simulation and analyzing the AMI values reached in networks with a strain magnitude of 0.3. In this altered model, the cell does not only consider the node stiffnesses of its first neighbors of the current simulation cycle, but averages the measurements of the last N_{av} cycles and decides according to this average measurement where to move. In total 200 cells with 50 migration steps each were simulated for different N_{av}. To calculate the AMI displayed in figure 5.14 only migration steps after initial N_{av} steps are used. This time-averaged mechanosensing will lead to a more persistent migration and increases the migration parallel to the strain. With a N_{av} of 20–30, AMI values similar to the experiments can be reached. Thus, the lack of cell polarization in the minimal model is one reason for the lower AMI compared to the experiment.

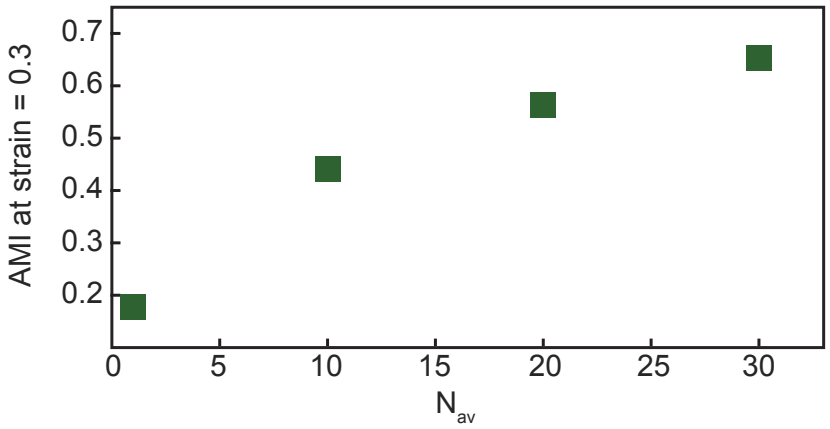

Figure 5.14.: Anisotropic migration index for cell migration simulation with time-averaged mechanosensing. The anisotropic migration index (AMI) is displayed at a strain of 0.3 for cells performing durotactic migration in a polarized model based on averaging the stiffness measurements over the last N_{av} computational cycles. The figure is adapted from [161] with permission from the Royal Society of Chemistry.

Another factor that can influence the migration in strained matrices in the experiment is the mesh size differences in the strained synthetic hydrogel. In the swelling process, the hydrogel network expands and the mesh size of the polymer network increases. However, in the set-up described in this work, gel expansion only occurs uniaxially, thus the mesh size of the network is anisotropic. This can direct the cell movement parallel to the expansion direction. Furthermore, in the model, the cell randomly digests nearby bonds. In experiments, however, it was shown that the sensitivity of collagen towards MMPs or other collagenases that cleave the fibers was altered under strain [111, 192–194]. This suggests that the digestion of hydrogel cross-links in the experiments can be influenced by the strain applied to the network and trigger an anisotropic migration. Yet, all these factors should scale monotonically with an external strain. The non-monotonic dependency of the migration direction to the applied strain suggests that the strain triggers another mechanism in the matrix that acts as guidance cue for embedded cells, which non-linearly depends on the strain magnitude.
As the non-monotonicity was also detected for the data generated by the minimal theoretical model, a closer look at the simulation and guidance cues provided in the model might help to understand the cell migration in strained matrices.

5.6. Non-linear local strain stiffening in the model guides cell migration

The cell in the implemented model performs a durotactic movement, which means that the cell moves to the neighboring node with the highest local stiffness. This is the only criteria for the modeled cells when deciding where to go. Therefore, the local stiffness

of the modeled network is analyzed in more detail in this section to elucidate how the stiffness is influenced by the macroscopic strain and if the stiffness can explain the observed non-monotonic cell behavior.
The local stiffness of the nodes in the network were probed by positioning a cell on a node in the matrix and letting it contract the network. Then, the tensorial stiffness of the nodes is measured and thereafter, the local stiffness magnitude $\bar{k}$ for every node is calculated. This way the cell measures the local stiffness of the network in different orientations to the external strain direction. In figure 5.15 the relative local stiffness of the modeled network in various directions to the local strain is displayed for different external strain magnitudes. The first interesting observation is that the stiffness of the network nodes increases with increasing strain. Even though the network consists of linear springs which show no strain stiffening effect, an increase in the strain magnitude results in higher node stiffnesses.

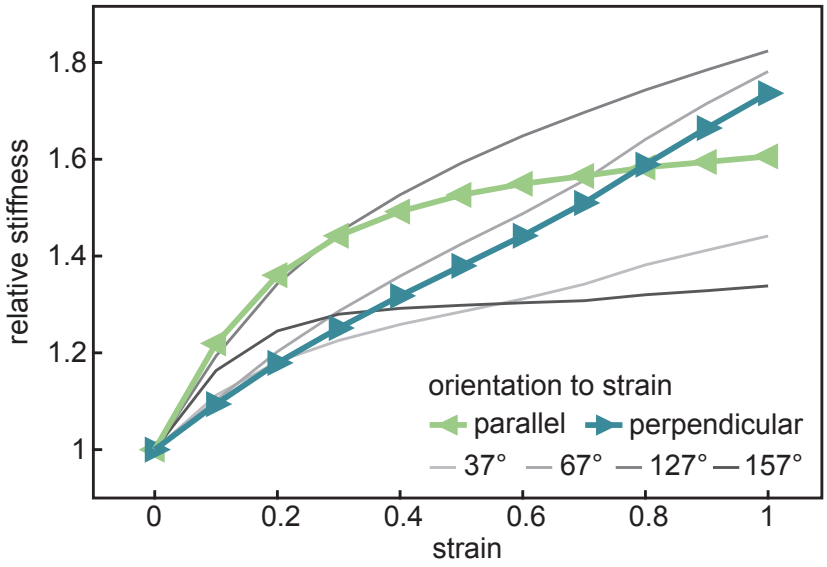

Figure 5.15.: Local stiffness measurements in the modeled network. Local relative stiffness probed by the modeled cell in different orientations to the external strain direction. Directions parallel and perpendicular to the the strain are displayed in green and blue respectively. The figure is adapted from [161] with permission from the Royal Society of Chemistry.

Secondly, the observed stiffening is anisotropic. The node stiffness probed perpendicular to the external strain direction increases linearly. This can be attributed to the tension built in the springs along the strain direction and is analogous to a guitar string, where higher tension increases the force necessary to pluck the string. The node stiffness parallel to the external strain shows a fast increase for small strains and approaches a plateau for high strains. Such a stiffness mechanism was previously described in these networks for the macroscopic response to external strain [195–197]. It can be explained by intrinsic heterogeneities in the bond density of such networks. Some regions can have a locally decreased connectivity, which renders such locations floppy and therefore

soft. However, the external strain pulls the regions out and they start contributing to the network stiffness, which explains the fast increase of the stiffness at small strains. The described anisotropic stiffening of the network nodes in the model explains the non-monotonicity of the AMI very well. The modeled cell always moves to the neighboring node with the highest stiffness. At low strains, the stiffest migration direction is parallel to the strain (see figure5.15), which results in an increased AMI. At higher strains, other migration directions are stiffer and cells move less in parallel direction to the external strain. This decreases the AMI and results in the non-monotonic cell behavior observed in the simulation.

The same analysis described for the model is difficult to perform in the synthetic hydrogel. Direction-dependent microrheological analyses in the gel are hard to realize. Studies with atomic force microscopy are not suitable as the channel used to confine the gel micro-structures impedes the use of contact-based measurements. Magnetic and optical tweezers or the use of passive rheology analyzing the Brownian motion of embedded beads are also not suitable in the described set-up, as the overall network stiffness is too big to detect enough bead displacement [174, 198, 199]. Thus, unfortunately, no stiffness measurements could be performed in the experimental set-up described in this work. Nonetheless, the results obtained from the model together with the very similar responses of experimental and simulated cells to the external strain suggest that local strain stiffening also plays an important part in the anisotropic migration of HT-1080 cells in uniaxially strained hydrogels.

5.7. Conclusion

In this chapter, a set-up to uniaxially strain a hydrogel and study the migration of embedded HT-1080 cells was introduced. A photo-induced polymerization reaction of a synthetic hydrogel, together with photo-lithography was used to micro-structure small hydrogel strips into channel slides. Due to the high aspect ratio of the strips and the confinement in the channel slide, the inherent swelling of the cross-linked gel was restricted to one direction. This induced a uniaxial strain in the network, which was verified by PIV analysis. By changing the composition of the hydrogel, the swelling and thereby the induced strain can be tuned. The embedded fibrosarcoma cells preferentially migrated parallel to the external strain direction. A maximal alignment of the migration direction to the strain is reached at strain values of 0.5 and 1 for gels containing 2mM or 3mM PEG-NB, respectively. At higher strain magnitudes cell migration is more isotropic again.

To understand this non-monotonic behavior, a simple theoretical model was implemented in the framework of a collaboration. The body-less cell in the model moved from lattice node to node on a triangular network, performing a durotactic, prote-

olytic cell migration. Before applying an external strain to the lattice, the system was calibrated with isotropic experimental data. In the strained system, the simulation produced very similar results to the experimentally observed cell migration. The non-monotonic dependency of the migration direction relative to the external strain direction with increasing strain was also observed in the model. To elucidate the underlying guidance mechanism the local stiffness of the modeled network was analyzed and showed a local, anisotropic strain stiffening effect, which explains the behavior of the durotactic cells.

The combination of the described experimental set-up and the implemented model provides the opportunity to understand cell guidance in strained matrices. Using microstructured gel strips inside microscopy channels does not only redundantize active straining of the gel with a laborious device, but also provides very good optical accessibility to monitor cell migration. Other studies that utilize complicated straining devices to generate an uniaxial strain without or with small compressions perpendicular to the strain direction, often lack the possibility to perform time-lapse imaging of the embedded cells [177, 184, 200]. Therefore, often only the cell alignment of cells is analyzed but not directly the migration of the cells. Furthermore, in a lot of studies, no explanation for the observed cell behavior is given [178, 181]. This partially is attributed to the very complex mechanism of cell guidance, as many factors influence cell migration, like the cell type used, stiffness of the network, matrix composition, adhesion motifs or diffusion gradients in big hydrogel slabs. Reducing the complexity of the matrices used in such studies can help to concentrate on specific possible guiding mechanisms.

The use of artificial hydrogels is one important step to reduce the complexity of an experiment. The composition of these gels can be fine-tuned in contrast to collagen or other naturally derived gels where e.g. the concentration of cell adhesion motifs like RGD sequences, cannot be influenced. Furthermore, natural gels are more heterogeneous in their overall network structure compared to gels formed by a radical step-growth polymerization. In collagen gels, fibers and bundles are formed which can align to an external strain and bias cell migration in one direction [166]. Such fibers do not exist in highly cross-linked synthetic gels. Additionally, the mechanical properties of the natural gels are more complicated as they show a pronounced macroscopic strain stiffening.

The linear elastic property of synthetic polymer networks is one advantage when analyzing fundamental guidance principles in strained networks, as it is believed that the stiffness of the matrix does not change when the gel is stretched. However, as shown by the local stiffness analysis in the model implemented in this work, macroscopic properties of a matrix and its local properties on the cellular scale might not always be the same. This finding is not only relevant when analyzing how cells are guided

by external strain, but has to be considered in other applications and for other matrix properties as well. Arnold et al. e.g. showed that the spatial distance of presented adhesion molecules on the nanoscale is crucial for the formation of focal adhesions and therefore for cell attachment and migration [201]. This is just another example where considering the local matrix cues rather than macroscopic properties is important to better understand cellular behavior.

6. Migration of Cancer Cells in Pressurized Hydrogel-Hydrogel Clefts

In the previous chapter, proteolytic cell migration inside a synthetic hydrogel was studied. However, *in vivo* cells cannot always digest their surrounding to move through the ECM. They sometimes have to squeeze through small pores or into clefts, thereby deforming the network to make enough room for the cell body to displace. If the pores are too small or the pressure acting on cells is too high, cell migration is suppressed.
Systems to analyze such cell migration often use small structures made of PDMS to observe how cells squeeze through µm confinements [52, 53, 202]. PDMS structures are considerably stiffer (few kPa to few MPa) than most *in vivo* tissue (0.1–30kPa) [203], which is desirable in these applications as the cell deformability is analyzed rather than matrix deformation. Other set-ups use softer gels, mostly agarose to compress cells and exert forces on them. In these assays, agarose is pressed on a cell culture surface and cells squeezed between the surfaces are analyzed [204, 205]. To migrate in these systems, cells have to deform the agarose.
To analyze non-proteolytic cell migration in a more *in vivo* like environment, the formation of pressurized clefts between two hydrogels (called sponge clamp) is described in this chapter and cell invasion into these clefts is analyzed. By using the photo-lithographic structuring of synthetic hydrogels described in chapter 3 and taking advantage of the inherent swelling of the gel structures, pressurized clefts can be formed. After quantifying the compression of the gels generated in the system, HT-1080 migration into the clefts, as well as a comparison between HT-1080 and MDA-MB-231 invasion, is studied as proof of concept.

6.1. Formation of hydrogel clefts by swelling of gel strips

The pressurized hydrogel-hydrogel interfaces are formed inside a 70µm high commercially available channel slide by photo-lithographic micro-structuring of synthetic hy-

drogels as described in chapter 3. Before polymerization of the hydrogel inside the channel, the surface of the channel was decorated with PEG-dithiol molecules (method described in section A.1.2). This was necessary to covalently bind the hydrogel to the surfaces, thereby stabilizing the structures and preventing a displacement of the gel upon swelling. Furthermore, immobilization of PEG molecules passivates the surface and inhibits cell attachment [206, 207].
Strips of 100µm width and 700µm length were polymerized parallel to each other in small initial distances D. As already discussed in section 2.3.2, hydrogels swell after polymerization and increase their volume, especially in direction of the short axis of the strip. If strips are spaced sufficiently, they can swell until they reach their equilibrium swollen state with an end strip width of W_{end} (see figure 6.1 A). By using an initial spacing smaller than (W_{end}), the swelling is hampered by neighboring strips, which results in the formation of multiple parallel sponge clamps (see figure 6.1 B). The clefts are under pressure due to the swelling pressure of the hydrogel.

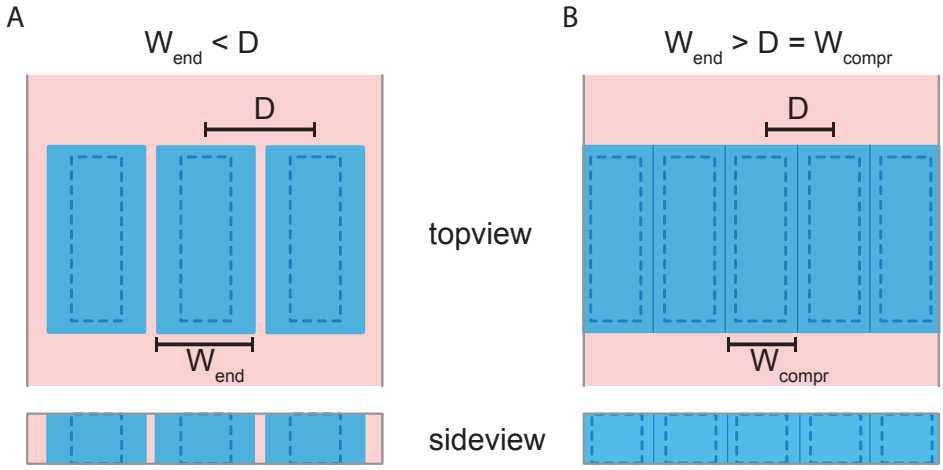

Figure 6.1.: Schematic overview of hydrogel strips with different initial strip distances D inside a channel. Hydrogel strips are displayed in blue, with dashed lines indicating the initial strip dimensions before swelling. (A) Strips with an initial distance D bigger than the width after equilibrium swelling W_{end} can swell completely without touching neighboring strips. (B) If D is smaller than W_{end}, gels encounter neighboring gels while swelling and are restricted in their swelling process. Only a final strip width W_{compr} = D can be reached.

In this work the described set-up was used to analyze the invasion of cells into the sponge clamp. As the cells should deform the network to squeeze into the cleft and not just digest the matrix to form migration tracks, the cross-linkers used in these experiments are 1kDa PEG-dithiol molecules which cannot be digested by cells. To enable cell adhesion to the gel via integrins, 1mM of the small CRGDS peptide is incorporated in the matrix. Due to the passivated surface of the channel system, cells in the experiments can only adhere to the gel, not to the slide material. This is one driving force for cells to migrate into the clefts. In addition, a chemotactic gradient of

fetal bovine serum (FBS) was established in the channel slide which further guides cell invasion into the pressurized clefts. In figure 6.2, a schematic of the set-up, as well as a brightfield image of an array of pressurized hydrogel clefts is displayed.

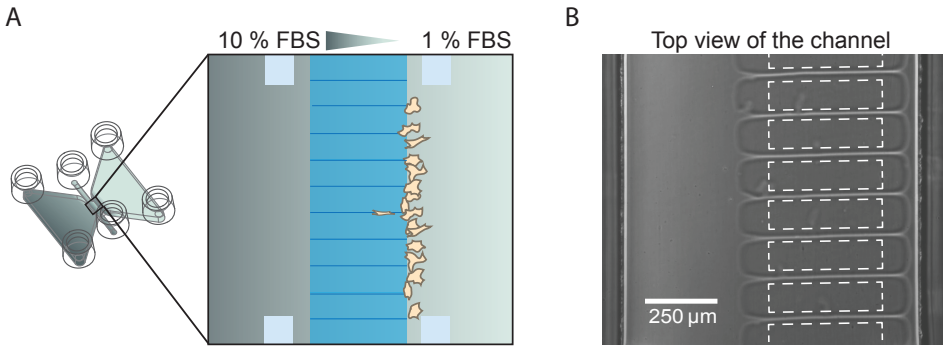

Figure 6.2.: Set-up of a sponge clamp. (A) Schematic of the sponge clamp set-up. Hydrogel strips are polymerized in the 70µm high channel of a µ-Slide chemotaxis (ibidi), where a linear gradient of serum guides cell migration into the clefts. (B) Phase-contrast image of formed sponge clamps without cells. White dashed lines indicate the initial strip dimensions before swelling.

6.2. Estimation of the compression in the clamp

The swelling of hydrogel strips in the 70µm high channel slides is analyzed to estimate the hydrogel compression achieved in the sponge clamp. In a first step, strips are polymerized with a high distance D of 250µm, to measure the equilibrium swelling of uncompressed hydrogels. This way, the strips can swell normally and the width after swelling, W_{end}, is measured for different cross-linker ratios. With increasing cross-linker ratio, the swelling decreases. However, for the highest cross-linker ratio tested, a small increase is observed (see figure 6.3).
To estimate the amount of compression built in a sponge clamp, C_{gel}, the width of normally swollen gels W_{end} is compared to the compressed width of the strips W_{compr}:

$$C_{\mathrm{gel}} = \frac{W_{\mathrm{end}} - W_{\mathrm{compr}}}{W_{\mathrm{end}}} \tag{6.1}$$

As the initial strip distance D determines W_{compr} if D$<W_{end}$, equation 6.1 can be rewritten as

$$C_{\mathrm{gel}} = 1 - \frac{D}{W_{\mathrm{end}}} \tag{6.2}$$

Thereby, the compression of the gel is estimated by measuring the width of normally swollen gels and knowing the initial strip distance in the sponge clamp set-up (see figure 6.3 B). Thus, the dependency of the compression on the used cross-linker ratio follows the same trend as the measured width W_{end} in figure 6.3 A, with higher cross-linker

ratios resulting in slightly smaller compressions. Decreasing the initial strip distance, increases the compression built in the sponge clamp. Hence, to change the compression in the set-up, the initial strip distance or the cross-linker ratio can be varied. With the set-up used in this work, compression values from 0.08 to 0.26 can be reached (see figure 6.3 B).

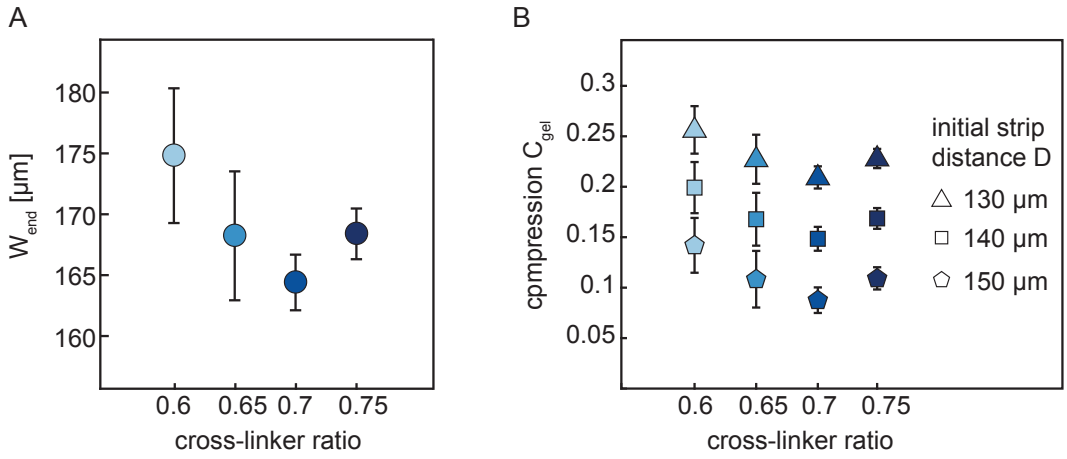

Figure 6.3.: Analysis of the compressions build in sponge clamps. (A) W_{end} of strips with high initial strip distance are measured to estimate the swelling. (B) From W_{end} displayed in (A), compressions, C_{gel}, in sponge clamps formed with different initial strip spacings D are calculated. Results show mean with standard deviation.

To reach compressions higher than 0.26, either the cross-linker ratio has to be reduced, which results in stronger swelling, or a smaller initial distance between the strips is necessary, which reduces the space available for gel expansion. The use of lower cross-linker concentrations is problematic, as less cross-linked gels are softer and therefore, less stable. This results in deformed structures that cannot be used as sponge clamps in cell experiments. Small strip spacings to increase the compression are also difficult to achieve, as scattered light in the simple photo-lithographic set-up used in this work results in polymerization of the gel in between the desired strips. A more sophisticated, but also expensive set-up, e.g. a mask-aligner, might achieve a better resolution. Nonetheless, one always has to consider that, in order to form structures inside a channel system, the parallel light passing a photo-mask does not directly penetrate the hydrogel solution, but first has to pass the bottom or top of the channel. This reduces the spatial resolution that can be achieved in such systems. In this work e.g. the system is illuminated through the bottom of the µ-slide which has a thickness of 180nm. This will always limit the resolution of photo-lithographic structuring inside the channel.

One approximation in the presented calculation of the gel compression in sponge clamps is the use of phase-contrast images of low magnification to measure the strip width. These W_{end} measurements are mean values over the entire channel height. When taking a series of fluorescent images at different heights from the channel bottom, a z-profile

of the gel strip can be reconstructed which shows that the strip width varies to some degree depending on the distance to the channel bottom (see figure 6.4). The half-width of normally swollen gels illustrates that the strip has a curved boundary, with smaller width close to the channel bottom. This also means that the calculated compression in the sponge clamp is not equal over the channel height and smaller compressions are realized close to the bottom compared to the middle of the channel.

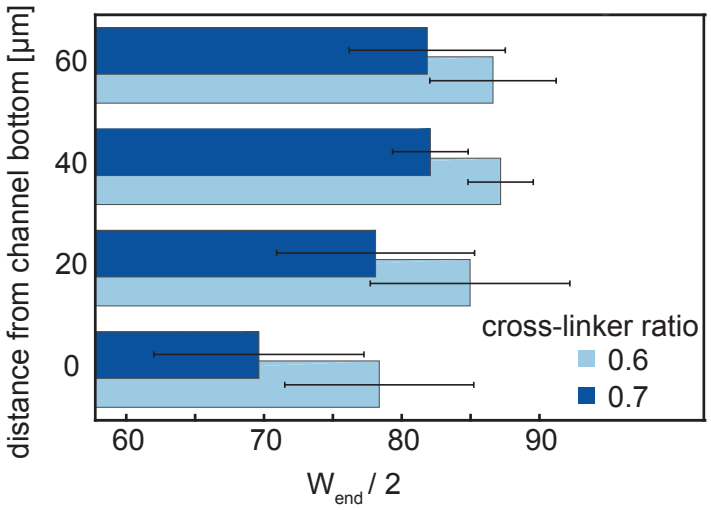

Figure 6.4.: z-profile of swollen hydrogel strips with big initial distance D. Example z-profiles of two swollen gels with high initial strip distance D and different cross-linker ratios. $W_{end}/2$ is displayed to illustrate the z-profile. Gels close to the bottom, where they are covalently bound to the channel surface, swell less compared to the middle of the channel height. Results show mean with standard deviation.

Overall, calculating the compression according to equation 6.2 is a good approximation for forces acting in the sponge clamp. However, to be able to calculate the pressure acting on the cells inside the clamp and thereby knowing exactly which forces the cells need to be able to displace the gel, the stiffness of the gels has to be known. As already discussed in section 4.3 measuring the stiffness inside the channel slide is very challenging and was not conducted in this thesis. The stiffness measurements in section 4.3 do only represent approximations of the micro-structured gel stiffness and show the well-known trend of higher stiffness for more cross-linked gels. As the degree of swelling also influences the gel stiffness, analysis of the exact values for the gel rigidity would have to be performed directly in the sponge clamp set-up as swelling is, in addition to the confinement in the channel, hampered by neighboring gels. Consequently, when comparing sponge clamps with different compressions, it always has to be considered that by changing the cross-linker ratio or the strip to strip distance, also the stiffness of the gel is varied. This can have a great influence on the cell invasion behavior.

6.3. HT-1080 migration into clefts shows sponge clamp effect

To show that cells can invade into the sponge clamps, HT-1080 fibrosarcoma cells were added to one side of the clamp and a chemotactic gradient from 1 to 10% FBS was applied across the gel to induce directed migration into the clefts. Figure 6.5 A shows a sponge clamp directly after the addition of the cells and 40h afterwards. Cells moved into the clefts as single cells and pushed the gel aside to make room for the cell body. This was confirmed by fluorescent microscopy of gels with embedded small fluorescent beads and the use of HT-1080-LifeAct cells, which allow the visualization of the actin structure in the cell (see figure 6.5 B).

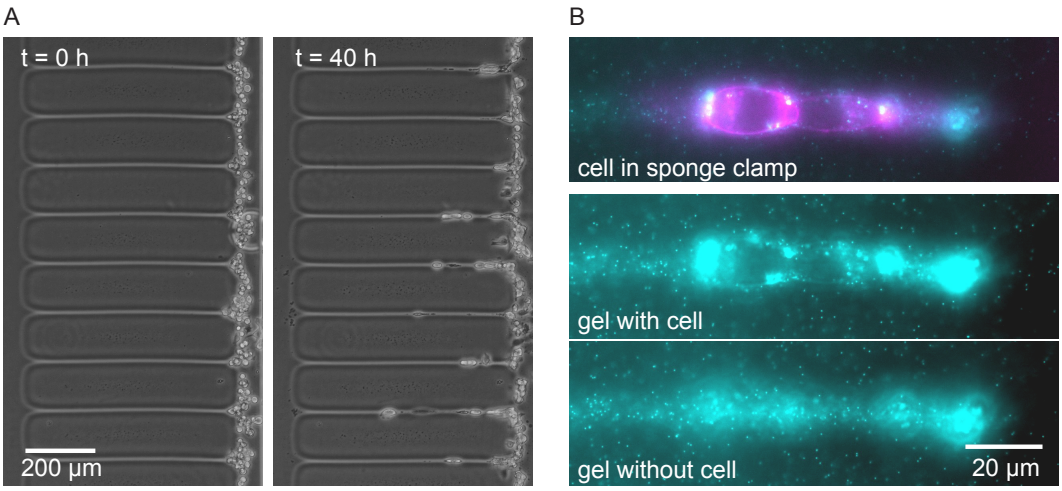

Figure 6.5.: Invasion of HT-1080 cells in sponge clamps. (A) Phase-contrast images of a set of sponge clamps formed by hydrogel strips polymerized with 2mM PEG-NB with a cross-linker ratio of 0.6 and an initial strip distance of 140µm. The image on the left shows the clamps directly after cell seeding and image on the right 40h after cell seeding. (B) Fluorescent images of HT-1080-LifeAct cells inside a sponge clamp. In the picture on the top, actin structures are displayed in magenta and the gel is visualized through small embedded beads in turquoise. The two images on the bottom show only the beads in the gel at the same position with and without a cell. After removing the cell from the cleft, the gel relaxes back and closes the room formally taken up by the cell.

To analyze the invasion depth of cells into the clefts, only the first cell entering a cleft was tracked. Following cells were not analyzed as their movement might be influenced by the leading cell. Therefore, one invasion track was recorded for every cleft and analyzed together with the tracks from the other parallel sponge clamps. In total four cross-linker ratios with three different initial strip distances were used to generate pressurized hydrogel-hydrogel interfaces. The mean invasion tracks for the different conditions are displayed in figure 6.6 and already illustrate that higher initial spacings, which means less compression, facilitates cell invasion. A clear trend concerning the influence of the cross-linker ratio is not directly visible from these tracks.

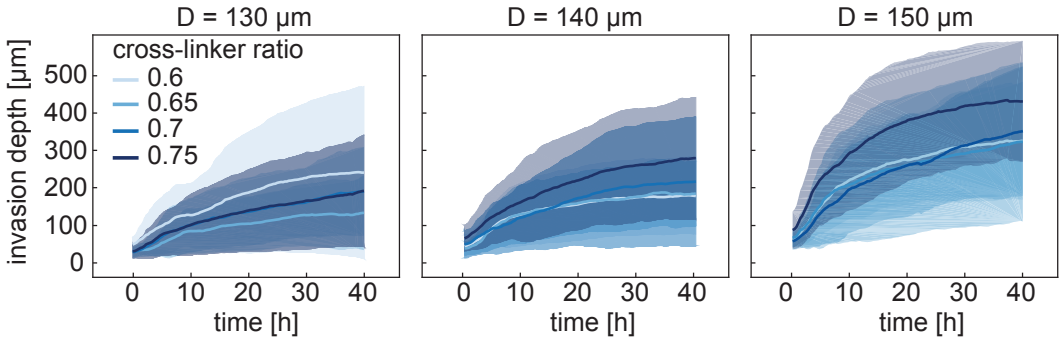

Figure 6.6.: Mean invasion tracks of HT-1080 cells migrating into different sponge clamps. Different cross-linker ratios and initial strip distances were used to form sponge clamps with different gel compressions. With increasing initial spacing, the cell invasion depth increases. Lines show mean value and shaded areas the standard deviation.

For further discussions, only the invasion depths after 40h are considered to simplify the comparison between different conditions. Figure 6.7 A shows the invasion depth depending on the calculated gel compressions in the set-ups. A trend towards less invasion in higher compressed clefts can be seen. However, the increase is not significant within each cross-linker ratio condition. Nonetheless, less invasion in higher compressed clamps is reasonable, as cells need to exert more pressure on the gel to push the matrix aside.

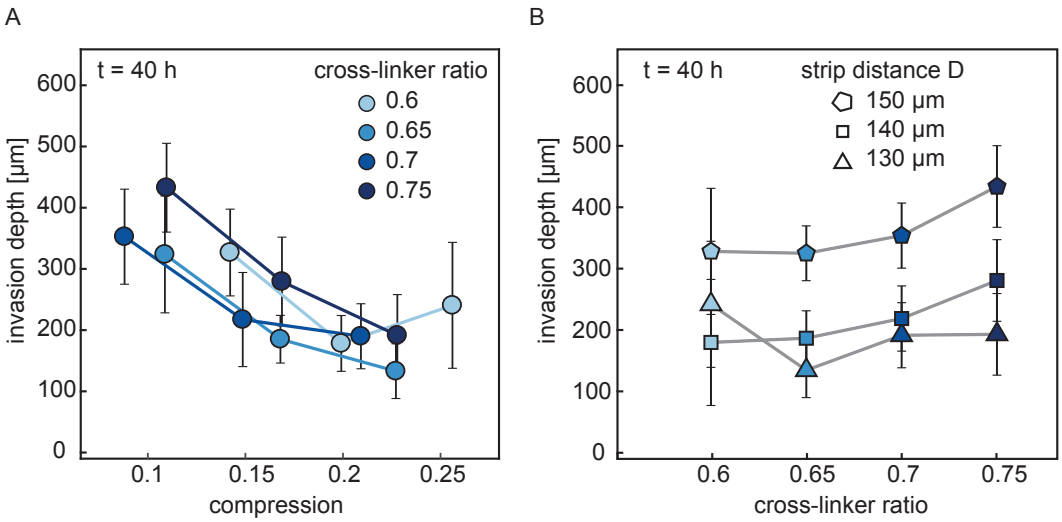

Figure 6.7.: Invasion depth of HT-1080 cells into sponge clamps. (A) The invasion depth after 40h depending on the gel compression is plotted for sponge clamps with varying cross-linker ratios. Results show mean value with standard error. (B) Same data plotted against the cross-linker ratio used to form the sponge clamp. Marker shape indicates the initial strip distance, D, used to achieve different gel compressions with the same gel composition.

Plotting the same data versus the used cross-linker ratio shows a small trend towards higher invasion in stronger cross-linked gels (see figure 6.7 B). This, on the one hand, can be attributed to the smaller swelling of higher cross-linked gels or, on the other

hand, might be influenced by the higher stiffness of gels with higher cross-linking degree. These two effects influence the pressure built in the clamps differently. Less swelling decreases the compression in the system, whereas stiffer gels increase the force necessary to push the hydrogel aside. Furthermore, one has to consider that cells in a sponge clamp do not only have to push the gel aside, but also have to move the cell body forward when invading into the clefts. This movement can be achieved through pulling on the gel, mediated by matrix bound integrin binding peptides. In traction force microscopy, cells on stiff 2D substrates exhibit a stronger contraction force compared to cells on softer substrates [208, 209]. Hence, a more rigid gel might facilitate the forward movement of cells in the clefts.

6.4. Invasion capacity of MDA-MB-231 cells into sponge clamps is smaller compared to HT-1080 cells

To further validate the sponge clamp set-up, another cancer cell, MDA-MB-231, a human breast adenocarcinoma cell line, is compared to the invasion of HT-1080 fibrosarcoma cells. Both cell types are highly invasive, with and without proteolytic digestion of their surrounding matrix [52, 210, 211].
Gels with 2mM PEG-NB and cross-linker ratios of 0.6 and 0.7 were used to form gel strips with an initial spacing of 140 and 150µm. For all conditions tested, HT-1080 migration was considerably faster in the first hours of the experiment compared to MDA-MB-231 cells. At later time points, both cell types had a comparable invasion speed (see slope of the mean invasion track for sponge clamps built with a cross-linker ratio of 0.6 and an initial strip distance of 140µm in figure 6.8 A). The reason for this can be manifold. Slower cells at the beginning of the experiment can be explained by stressed cells that still have to recover from the detachment procedure [212]. The detachment of cells with trypsin solution destroys cell-surface interactions, amongst others integrins, which are important for effective cell migration. It is known that a medium cell-substrate adhesion results in the highest migration speed [213]. Thus, for MDA-MB-231 cells, after trypsination, the integrin concentration might be too low for a fast migration, whereas for HT-1080 cells, the decreased ligand concentration on the cell surface might enhance the migration speed. Lautscham et al. also showed that a smaller fraction of MDA-MB-231 cells compared to HT-1080 cells entered narrow constrictions formed in PDMS, yet invasion depth and speed were comparable [52]. Thus, the low mean cell invasion of MDA-MB-231 at the beginning can also be a result of non-invading cells blocking the entrance to the clefts until a cell that has a higher invasion potential enters the clamp and migrates efficiently.

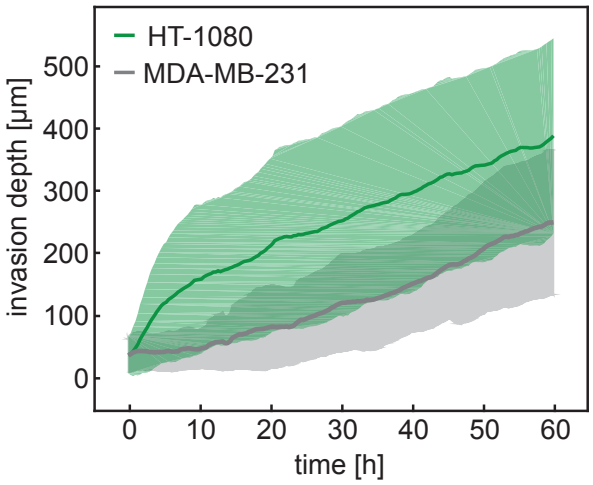

Figure 6.8.: Invasion depth comparison between HT-1080 and MDA-MB-231 cells. Example invasion profile of both cell types migrating into a sponge clamp polymerized with a cross-linker ratio of 0.6 and an initial strip distance D=140µm. Lines show mean value and shaded regions standard deviation.

Due to the lower invasion speed in the first hours of the experiment, the invasion depth of HT-1080 cells after 60h is always higher than for the MDA-MB-231. For both cell lines, a smaller compression does not increase the invasion depth (figure 6.9 A), and for more cross-linked gels, the invasion capacity decreases (figure 6.9 B).

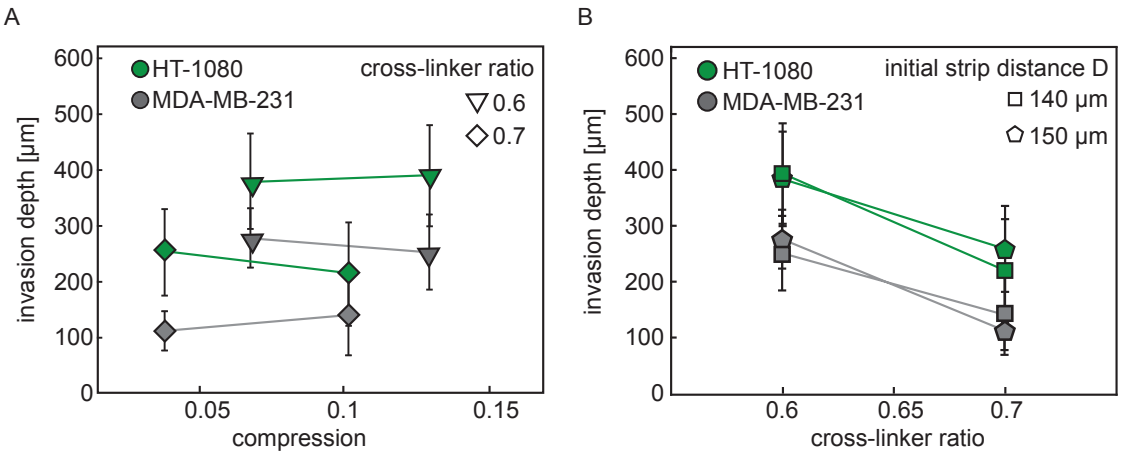

Figure 6.9.: Invasion depth of HT-1080 and MDA-MB-231 cells after 60h. Invasion depth after 60h depending (A) on the gel compression and (B) on the cross-linker ratio of the gel. HT-1080 data displayed in green, MDA-MB-231 data in gray. Shape of the markers indicate the cross-linker ratio and initial strip distance used, respectively. Results show mean with standard error.

Both these trends are inconsistent with previously observed behavior of HT-1080 cells described in section 6.3. There, an increase in compression resulted in a decrease in invasion and more cross-linked gels enhanced cell invasion to a small extent. However, only two cross-linker ratios and two initial strip distances were tested in the new experiments. Deriving accurate dependencies and extrapolations from such a small data set

is not possible. Nonetheless, some differences between the data sets and their possible causes are discussed.

An explanation for the discrepancy could be the different compression ranges that are obtained. In the first experiments, strip widths after swelling, W_{end}, between 165 and 175 µm were measured, whereas only 158 to 161 µm wide strips were formed for the new experiments (see figure 6.10). Thus, in the new clamps, lower gel compressions are achieved. A direct comparison between the invasion depth in the old and new experiments depending on the cross-linker ratio, is therefore not possible.

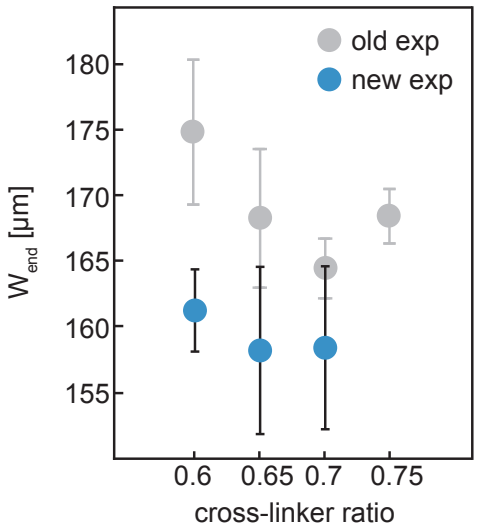

Figure 6.10.: Swelling analysis of the two gel batches used to form sponge clamps. End strip width, W_{end}, are displayed for hydrogel strips formed with different cross-linker ratios and high initial spacing to ensure equilibrium swelling of the structures. The new measurements are displayed in blue, results from the old experiments (invasion analysis of only HT-1080 cells, see figure 6.3 A) are displayed in grey to facilitate direct comparison. Results show mean values with standard deviation.

A reason for the different swelling behaviors in the two sets of experiments, can be the use of different stock solutions of the same monomer batch that were used. To prepare the polymer solution, first stock solutions of all components (they are solids in their dry form) are prepared, which are afterwards mixed to form the pre-polymer solution. This solution is then injected in the channels and illuminated to form the hydrogel. Due to the small volumes necessary and the high viscosity of PEG-NB stock solutions, a minimal difference in the concentration of the stock solutions is possible. This might explain the different swelling degrees for the same cross-linker ratio in the two sets of experiments.

The old data set shows that higher gel compressions hamper the cell invasion, however, for the very low compressions achieved in the new experiments, this trend cannot be observed. There are examples in the literature where a small compression of cells enhances their invasiveness compared to an uncompressed state [214]. Therefore, it is possible that at very low compressions cell invasion is low but increases rapidly for

slightly higher compressions, whereas at considerably increased pressure in the clefts, cell invasion is hampered. This would explain the observed invasion behavior of HT-1080 cells.
Furthermore, HT-1080 cells from two different cryovial cultures were used in the separate experiments. Even though the cryovials are from the same working cell bank, which means that they contain the same batch of cells, they might slightly differ. The cells are cultured according to standard operation procedures established in the lab to ensure constant cell quality and uniform handling of the cultures. Nonetheless, small variations are possible that might influence the cell behavior and can contribute to small variations between the two experiment sets [215].

6.5. Conclusion

In this chapter a set-up to form pressurized hydrogel clefts was introduced and used to analyze the invasion capacity of cancer cells into such sponge clamps. By photolithographic structuring of small, parallel hydrogel strips inside a channel slide and consecutive swelling of these structures, the pressurized gaps are formed if the initial strip spacing, D, is smaller than the strip width after swelling, W_{end}. The compressions realized in the gel can be varied by changing the cross-linker used to form the hydrogel and by the initial strip distance. Low cross-linker ratios and small initial spacings result in high compressions. The gels used to form these pressurized gaps cannot be degraded by cells as their backbone is completely composed of PEG molecules, but 1 mM of RGD peptides are incorporated to enable cell adhesion to the gel. The rest of the channel slide is passivated by covalent immobilization of PEG chains on the surface, whereby cells can only adhere to the hydrogel. A soluble FBS gradient over the formed sponge clamps directs cell migration into the clefts. As a proof of concept for this set-up, the non-proteolytic invasion of cancer cells into the pressurized gaps was analyzed.
HT-1080 cells readily invade into the clamp at low compressions, but invasion depths decreased with increasing compression. The cross-linker ratio used to form the gels also influences the invasion capacity. Higher cross-linking and therefore stiffer gels increase the migration depth of HT-1080 cells. However, when a new batch of hydrogel solution was prepared and HT-1080 migration was compared to MDA-MB-231 migration, these dependencies could not be reproduced. The swelling of the gel strips polymerized from the two different batches varies, which results in different compressions of structures formed with the same initial strip distance and the supposedly same cross-linker ratio. This might explain the discrepancies in the migration of HT-1080 cells in the two experimental sets. Nonetheless, a difference between HT-1080 and MDA-MB-231 invasion was observed. HT-1080 migration in the first hours of the experiment was faster than MDA-MB-231 movement until after less than 24h, the mean invasion speeds were

similar.
In these proof-of-concept experiments, a relatively low number of different conditions were tested, especially for the comparison between the two different cell lines. These limited sample sizes do impede a detailed analysis of the compression and stiffness dependencies on cell invasion. A broader range of compressions would enable a more thorough investigation of cell migration in pressurized hydrogel clefts. This could be achieved by higher numbers of different cross-linker ratios or overall PEG-NB concentration used to polymerize the gels, as well as an increased number of initial strip distances.
In order to understand the interplay between gel compression, pressure necessary to displace the gel and contraction forces that move the cell body forward, exact values of the matrix stiffness would be necessary. But, as already discussed before, these are very difficult to retrieve within the used set-up. Furthermore, the curved z-profile of the clamps complicates the analysis of cell invasion as the calculated compressions are just mean values over the whole channel height.
Despite the mentioned drawbacks and improvement possibilities, the proof-of-concept experiments realized in the introduced sponge clamp show that cancer cells can invade into pressurized clefts formed out of soft synthetic hydrogels by deforming the matrix. An easy analysis of the migration is possible due to the parallel, micro-structured clefts, which confine cell migration in quasi 1D. In the set-up, different ligands or ligand concentrations in the matrix can be realized, which is an advantage over under-agarose-invasion experiments, where adhesion ligand concentration is determined by the agarose concentration, which also affects the gel stiffness. Another advantage of the formed sponge clamps is the use of a commercially available channel slide, which is designed for microscopic analysis, thus allowing cell migration to be easily monitored. Overall, the implemented set-up to analyze non-proteolytic invasion of cells in pressurized clefts shows promising results. However, an improvement of the system and a more thorough investigation of the gel properties and forces acting on the cells in these sponge clamps has to be conducted to retrieve quantitative conclusions that will help to understand cell invasion dependencies.

7. Outlook

In the presented work, the photo-lithographic micro-structuring of synthetic hydrogels inside channel slides was introduced and the formation of advanced 3D matrices after swelling of the gel was used to study cell migration. Due to the modular design principle of the synthetic gel, matrices with different properties can be polymerized by incorporating small peptide sequences to enable interaction of cells with the otherwise bioinert gel backbone. Furthermore, it was demonstrated that the inherent swelling of the cross-linked synthetic hydrogels can be tuned by changing the gel composition, especially the cross-linker ratio. In addition to the micro-structuring of the gels, their swelling can be used to form complex hydrogel matrices for cell migration analysis.
In this thesis, the polymerization of thin strips with a high aspect ratio within a channel resulted in an anisotropic swelling of the gel which uniaxially strained the matrix. Proteolytic cell migration within the gel showed a non-monotonic dependency of the migration direction on the strain magnitude. With the help of a theoretical model, microscopic strain stiffening of the macroscopically linear elastic matrix was identified as an important guidance cue in such systems.
Due to the very good optical accessibility of the matrix inside the channel slide, high resolution microscopy of the migrating cells in a strained environment would be possible in the future. This is not feasible in most other set-ups used to analyze cell behavior in strained systems, as the complex devices are not suitable for live cell imaging [177, 184, 200]. High resolution imaging, in combination with fluorescence labeling of integrins or cytoskeletal components, enable a more thorough investigation of the migration mode and signaling mechanisms used by cells to move in strained 3D matrices. Furthermore, labeling of matrix cleavage sites can help to understand if an applied strain does alter the proteolytic degradability of fibers and thus is one guidance mechanism that steers cells in complex 3D matrices.
Another upgrade of the system in the future could be a combination of different guidance cues with the described set-up. For example, combining soluble or matrix bound growth factor gradients with strained gels. This is especially interesting as mechanical guidance has only been appreciated as an important influence on cell behavior in the last decades. Therefore, currently only a few studies deal with the combination of mechanical and e.g. chemotactic guidance mechanisms [12, 105].

Another application of the inherent swelling of parallel gel strips in a channel slide is the formation of pressurized hydrogel clefts to analyze the non-proteolytic cell migration into these sponge clamps. In proof-of-concept experiments the invasion of cancer cells was studied in this thesis and was shown to have a dependency on the magnitude of gel compression in the clamps. To improve the system and enable more quantitative analysis, a thorough investigation of the matrix stiffness in the set-up has to be realized in the future. However, up until now, no suitable analysis method is available as contactless measurements with optical or magnetic tweezers cannot be performed in the channel slides [216]. Passive rheology using the Brownian motion of entrapped beads as stiffness indicator is also difficult due to the relatively high rigidity and therefore very small bead movement that would have to be detected.

The curved z-profil of the strips in the sponge clamp set-up also complicates compression analysis. Hence, the use of two-photon-lasers to polymerize more sophisticated hydrogel structures, which are also structured in the z-direction, would improve the sponge clamps. The strip geometry could be adapted to produce an even compression along the hydrogel height.

The introduced sponge clamp set-up can also be adapted to other scientific questions by changing the composition and ligands presented on the gel backbone. By exchanging the adhesive peptide addressing integrins in normal cell migration with E-cadherins, the endothelial barrier of blood vessels could be mimicked in order to analyze intravasation of cancer cells. This would help to understand an important process in cancer metastasis, where cancer cells break through the wall of blood vessel to reach distant sites from the primary tumor. As the sponge clamp is polymerized inside a channel system, a controlled media flow can be established next to the hydrogel, which would enable the simulation of a blood flow in the system to also study extravasation of cancer cells from the blood stream.

Apart from the already implemented assays to analyze cell migration, the photo-lithographic micro-structuring can also be used in the future to fabricate other 3D matrices which are difficult to realize through micro-molding. Consecutive polymerization of multiple gels with different embedded cells can be used to form complex multi-cellular structures mimicking the composition and layout of tissue compartments or whole organs. In pharmaceutical drug research, organ-on-a-chip technologies are rapidly gaining importance to identify and test drug candidates. One important organ in drug testing is the liver, where many substances are metabolized [129, 217, 218]. Therefore, liver toxicity of drug candidates is a major rejection cause. Furthermore, the liver has a complex internal structure important for the correct function of the organ, which cannot be reproduced in 2D cultivation. Photo-lithographic structuring of the different liver components in a channel slide, which enables an easy perfusion

of the formed structure, can help to build such organoid models at some point in the future.

An easier approach to mimic 3D tissues is the use of spheroids, globular cell aggregates. For long-term survival as well as easy drug application, a micro-fluidic accessibility in combination with a positioning of the spheroids is desirable. To achieve this, the in-situ polymerization of hydrogel chambers to capture spheroids, but retain fluidic access to the cells, could be used (see figure 7.1).

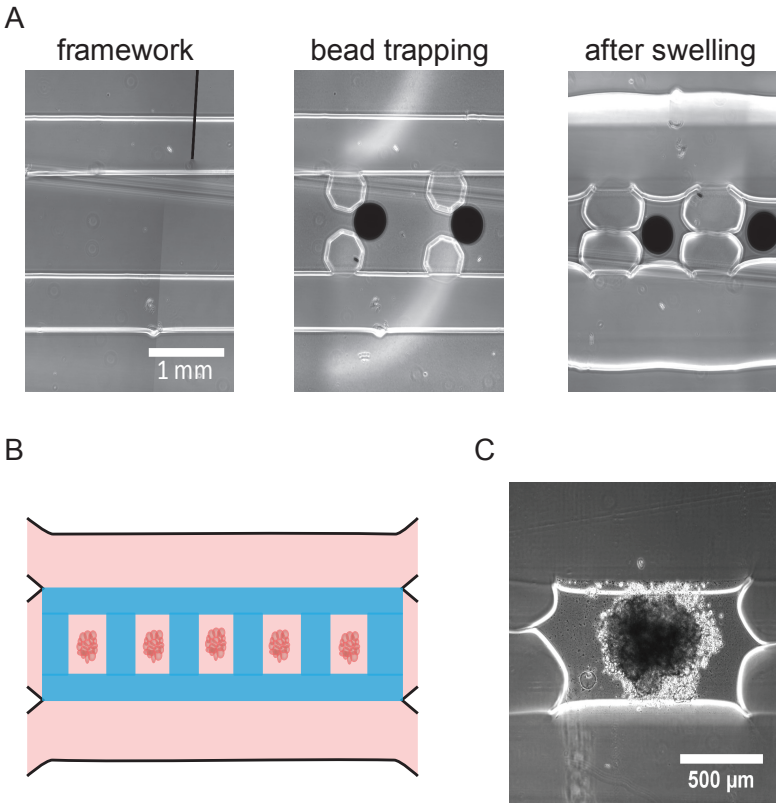

Figure 7.1.: Possible future encapsulation system for spheroids. (A) Different steps for entrapping beads as surrogates for spheroids. First, a framework structure is polymerized by photo-lithography. Afterwards, beads in pre-polymer solution are flushed into the channel and small pillars are polymerized close to each other to entrap the beads. After washing the channel with media, the unpolymerized solution is flushed out of the system and the gel swells, which closes the gap between the pillars and thereby forms closed hydrogel chambers. (B) Schematic of multiple spheroids entrapped in hydrogel chambers. Via the channel slide, different solutions can be flushed into the system. (C) A MCF-7 spheroid after four days in a hydrogel chamber.

Here, the hydrogel structures can be polymerized by using a fluorescent microscope and limiting the illuminated area by the aperture. Thereby, in-situ polymerization of structures on the microscope is possible.

For the formation of the gel chambers, the swelling of hydrogel micro-structures is used again. By spacing pillars close to each other, they can close a passage when they swell. This process could be reversed when changing the ionic strength of the media and thus, release components entrapped in the chambers.

Another possibility that would permit a release of spheroids or cells from such chambers or in general from a hydrogel, is the incorporation of light induced cleavage sites in the gel backbone [130, 219]. Photodegradable gels enable the extraction of cells from hydrogels to perform e.g. gene analysis to complement migration experiments.
Taken together, the photo-lithographic micro-structuring of small hydrogel patterns inside channel slides presented in this work is a versatile method to form complex 3D matrices for cell migration studies. The performed experiments help to understand the importance of matrix mechanics on cell migration guidance. They further affirm the necessity of taking the step from 2D to 3D experiments in cell research, despite the higher complexity that goes along with it.

A. Methods and Experimental Details

A.1. Gel polymerization and surface modification

A.1.1. Synthesis of the photo-initiator lithium phenyl-2,4,6-trimethylbenzoylphosphinate (LAP)

The photo-initiator used to start the radical polymerization reaction of the hydrogel was synthesized as previously described by Majima et al. (see figure A.1) [220]. 1.07g of 2,4,6-trimethylbenzoyl chloride (Sigma-Aldrich) was added drop-wise to a continuously stirred solution of 1g of dimethyl phenylphosphonite (Sigma-Aldrich) at room temperature and under argon atmosphere. After stirring for 18h, a solution of lithium bromide (Sigma-Aldrich) in 33.6ml of 2-butanone (Sigma-Aldrich) was added and the whole mixture was heated to 50°C. A precipitate formed whereupon the mixture was cooled to room temperature and stirred for an additional 4h. Afterwards, it was filtered and the precipitate was washed three times with 2-butanone. The solid was transferred to a round-bottom flask and dried in a desiccator over night. Phenyl-2,4,6-trimethylbenzoylphosphinate (LAP) was obtained as white solid in almost quantitative yield (84%). An absorption spectra from 300–500nm was recorded to confirm the successful synthesis of LAP.

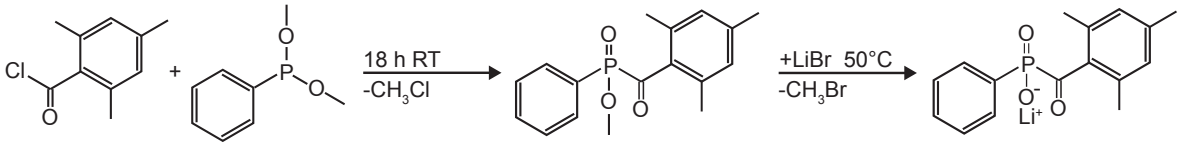

Figure A.1.: Synthesis of the photo-initiator LAP.

A.1.2. Covalent surface functionalization

To covalently bind hydrogels to a surface, suitable functional groups have to be present. Surface associated PEG molecules impede cell adhesion and render a material cell repellent. Thus, a photo-induced radical immobilization procedure (see figure A.2) previously described by Larsen et al. was used in this thesis to bind norbornene and thiol functionalized PEG molecules on the polymere coverslip of ibidi slides (µ-Slide Chemotaxis and µ-Slide Angiogenesis, ibidi) [221].

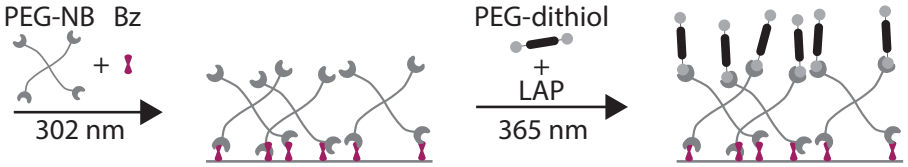

Figure A.2.: Schematic overview of the surface functionalization procedure. PEG-NB molecules are immobilized on the coverslip through a radical reaction initiated by 302nm light. In a second step, PEG-dithiol is bound to the PEG-NB to decorate the surface with thiol groups.

A solution of 5mM 20kDa 4-armed PEG-norbornene (PEG-NB, JenKem Technology USA) and 4mM 4-benzoyl benzylamine hydrochloride (Bz, Fluorochem) in PBS was injected in the channel of the µ-Slide Chemotaxis or pipetted in the well of the µ-Slide Angiogenesis and illuminated with a 302nm lamp (VWR) for 30min through the polymer coverslip. After washing three times with PBS, the surface was covered with a solution of 20mM 1kDa linear dithiol-PEG (PEG-dithiol, Sigma-Aldrich) and 10mM LAP in PBS and illuminated through the bottom of the slide with 365nm light (collimated LED at 10mW cm^2, Rapp OptoElectronic) for 30s. After final washing steps with PBS the functionalized surfaces were kept in PBS until further use.

A.1.3. Photo-lithographic structuring of hydrogels in channel slides

To form hydrogel structures inside channels, different slides from ibidi were used. For the characterization of the gels in chapter 4, the µ-Slide VI 0.4 uncoated and the µ-Slide VI 0.1 uncoated, with 400 and 100µm high channels, respectively, were used. The µ-Slide VI 0.4 uncoated was also used in chapter 5. For the formation of sponge clamps in chapter 6, the surface of the µ-Slide Chemotaxis was functionalized as described in section A.1.2 prior to gel polymerization.

If not stated otherwise, 2–3mM PEG-NB, an off-stoichiometric amount of dithiol-containing cross-linking molecule, 1mM CRGDS-peptide (Iris Biotech) and 3mM of the photo-initiator LAP are mixed in PBS and injected in the channel slide. The slide is directly put on a chromium mask containing the desired structures and illuminated through the bottom with collimated 365nm light for 20s, if not stated otherwise. The regions illuminated by the light polymerize and form small hydrogel structures in the channel. After washing the channels with PBS or cell culture media the slides are placed in an incubator at 37°C for at least 2h until the structures are completely swollen.

The composition of the gel was varied within this work. As cross-linker either a small peptide sequence that can be degraded by matrix metalloproteinases (MMPs) (KCG-PQGIWGQCK, Iris Biotech) (used in chapter 5) or the non-cleavable 1kDa PEG-dithiol (chapter 6) was used. Depending on the cross-linker utilized, the formed gels

are degradable by cells expressing MMPs or they are non-degradable and thus, non-migratable. To accurately describe the composition of the gels, a cross-linker ratio r_c is defined according to equation 3.1.
Cells or other small particles can easily be embedded in the gel by adding them into the pre-polymer solution before the solution is injected into the channel. To embed cells in the gel in chapter 5, a suspension of HT-1080 cells in PBS was mixed with the pre-polymer solution, reaching a final cell concentration of $6.7\text{x}10^5$cells/ml. To visualize the gel and detect deformations, small fluorescent beads (e.g. 200nm red-fluorescent beads (Invitrogen) or 1.1µm green fluorescent beads (Sigma-Aldrich)) were embedded in some gels.

A.1.4. Polymerization of hydrogel slabs for migration studies

To analyze cell migration in isotropically swollen hydrogels, gel slabs were formed and swollen while freely floating in cell culture medium. To polymerize the gels, a pre-polymer solution consisting of 2mM PEG-NB, 2.4mM cross-linker, 1mM CRGDS peptide, 3mM LAP and HT-1080 cells at a final concentration of $6.7\text{x}10^5$cells/ml in PBS was prepared. As cross-linker a mixture of cleavable peptide linker and non-cleavable PEG-dithiol linker at a ratio of 1–0.4 was used to change the overall degradability of the network.
Small amounts of pre-polymer solution (approximately 1µl) and air were alternately aspirated with a pipette and injected into a silicon tubing (Tygon) with an inner diameter of 1.6mm (see figure A.3). The tube was illuminated with 365nm light for 30s to polymerize the solution. The formed gels were pushed out of the tube by air pressure and were allowed to swell freely floating in cell culture medium for 2h under standard conditions (37°C, 5% CO_2, 100% humidity).
To enable long-term microscopic migration analysis, the hydrogel slabs were fixed to the bottom of a µ-Slide Angiogenesis. The slide surface was functionalized as described in section A.1.2. Then, 1µl of 0.5mM LAP in PBS was pipetted onto the functionalized surface and a swollen hydrogel slab was placed on top of it. After illuminating through the bottom of the slide with 365nm light for 5s, the gel was covalently bound to the surface and the well was filled with cell culture medium (see figure A.4).

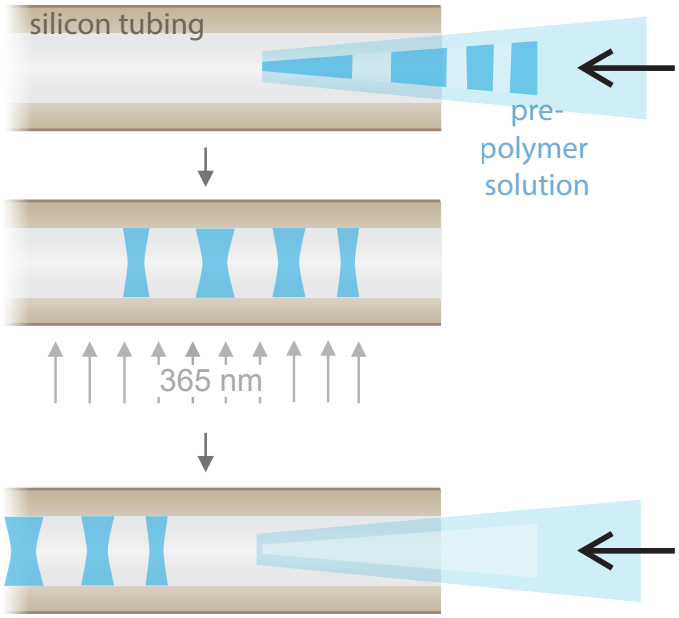

Figure A.3.: Schematic overview of the polymerization procedure of small hydrogel slabs. Pre-polymer solution and air is alternately aspirated in a pipette and injected into a silicon tubing. The tube is illuminated with 365nm light to polymerize the hydrogel slabs, which are afterwards pressed into PBS.

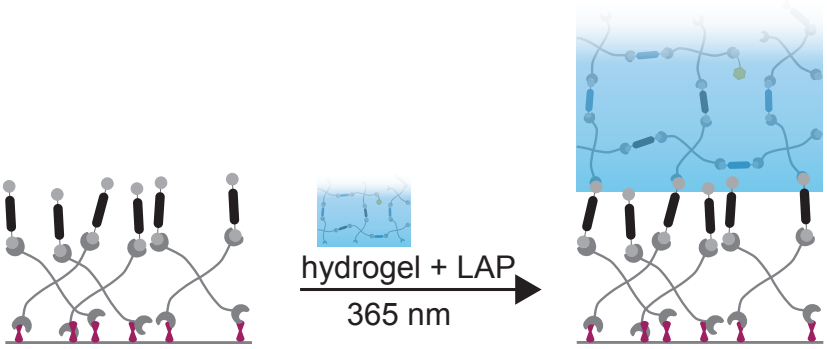

Figure A.4.: Schematic overview of the hydrogel immobilization on a functionalized surface. The polymerized and swollen hydrogel slab is immobilized on a surface functionalized according to chapter A.1.2 by LAP initiated thiol-ene reaction.

A.1.5. Polymerization of hydrogel slabs for stiffness measurements

For the macroscopic stiffness measurements described in detail in section A.4.4, big hydrogel slabs with a diameter of 2cm were casted in a custom made mold. The mold consists of a plastic syringe (20ml, VWR) where the top is cut off and the plunger is covered with a piece of balloon to avoid adhesion of the gel to the syringe. Pre-polymer solution of 2 or 3mM PEG-NB, an off-stoichiometric amount of the MMP cleavable peptide cross-linker (peptide: KCGPQGIWGQCK), 1mM CRGDS peptide and 3mM LAP in PBS was used. The solution was pipetted in the mold, illuminated with collimated light of 365nm for 30s and afterwards the formed big hydrogel slab was pressed into PBS and was allowed to swell overnight before stiffness measurements

were performed.

A.2. Microscopy

Microscopic images of the gels and cells were acquired on three different microscopes. For fluorescence images a Nikon Eclipse Ti (Nikon) inverted microscope equipped with a CFI Plan Fluor DL 10x or a 60x oil CFI Plan Apochromat objective (both Nikon), an Intensilight C-HG TIE (Nikon) and an Orca Flash 4.0 LT (Hamamatsu) camera was used. For phase-contrast images either the above mentioned Nikon microscope was used with a CFI Plan Fluor DL 4x objective, or an Olympus CKX41 (Olympus) with a UPlan FL N 4x objective (Olympus), or an EVOS fl (AMG) with a 4x objective. When cells were imaged in time-lapse recordings, the microscopes were equipped with a temperature-controlled heating system together with a gas incubation system (both from ibidi) to insure a humidified atmosphere with 5% CO_2 at 37°C.

A.3. Cell culture

A.3.1. Routine culture

Routine cell culture was performed according to the standard operating procedures implemented in the laboratory. The used cell lines and their detailed culture conditions are listed in table A.1. Cells were cultured in standard culture flasks (Sarstedt) in a humidified atmosphere at 37°C and 5% CO_2 until they reached a confluence of around 80%. Then the culture was washed with PBS, trypsinized at 37°C and after addition of cell culture medium, the cell suspension was centrifuged for 5min at 200 x g. The cell pellet was resuspended in fresh culture medium and seeded in a new flask for routine culture. Cells that were embedded in a hydrogel were resuspended in PBS instead of culture medium.

Table A.1.: Cell lines and their culture conditions used in this thesis.

cell line	supplier	cell culture medium	trypsination time
HT-1080	DSMZ	DMEM + 10% FBS	2min
HT-1080-LifeAct	ibidi	DMEM + 10%FBS + 0.75mg/ml G418	2min
MDA-MB-231	DSMZ	DMEM-F12 + 10% FBS	3min

A.3.2. Cell viability studies

Gel strips containing HT-1080 cells were polymerized as described in chapter A.1.3 and kept at standard culture conditions until live-dead staining was performed. For every

gel composition five channels were prepared to analyze the cell viability at five different days. 2h after the polymerization and every 24h the culture medium in the channels was replaced with new medium. Stainings were performed 3h after polymerization and on the four consecutive days using a mixture of 8µg/ml fluorescein diacetate (FDA) and 20µg/ml propidium iodide (PI) in PBS. Before incubating the gels for 5min with this solution in the dark, the channels were washed with PBS to reduce background signal. Afterwards the staining solution is washed out of the channels with PBS and the gels are immediately imaged on the Nikon Eclipse Ti microscope with the 60x objective. z-stacks of the gels with a spacing of 50 µm were acquired over the whole channel height. The image-processing software ImageJ was used to project the z-stack of each fluorescent channel onto one plane using the maximal intensity projection. The images are further auto-thresholded and then analyzed using the 'analyze particles' function from ImageJ to count the number of viable and dead cell. The viability v is calculated according to equation 4.2 by comparing the number of viable cells to the overall cell number.

A.4. Characterization of the hydrogel structures

A.4.1. Particle image velocimetry analysis

To analyze the swelling behavior of small hydrogel strips under confinement, 1.1µm beads were supplemented in the pre-polymer solution. The gel was polymerized as described in section A.1.3 inside a µ-Slide VI 0.4 and, before flushing the unpolymerized solution out, the slide was mounted on a microscope equipped with a 10x objective. Directly after washing the channels with PBS, image acquisition was started using 2min intervals for 3h. The MatLab (version 9.2.0.556344 (R2017a), The MathWorks, Inc.) toolbox MatPIV (version 1.6.1) was afterwards used with a slightly customized script to perform particle image velocimetry (PIV) analysis on the acquired image stack. Changes in the script include a smallest interrogation size window of 64x64 pixels with a 50% overlap. The filtering process used in the analysis was changed to include a signal-to-noise-ratio filter, a global histogram operator as well as a local filter. These filters deleted outliers and replaced them with not a number(NaN) values. Afterwards, all NaN values with at least five remaining surrounding neighbors were replaced by a linear interpolation from the neighboring vectors. The minimal limit of five neighbors ensures that the vector field is localized within the gel strip area, without propagating beyond the strip edges.

A.4.2. Measurement of the swelling ratio and swelling strain

In this work, the swelling of hydrogel strips inside channel systems is described by the swelling ratio r_{sw}, calculated according to equation 4.1. The gel strips were swollen for at least 2h and then imaged with a 4x objective on the Olympus or EVOS microscope. The strip width in the longitudinal middle section of the strip was measured and used to calculate the swelling ratio by comparing it to the initial strip width.
Considering the PIV analysis of the swelling process, where swelling in the longitudinal middle section of the strips was only detected in the direction parallel to the strip width, the strain γ_{s} induced in the confined gel strip was calculated by comparing the width before and after swelling according to equation 5.1 in chapter 5.

A.4.3. Estimation of the gel compression in the sponge clamp

To calculate how much the gel is compressed in the sponge clamp, the initial strip distance D, which at the same time is the compressed strip width, is compared to the equilibrium strip width, W_{end}, according to equation 6.2. W_{end} was measured in a separate experiment, where hydrogel strips were polymerized in the functionalized µ-Slide Chemotaxis as described in section A.1.3 with a high initial distance D. Thus, the strips swelled without touching neighboring strips. The gels were imaged on the EVOS microscope with a 4x objective and the strip width was measured in the longitudinal middle section of the strip.

A.4.4. Shear rheometry

For bulk measurements of the gel stiffness, big hydrogel slabs were polymerized as described in section A.1.5. The samples were measured on a rheometer MCR100 (Anton Paar) on a plate-plate set-up with a diameter of 2cm. For every gel composition tested, one frequency sweep from 0.1–50s^{-1} with an amplitude of 2% was performed to ensure a measurement in the linear regime. For all gels, a frequency of 1.6Hz was used in the following amplitude sweep. The measurments were performed in a range from 0.1–50% an yielded a linear elastic respond for a deformation from 2.8–9%. For each gel composition the mean of all measurements in this regime was calculated to obtain a macroscopic storage modulus for each gel composition.

A.5. Cell migration analyses

A.5.1. Tracking of single cells and analysis of the migration anisotropy

In chapter 5 cell migration of embedded HT-1080 cells was analyzed using phase-contrast time-lapse imaging with 10min intervals for 24h starting 3h after cell encapsulation. They were recorded on the Olympus or Nikon microscope with a 4x objective. The plug-in 'Manual Tracking' in ImageJ was used to manually track the center of 25 randomly selected cells per experiment and condition. For each condition 3–5 biological replicates are performed with 2–3 positions each. Further analyses of the migration tracks were performed in MatLab. Only cells which migrated a total distance bigger than 40µm were considered migrating and were included in the analyses. In the migration experiments in isotropically swollen hydrogel slabs described in chapter 5.4, a static structure in the gel is tracked for every position and used to correct the cell migration tracks due to a small overall movement of the big gel slab.

To analyze the main migration direction of the embedded cells, the recorded cell position at each time point was used to calculate the total distance traveled by the cell parallel and perpendicular to the strain direction separately (see equation 5.5 and 5.6 in chapter 5.5). Comparing their deviation to the total distance traveled by the cell yields the anisotropic migration index (AMI) according to equation 5.7.

A.5.2. Sponge clamp experiments and cell invasion analysis

To analyze the invasion of cells into hydrogel-hydrogel interfaces as discussed in chapter 6, parallel hydrogel strips with a small initial spacing of 130–150µm are polymerized in µ-Slides Chemotaxis as described in chapter A.1.3. The structures were allowed to swell in cell culture medium at 37°C overnight before cells were introduced into the system. A cell suspension of 30 000 cells/ml in cell culture medium with a reduced FBS concentration of 1% was injected into one reservoir of the slide. Then the slide was placed upright in an incubator with this reservoir facing up so all cells would fall onto the sponge clamps. After 1h the slide was mounted on the Olympus microscope with a 4x objective and time-lapse acquisition was started with 20min intervals for up to 60h. With the ImageJ plug-in 'Manual Tracking' the first cell invading a hydrogel-hydrogel interface was tracked manually. Additionally, the starting point of the sponge clamp was tracked to calculate the cell invasion depth for every track. 7–11 clamps were analyzed in one channel, with two channels per biological replicate and 3–4 replicates per condition.

A.5.3. Calculation of the mean square displacement and velocity autocorrelation function

To calibrate the theoretical model in chapter 5.4 the mean square displacement (MSD) and the velocity auto-correlation function (VACF) were calculated for cells migrating in isotropically swollen gels with different degradability and in simulated cells on unstrained lattices. The VACF is given by

$$VACF(t) = \frac{1}{T-t+1} \sum_{\tau=0}^{T-t} [\vec{v}(\tau+t) \cdot \vec{v}(\tau)], \tag{A.1}$$

where $\vec{v}(\tau)$ and $\vec{v}(\tau+t)$ are the velocity vectors of a cell at time point τ and $\tau + t$, respectively and T is the number of time points recorded in the experiment or simulation. The MSD is calculated according to

$$MSD(t) = \frac{1}{T-t+1} \sum_{\tau=0}^{T-t} [\vec{r}(\tau+t) - \vec{r}(\tau)]^2 \tag{A.2}$$

where $\vec{r}(\tau)$ and $\vec{r}(\tau+t)$ are the position vectors of a cell at time point τ and $\tau + t$, respectively.

A.6. Implementation of the theoretical cell migration model

The model described in the following chapter was implemented by Hugo LeRoy and David B. Brückner in the group of Prof. Chase Broedersz (LMU Munich) within the framework of a collaboration. The movement of a bodyless point on a 2D lattice network is modeled to simulate the proteolytic, durotactic cell migration in a 3D network. The migration matrix consists of a coarse-grained model of a triangular lattice network. Grid nodes are connected by linear springs, which have an elastic constant of k and a rest length l_0. To introduce an intrinsic disorder, every node is only connected to 4.8 bonds on average.

In the simulation, migration is modeled by four basic steps (see figure 5.7). First, the cell deforms the network by pulling on the second nearest neighbor nodes. Then, the stiffness magnitudes of the nodes, which depend on the restoring force of the network according to equation 5.3, are calculated for every neighbor node. As third step, the bodyless cell moves to the neighboring node with the highest stiffness magnitude and thereafter randomly deletes an average of one bond per simulation cycle to a nearest neighbor node. If not stated otherwise, 100 of such computational cycles are performed for one cell simulation.

For migration simulations in strained networks, the lattice is rotated by 15° to prevent the alignment of special network axis with the strain direction. The networks are uniaxially strained before migration is simulated.
When calculating the anisotropic migration index for a modeled cell, two corrections are necessary to be able to compare it to the AMI of the experiments. First, the distance traveled by the cell parallel to the external strain is corrected by the strain magnitude according to equation 5.8 to compensate for the increased node to node distance. Secondly, the calculated AMI is normalized to the maximal AMI that can be reached in the model (0.577 for a 15°C rotation of the lattice network, see equation 5.9).
In an extension of the model, a time-averaged mechanosensing is implemented. There, the stiffness measurements of the last N_{av} cycles are averaged and the cell moves in the direction of the highest average stiffness. For calculations of the AMI in this system, only migration steps after the first N_{av} cycles are considered.

List of Publications

P1 Miriam Dietrich, Hugo LeRoy, David B. Brückner, Hanna Engelke, Roman Zantl, Joachim O. Rädler and Chase P. Broedersz . **Guiding 3D cell migration in deformed synthetic hydrogel microstructures.** *Soft Matter*, 2018,14, 2816–2826.

P2 Roman Zantl, Miriam Dietrich (2016) **Fluidkanalsystem zur Untersuchung von Zellen.** *Patent number: EP 3 020 480 A1.*

List of Abbreviations

2D	two-dimensional
3D	three-dimensional
AMI	anisotropic migration index
Bz	4-benzoyl benzylamine hydrochloride
DMEM	Dulbecco's Modified Eagle Medium
DMEM/F12	Dulbecco's Modified Eagle Medium/Nutrient Mixture F-12
DNA	deoxyribonucleic acid
ECM	extracellular matrix
FBS	fetal bovine serum
FDA	fluorescein diacetate
GAG	glycosamyloglycan
I2959	1-[4-(2- hydroxyethoxy)-phenyl]-2-hydroxy-2-methyl-1-propanone
LAP	lithium phenyl- 2,4,6-trimethylbenzoylphosphinate
LED	light-emitting diode
MMP	matrix-metalloproteinase
MSD	mean square displacement
PA	polyacrylamide
PBS	phosphate buffered saline
PDMS	polydimethylsiloxane
PEG	polyethylene glycol
PEG-dithiol	linear 1kDa PEG with one thiol group at each end
PEG-NB	20kDa 4-arm PEG-norbornene
PI	propidium iodide
PIV	particle image velocimetry
UV	ultraviolet
VACF	velocity autocorrelation function

Bibliography

[1] Hanahan, D.; Weinberg, R.A. (2011). Hallmarks of cancer: The next generation. *Cell*, 144(5), 646–674.

[2] Clark, A.G.; Vignjevic, D.M. (2015). Modes of cancer cell invasion and the role of the microenvironment. *Current Opinion in Cell Biology*, 36, 13–22.

[3] Yilmaz, M.; Christofori, G. (2009). EMT, the cytoskeleton, and cancer cell invasion. *Cancer and Metastasis Reviews*, 28(1-2), 15–33.

[4] Hockemeyer, K.; Janetopoulos, C.; Terekhov, A.; Hofmeister, W.; Vilgelm, A.; Costa, L.; Wikswo, J.P.; Richmond, A. (2014). Engineered three-dimensional microfluidic device for interrogating cell-cell interactions in the tumor microenvironment. *Biomicrofluidics*, 8(4), 044105.

[5] He, K.; Xu, T.; Goldkorn, A. (2011). Cancer cells cyclically lose and regain drug-resistant highly tumorigenic features characteristic of a cancer stem-like phenotype. *Molecular Cancer Therapeutics*, 10(6), 938–948.

[6] Egeblad, M.; Rasch, M.G.; Weaver, V.M. (2010). Dynamic interplay between the collagen scaffold and tumor evolution. *Current Opinion in Cell Biology*, 22(5), 697–706.

[7] Goetzl, E.J.; Bando, M.J.; Leppert, D. (1996). Matrix metalloproteinases in immunity. *J Immunol*, 156, 1–4.

[8] Nourshargh, S.; Alon, R. (2014). Leukocyte migration into inflamed tissues. *Immunity*, 41(5), 694–707.

[9] O'Connor, T.P.; Duerr, J.S.; Bentley, D. (1990). Pioneer growth cone steering decisions mediated by single filopodial contacts in situ. *The Journal of Neuroscience*, 10(12), 3935–3946.

[10] Cooper, J.A. (2013). Mechanisms of cell migration in the nervous system. *The Journal of Cell Biology*, 202(5), 725–734.

[11] Harris, H. (1954). Role of chemotaxis in inflammation. *Physiological Reviews*, 34(3), 529–562.

[12] Roca-Cusachs, P.; Sunyer, R.; Trepat, X. (2013). Mechanical guidance of cell migration: Lessons from chemotaxis. *Current Opinion in Cell Biology*, 25(5), 543–549.

[13] Weiss, P. (1934). in vitro experiments on the factors determining the course of the outgrowing nerve fiber. *The journal of experimental zoology*, 68(3), 393–448.

[14] Maiuri, P.; Terriac, E.; Paul-Gilloteaux, P.; Vignaud, T.; McNally, K.; Onuffer, J.; Thorn, K.; Nguyen, P.A.; Georgoulia, N.; Soong, D.; Jayo, A.; Beil, N.; Beneke, J.; Hong Lim, J.C.; Pei-Ying Sim, C.; Chu, Y.S.; Jiménez-Dalmaroni, A.; Joanny, J.F.; Thiery, J.P.; Erfle, H.; Parsons, M.; Mitchison, T.J.; Lim, W.A.; Lennon-Duménil, A.M.; Piel, M.; Théry, M. (2012). The first World Cell Race. *Current Biology*, 22(17), R673–R675.

[15] Schreiber, C.; Segerer, F.J.; Wagner, E.; Roidl, A.; Rädler, J.O. (2016). Ring-Shaped microlanes and chemical barriers as a platform for probing single-cell migration. *Scientific Reports*, 6(February), 1–9.

[16] Segerer, F.J.; Thüroff, F.; Piera Alberola, A.; Frey, E.; Rädler, J.O. (2015). Emergence and persistence of collective cell migration on small circular micropatterns. *Physical Review Letters*, 114(22), 1–5.

[17] Kushiro, K.; Asthagiri, A.R. (2012). Modular design of micropattern geometry achieves combinatorial enhancements in cell motility. *Langmuir*, 28(9), 4357–4362.

[18] Vu, L.T.; Jain, G.; Veres, B.D.; Rajagopalan, P. (2015). Cell migration on planar and three-dimensional matrices: A hydrogel-based perspective. *Tissue Engineering Part B: Reviews*, 21(1), 67–74.

[19] Lo, C.M.; Wang, H.B.; Dembo, M.; Wang, Y.L. (2000). Cell movement is guided by the rigidity of the substrate. *Biophysical Journal*, 79(1), 144–152.

[20] Grover, C.N.; Gwynne, J.H.; Pugh, N.; Hamaia, S.; Farndale, R.W.; Best, S.M.; Cameron, R.E. (2012). Crosslinking and composition influence the surface properties, mechanical stiffness and cell reactivity of collagen-based films. *Acta Biomaterialia*, 8(8), 3080–90.

[21] Wen, Q.; Janmey, P.A. (2013). Effects of non-linearity on cell-ECM interactions. *Experimental Cell Research*, 319(16), 2481–2489.

[22] Sung, K.E.; Su, G.; Pehlke, C.; Trier, S.M.; Eliceiri, K.W.; Keely, P.J.; Friedl, A.; Beebe, D.J. (2009). Control of 3-dimensional collagen matrix polymerization

for reproducible human mammary fibroblast cell culture in microfluidic devices. *Biomaterials*, 30(27), 4833–41.

[23] Vukicevic, S.; Kleinman, H.K.; Luyten, F.P.; Roberts, A.B.; Roche, N.S.; Reddi, A.H. (1992). Identification of multiple active growth factors in basement membrane Matrigel suggests caution in interpretation of cellular activity related to extracellular matrix components. *Experimental Cell Research*, 202, 1–8.

[24] Tibbitt, M.W.; Anseth, K.S. (2009). Hydrogels as extracellular matrix mimics for 3D cell culture. *Biotechnology and Bioengineering*, 103(4), 655–663.

[25] Lutolf, M.P.; Hubbell, J.A. (2005). Synthetic biomaterials as instructive extracellular microenvironments for morphogenesis in tissue engineering. *Nature Biotechnology*, 23(1), 47–55.

[26] Lampe, K.J.; Antaris, A.L.; Heilshorn, S.C. (2013). Design of three-dimensional engineered protein hydrogels for tailored control of neurite growth. *Acta Biomaterialia*, 9(3), 5590–5599.

[27] Ahmed, M.; Ramos, T.; Wieringa, P.; Blitterswijk, C.V.; Boer, J.D.; Moroni, L. (2018). Geometric constraints of endothelial cell migration on electrospun fibres. *Scientific Reports*, 8(1), 1–10.

[28] Sill, T.J.; von Recum, H.A. (2008). Electrospinning: Applications in drug delivery and tissue engineering. *Biomaterials*, 29(13), 1989–2006.

[29] Raeber, G.P.; Lutolf, M.P.; Hubbell, J.a. (2005). Molecularly engineered PEG hydrogels: a novel model system for proteolytically mediated cell migration. *Biophysical Journal*, 89(2), 1374–88.

[30] Singh, S.P.; Schwartz, M.P.; Lee, J.Y.; Fairbanks, B.D.; Anseth, K.S. (2014). A peptide functionalized poly(ethylene glycol) (PEG) hydrogel for investigating the influence of biochemical and biophysical matrix properties on tumor cell migration. *Biomaterials Science*, 2, 1024–1034.

[31] Hansen, T.D.; Koepsel, J.T.; Le, N.N.; Nguyen, E.H.; Zorn, S.; Parlato, M.; Loveland, S.G.; Schwartz, M.P.; Murphy, W.L. (2014). Biomaterial arrays with defined adhesion ligand densities and matrix stiffness identify distinct phenotypes for tumorigenic and non-tumorigenic human mesenchymal cell types. *Biomaterials Science*, 2(5), 745–756.

[32] Zhu, J. (2010). Bioactive modification of poly(ethylene glycol) hydrogels for tissue engineering. *Biomaterials*, 31(17), 4639–56.

[33] Cruise, G.M.; Scharp, D.S.; Hubbell, J.a. (1998). Characterization of permeability and network structure of interfacially photopolymerized poly(ethylene glycol) diacrylate hydrogels. *Biomaterials*, 19(14), 1287–94.

[34] Stringer, J.L.; Peppas, N.A. (1996). Diffusion of small molecular weight drugs in radiation-crosslinked poly (ethylene oxide) hydrogels. *Journal of Controlled Release*, 42, 195–202.

[35] Schwartz, M.P.; Fairbanks, B.D.; Rogers, R.E.; Rangarajan, R.; Zaman, M.H.; Anseth, K.S. (2010). A synthetic strategy for mimicking the extracellular matrix provides new insight about tumor cell migration. *Integr. Biol.*, 2(1), 32–40.

[36] Lutolf, M.P.; Hubbell, J.a. (2003). Synthesis and physicochemical characterization of end-linked poly (ethylene glycol)-co-peptide hydrogels formed by Michael-type addition. *Biomacromolecules*, 4, 713–722.

[37] Culver, J.C.; Hoffmann, J.C.; Poché, R.A.; Slater, J.H.; West, J.L.; Dickinson, M.E. (2012). Three-dimensional biomimetic patterning in hydrogels to guide cellular organization. *Advanced Materials*, 24(17), 2344–2348.

[38] Nemir, S.; Hayenga, H.N.; West, J.L. (2010). PEGDA hydrogels with patterned elasticity: Novel tools for the study of cell response to substrate rigidity. *Biotechnology and Bioengineering*, 105(3), 636–644.

[39] Hatten, M.E. (1993). The role of migration in central nervous system neuronal development. *Current Opinion Neurobiology*, 3(1), 38–44.

[40] Ray, S.J.; Franki, S.N.; Pierce, R.H.; Dimitrova, S.; Koteliansky, V.; Sprague, A.G.; Doherty, P.C.; Fougerolles, A.R.D.; Topham, D.J.; York, N.; De Fougerolles, A.R.; Topham, D.J. (2004). The collagen binding $\alpha 1\beta 1$ integrin VLA-1 regulates CD8 T cell-mediated immune protection against heterologous influenza infection. *Immunity*, 20(2), 167–179.

[41] Egeblad, M.; Werb, Z. (2002). New functions for the matrix metalloproteinases in cancer progression. *Nature Reviews Cancer*, 2(March), 161–174.

[42] Fletcher, D.A.; Mullins, R.D. (2010). Cell mechanics and the cytoskeleton. *Nature*, 463(7280), 485–492.

[43] Lauffenburger, D.A.; Horwitz, A.F. (1996). Cell migration: Review a physically integrated molecular process. *Cell*, 84, 359–369.

[44] Pollard, T.D. (2003). The cytoskeleton, cellular motility and the reductionist agenda. *Nature*, 422(6933), 741–745.

[45] Watanabe, T.; Noritake, J.; Kaibuchi, K. (2005). Regulation of microtubules in cell migration. *Trends in Cell Biology*, 15(2), 76–83.

[46] Goode, B.L.; Drubin, D.G.; Barnes, G. (2000). Functional cooperation between the microtubule and actin cytoskeletons. *Current Opinion in Cell Biology*, 12(1), 63–71.

[47] Wiche, G. (1998). Role of plectin in cytoskeleton organization and dynamics. *Journal of Cell Science*, 111, 2477–2486.

[48] Kreplak, L.; Doucet, J.; Dumas, P.; Briki, F. (2004). New aspects of the α-helix to β-sheet transition in stretched hard α-keratin fibers. *Biophysical Journal*, 87(1), 640–647.

[49] Schoumacher, M.; Goldman, R.D.; Louvard, D.; Vignjevic, D.M. (2010). Actin, microtubules, and vimentin intermediate filaments cooperate for elongation of invadopodia. *Journal of Cell Biology*, 189(3), 541–556.

[50] Lammerding, J.; Fong, L.G.; Ji, J.Y.; Reue, K.; Stewart, C.L.; Young, S.G.; Lee, R.T. (2006). Lamins A and C but not lamin B1 regulate nuclear mechanics. *Journal of Biological Chemistry*, 281(35), 25768–25780.

[51] Irianto, J.; Pfeifer, C.R.; Bennett, R.R.; Xia, Y.; Ivanovska, I.L.; Liu, A.J.; Greenberg, R.A.; Discher, D.E. (2016). Nuclear constriction segregates mobile nuclear proteins away from chromatin. *Molecular Biology of the Cell*, 27(25), 4011–4020.

[52] Lautscham, L.A.; Kämmerer, C.; Lange, J.R.; Kolb, T.; Mark, C.; Schilling, A.; Strissel, P.L.; Strick, R.; Gluth, C.; Rowat, A.C.; Metzner, C.; Fabry, B. (2015). Migration in confined 3D environments is determined by a combination of adhesiveness, nuclear volume,contractility, and cell stiffness. *Biophysical Journal*, 109(5), 900–913.

[53] Denais, C.M.; Gilbert, R.M.; Isermann, P.; Mcgregor, A.L.; Lindert, M.; Weigelin, B.; Davidson, P.M.; Friedl, P.; Lammerding, J. (2016). Nuclear envelope rupture and repair during cancer cell migration. *Science*, 352(6283), 353–358.

[54] Condeelis, J. (1993). Life at the leading edge: The formation of cell protrusions. *Annual Review of Cell Biology*, 9(1), 411–444.

[55] Zaidel-Bar, R. (2003). Early molecular events in the assembly of matrix adhesions at the leading edge of migrating cells. *Journal of Cell Science*, 116(22), 4605–4613.

[56] Insall, R.H.; Machesky, L.M. (2009). Actin dynamics at theleading edge: from simple machinery to complex networks. *Developmental Cell*, 17(3), 310–322.

[57] Bresnick, a.R. (1999). Molecular mechanisms of nonmuscle myosin II regulation. *J Cell Biol*, 11, 26–33.

[58] Vicente-Manzanares, M.; Ma, X.; Adelstein, R.S.; Horwitz, A.R. (2009). Non-muscle myosin II takes centre stage in cell adhesion and migration. *Nature Reviews Molecular Cell Biology*, 10(11), 778–790.

[59] Burridge, K. (1988). Focal adhesions: Transmembrane junctions between the extracellular matrix and the cytoskeleton. *Annual Review of Cell and Developmental Biology*, 4(1), 487–525.

[60] Kanchanawong, P.; Shtengel, G.; Pasapera, A.M.; Ramko, E.B.; Davidson, W.; Hess, H.F.; Waterman, C.M. (2010). Nanoscale architecture of integrin-based cell adhesions. *Nature*, 468(7323), 580–584.

[61] Levy, J.R.; Holzbaur, E.L.F.; Parsons, J.T.; Horwitz, A.R.; Schwartz, M.a.; Larson, D.R.; Singer, R.H.; Zenklusen, D.; Campellone, K.G.; Welch, M.D.; Schneider-poetsch, T.; Ju, J.; Eyler, D.E.; Dang, Y.; Bhat, S.; Merrick, W.C.; Green, R.; Shen, B.; Liu, J.O.; Schnitzer, J.; Storm, N.i. (2010). Cell adhesion: integrating cytoskeletal dynamics and cellular tension. *Nat Rev Mol Cell Biol.*, 11(9), 633–643.

[62] Hynes, R.O. (2002). Integrins : Bidirectional , allosteric signaling machines. *Cell*, 110, 673–687.

[63] Huttenlocher, A.; Horwitz, A.R. (2011). Integrins in cell migration. *Cold Spring Harbor Perspectives in Biology.*

[64] Schwartz, M.A. (2010). Integrins and extracellular matrix in mechanotransduction. *Cold Spring Harbor Perspectives in Biology.*

[65] Ross, T.D.; Coon, B.G.; Yun, S.; Baeyens, N.; Tanaka, K.; Ouyang, M.; Schwartz, M.A. (2013). Integrins in mechanotransduction. *Curr Opin Cell Biol*, 25(5), 613–618.

[66] Frantz, C.; Stewart, K.M.; Weaver, V.M. (2010). The extracellular matrix at a glance. *Journal of Cell Science*, 123(Pt 24), 4195–200.

[67] Alexandrova, A.Y. (2008). Evolution of cell interactions with extracellular matrix during carcinogenesis. *Biochemistry (Moscow)*, 73(7), 733–41.

[68] Bonnans, C.; Chou, J.; Werb, Z. (2014). Remodelling the extracellular matrix in development and disease. *Nature Reviews Molecular Cell Biology*, 15(12), 786–801.

[69] Kular, J.K.; Basu, S.; Sharma, R.I. (2014). The extracellular matrix: Structure, composition, age-related differences, tools for analysis and applications for tissue engineering. *Journal of Tissue Engineering*, 5, 1–17.

[70] Wolf, K.; Alexander, S.; Schacht, V.; Coussens, L.M.; von Andrian, U.; van Rheenen, J.; Deryugina, E.; Friedl, P. (2009). Collagen-based cell migration in vitro and in vivo. *Seminars in Cell & Developmental Biology*, 20(8), 931–941.

[71] Sabeh, F.; Ota, I.; Holmbeck, K.; Birkedal-hansen, H.; Soloway, P.; Balbin, M.; Lopez-otin, C.; Shapiro, S.; Inada, M.; Krane, S.; Allen, E.; Chung, D.; Weiss, S.J. (2004). Tumor cell traffic through the extracellular matrix is controlled by the membrane-anchored collagenase MT1-MMP. *Journal Cell Biology*, 167(4), 769–781.

[72] Ilina, O.; Bakker, G.J.; Vasaturo, A.; Hoffman, R.M.; Friedl, P. (2011). Two-photon laser-generated microtracks in 3D collagen lattices. *Physical Biology*, 8, 1–8.

[73] Oxlund, H.; Andreassen, T.T. (1980). The roles of hyaluronic acid, collagen and elastin in the mechanical properties of connective tissues. *J. Anat*, 131(4), 611–620.

[74] Muiznieks, L.D.; Keeley, F.W. (2013). Molecular assembly and mechanical properties of the extracellular matrix: A fibrous protein perspective. *Biochimica et Biophysica Acta*, 1832(7), 866–875.

[75] Smith, M.L.; Gourdon, D.; Little, W.C.; Kubow, K.E.; Eguiluz, R.A.; Luna-Morris, S.; Vogel, V. (2007). Force-induced unfolding of fibronectin in the extracellular matrix of living cells. *PLoS Biology*, 5(10), 2243–2254.

[76] Klotzsch, E.; Smith, M.L.; Kubow, K.E.; Muntwyler, S.; Little, W.C.; Beyeler, F.; Gourdon, D.; Nelson, B.J.; Vogel, V. (2009). Fibronectin forms the most extensible biological fibers displaying switchable force-exposed cryptic binding sites. *Proceedings of the National Academy of Sciences*, 106(43), 18267–18272.

[77] Iozzo, R.V.; Murdoch, A.D. (1996). Proteoglycans of the extracellular environment: clues from the gene and protein side offer novel perspectives in molecular diversity and function. *The FASEB Journal*, 10(5), 598–614.

[78] Järveläinen, H.; Saino, A.; Koulu, M.; Wight, T.N.; Penttinen, R. (2009). Extracellular matrix molecules: potential targets in pharmacotherapy. *Pharmacol Rev.*, 61(2), 198–223.

[79] Hildebrand, A.; Romarís, M.; Rasmussen, L.M.; Heinegård, D.; Twardzik, D.R.; Border, W.A.; Ruoslahti, E. (1994). Interaction of the small interstitial proteoglycans biglycan, decorin and fibromodulin with transforming growth factor beta. *The Biochemical Journal*, 534(Pt 2), 527–34.

[80] Taipale, J.; Keski-Oja, J. (1997). Growth factors in the extracellular matrix. *The FASEB Journal*, 11, 51–59.

[81] Friedl, P.; Alexander, S. (2011). Cancer invasion and the microenvironment: Plasticity and reciprocity. *Cell*, 147(5), 992–1009.

[82] Gritsenko, P.G.; Ilina, O.; Friedl, P. (2012). Interstitial guidance of cancer invasion. *Journal of Pathology*, 226(2), 185–199.

[83] Wolf, K.; Friedl, P. (2009). Mapping proteolytic cancer cell-extracellular matrix interfaces. *Clin Exp Metastasis*, 26, 289–298.

[84] Yoshida, K. (2006). Dissection of amoeboid movement into two mechanically distinct modes. *Journal of Cell Science*, 119(18), 3833–3844.

[85] Wolf, K.; Mazo, I.; Leung, H.; Engelke, K.; Von Andrian, U.H.; Deryugina, E.I.; Strongin, A.Y.; Bröcker, E.B.; Friedl, P. (2003). Compensation mechanism in tumor cell migration: Mesenchymal-amoeboid transition after blocking of pericellular proteolysis. *Journal of Cell Biology*, 160(2), 267–277.

[86] Sanz-Moreno, V.; Marshall, C.J. (2010). The plasticity of cytoskeletal dynamics underlying neoplastic cell migration. *Current Opinion in Cell Biology*, 22(5), 690–696.

[87] Wolf, K.; Friedl, P. (2011). Extracellular matrix determinants of proteolytic and non-proteolytic cell migration. *Trends in cell biology*, 21(12), 736–44.

[88] Geum, D.T.; Kim, B.J.; Chang, A.E.; Hall, M.S.; Wu, M. (2016). Epidermal growth factor promotes a mesenchymal over an amoeboid motility of MDA-MB-231 cells embedded within a 3D collagen matrix. *European Physical Journal Plus*, 131(1), 1–10.

[89] Trepat, X.; Wasserman, M.R.; Angelini, T.E.; Millet, E.; Weitz, D.A.; Butler, J.P.; Fredberg, J.J. (2009). Physical forces during collective cell migration. *Nature Physics*, 5(6), 426–430.

[90] Yamaguchi, N.; Mizutani, T.; Kawabata, K.; Haga, H. (2015). Leader cells regulate collective cell migration via Rac activation in the downstream signaling of integrin β1 and PI3K. *Scientific Reports*, 5, 1–8.

[91] Hegerfeldt, Y.; Tusch, M.; Bröcker, E.B.; Friedl, P. (2002). Collective cell movement in primary melanoma explants. *Cancer Research*, 62(7), 2125–2130.

[92] Clark, P.; Connolly, P.; Curtis, A.S.G.; Dow, J.A.T.; Wilkinson, C.D.W. (1991). Cell guidance by ultrafine topography in vitro. *Journal of Cell Science*, 99(Pt 1), 73–77.

[93] Micholt, L.; Gärtner, A.; Prodanov, D.; Braeken, D.; Dotti, C.G.; Bartic, C. (2013). Substrate topography determines neuronal polarization and growth in vitro. *PLoS ONE*, 8(6), 1–14.

[94] Marmaras, A.; Lendenmann, T.; Civenni, G.; Franco, D.; Poulikakos, D.; Kurtcuoglu, V.; Ferrari, A. (2012). Topography-mediated apical guidance in epidermal wound healing. *Soft Matter*, 8(26), 6922.

[95] Le Berre, M.; Liu, Y.J.; Hu, J.; Maiuri, P.; Bénichou, O.; Voituriez, R.; Chen, Y.; Piel, M. (2013). Geometric friction directs cell migration. *Physical Review Letters*, 111(19), 1–5.

[96] Isenberg, B.C.; DiMilla, P.A.; Walker, M.; Kim, S.; Wong, J.Y. (2009). Vascular smooth muscle cell durotaxis depends on substrate stiffness gradient strength. *Biophysical Journal*, 97(5), 1313–1322.

[97] Raab, M.; Swift, J.; Dingal, P.C.P.; Shah, P.; Shin, J.W.; Discher, D.E. (2012). Crawling from soft to stiff matrix polarizes the cytoskeleton and phosphoregulates myosin-II heavy chain. *Journal of Cell Biology*, 199(4), 669–683.

[98] Aznavoorian, S.; Stracke, M.L.; Krutzsch, H.; Schiffmann, E.; Liotta, L.A. (1990). Signal transduction for chemotaxis and haptotaxis by matrix molecules in tumor cells. *The Journal of Cell Biology*, 110, 1427–1438.

[99] Sockanathan, S.; Sabharwal, P.; Rao, M.; Lee, C.; Park, S.; Weinmaster, G.; Boulter, J.; Gossler, A.; Berrie, C.P.; Corda, D.; Farquhar, M.G.; Lieberam, I.; Porter, J.A.; Jessell, T.M.; Coussens, L.M.; Liu, J.F.; An, X.M.; Liang, D.C. (2013). Interstitial dendritic cell guidance by haptotactic chemokine gradients. *Science*, 339, 328–333.

[100] Moreno-Arotzena, O.; Borau, C.; Movilla, N.; Vicente-Manzanares, M.; García-Aznar, J.M. (2015). Fibroblast migration in 3D is controlled by haptotaxis in

a non-muscle myosin II-dependent manner. *Annals of Biomedical Engineering*, 43(12), 3025–3039.

[101] Parent, C.a.; Devreotes, P.N. (1999). A cell's sense of direction. *Science*, 284(April), 765–770.

[102] Bagorda, A.; Parent, C.A. (2008). Eukaryotic chemotaxis at a glance. *Journal of Cell Science*, 121(16), 2621–2624.

[103] Van Haastert, P.J.M.; Devreotes, P.N. (2004). Chemotaxis: Signalling the way forward. *Nature Reviews Molecular Cell Biology*, 5(8), 626–634.

[104] Tessier-Lavigne, M.; Goodman, C.S. (1996). The molecular biology of axon guidance. *Science*, 274(5290), 1123–1133.

[105] Koser, D.E.; Thompson, A.J.; Foster, S.K.; Dwivedy, A.; Pillai, E.K.; Sheridan, G.K.; Svoboda, H.; Viana, M.; Costa, L.d.F.; Guck, J.; Holt, C.E.; Franze, K. (2016). Mechanosensing is critical for axon growth in the developing brain. *Nature Neuroscience*, 19, 1592–1598.

[106] Ridley, A.J.; Schwartz, M.a.; Burridge, K.; Firtel, R.a.; Ginsberg, M.H.; Borisy, G.; Parsons, J.T.; Horwitz, A.R. (2003). Cell migration: integrating signals from front to back. *Science (New York, N.Y.)*, 302(5651), 1704–9.

[107] Ribeiro, A.; Vargo, S.; Powell, E.M.; Leach, J.B. (2012). Substrate three-dimensionality induceselemental morphological transformation of sensory neurons on a physiologic timescale. *Tissue Engineering Part A*, 18(1-2), 93–102.

[108] Smalley, K.S.M.; Lioni, M.; Herlyn, M. (2006). Life isn'T flat: Taking cancer biology to the next dimension. *In Vitro Cellular & Developmental Biology - Animal*, 42(8), 242.

[109] Petrie, R.J.; Gavara, N.; Chadwick, R.S.; Yamada, K.M. (2012). Nonpolarized signaling reveals two distinct modes of 3D cell migration. *Journal of Cell Biology*, 197(3), 439–455.

[110] Elsdale, T.; Bard, J. (1972). Collagen substrata for studies on cell behavior. *The Journal of Cell Biology*, 54, 626–637.

[111] Ruberti, J.W.; Hallab, N.J. (2005). Strain-controlled enzymatic cleavage of collagen in loaded matrix. *Biochemical and Bophysical Research Communications*, 336, 483–489.

[112] Poincloux, R.; Collin, O.; Lizárraga, F.; Romao, M.; Debray, M.; Piel, M.; Chavrier, P. (2011). Contractility of the cell rear drives invasion of breast tumor cells in 3D Matrigel. *Proceedings of the National Academy of Sciences*, 108(5), 1943–1948.

[113] Benton, G.; Kleinman, H.K.; George, J.; Arnaoutova, I. (2011). Multiple uses of basement membrane-like matrix (BME/Matrigel) in vitro and in vivo with cancer cells. *International Journal of Cancer*, 128(8), 1751–1757.

[114] Hughes, C.S.; Postovit, L.M.; Lajoie, G.A. (2010). Matrigel: a complex protein mixture required for optimal growth of cell culture. *Proteomics*, 10(9), 1886–1890.

[115] Sun, T.; Mai, S.; Norton, D.; Haycock, J.W.; Ryan, A.J.; MacNeil, S. (2005). Self-organization of skin cells in three-dimensional electrospun polystyrene scaffolds. *Tissue engineering*, 11(7), 1023–1033.

[116] Li, W.J.; Laurencin, C.T.; Caterson, E.J.; Tuan, R.S.; Ko, F.K. (2002). Electrospun nanofibrous structure: A novel scaffold for tissue engineering. *Journal of Biomedical Materials Research*, 60(4), 613–621.

[117] Black, K.A.; Lin, B.F.; Wonder, E.A.; Desai, S.S.; Chung, E.J.; Ulery, B.D.; Katari, R.S.; Tirrell, M.V. (2015). Biocompatibility and characterization of a peptide amphiphile hydrogel for applications in peripheral nerve regeneration. *Tissue Engineering Part A*, 21(7-8), 1333–1342.

[118] Ulijn, R.V.; Smith, A.M. (2008). Designing peptide based nanomaterials. *Chemical Society Reviews*, 37(4), 664–675.

[119] Zisch, A.; Lutolf, M.; Ehrbar, M.; Raeber, G. (2003). Cell-demanded release of VEGF from synthetic, biointeractive cell ingrowth matrices for vascularized tissue growth. *The FASEB journal*.

[120] Cohn, D.; Sosnik, A.; Garty, S. (2005). Smart hydrogels for in situ generated implants. *Biomacromolecules*, 6(3), 1168–1175.

[121] Lin, C.C.; Raza, A.; Shih, H. (2012). PEG hydrogels formed by thiol-ene photo-click chemistry and their effect on the formation and recovery of insulin-secreting cell spheroids. *Biomaterials*, 32(36), 9685–9695.

[122] Aimetti, A.A.; Machen, A.J.; Anseth, K.S. (2009). Poly(ethylene glycol) hydrogels formed by thiol-ene photopolymerization for enzyme-responsive protein delivery. *Biomaterials*, 30(30), 6048–54.

[123] Karaca, N.; Temel, G.; Karaca Balta, D.; Aydin, M.; Arsu, N. (2010). Preparation of hydrogels by photopolymerization of acrylates in the presence of Type I and one-component Type II photoinitiators. *Journal of Photochemistry and Photobiology A: Chemistry*, 209(1), 1–6.

[124] Patterson, J.; Hubbell, J.A. (2010). Enhanced proteolytic degradation of molecularly engineered PEG hydrogels in response to MMP-1 and MMP-2. *Biomaterials*, 31(30), 7836–7845.

[125] Toepke, M.W.; Impellitteri, N.a.; Theisen, J.M.; Murphy, W.L. (2013). Characterization of thiol-ene crosslinked PEG hydrogels. *Macromolecular Materials and Engineering*, 298(6), 699–703.

[126] Tokuda, E.Y.; Leight, J.L.; Anseth, K.S. (2014). Modulation of matrix elasticity with PEG hydrogels to study melanoma drug responsiveness. *Biomaterials*, 35(14), 4310–8.

[127] Lutolf, M.P.; Lauer-Fields, J.L.; Schmoekel, H.G.; Metters, a.T.; Weber, F.E.; Fields, G.B.; Hubbell, J.a. (2003). Synthetic matrix metalloproteinase-sensitive hydrogels for the conduction of tissue regeneration: engineering cell-invasion characteristics. *Proceedings of the National Academy of Sciences of the United States of America*, 100(9), 5413–8.

[128] Fairbanks, B.D.; Schwartz, M.P.; Bowman, C.N.; Anseth, K.S. (2009). Photoinitiated polymerization of PEG-diacrylate with lithium phenyl-2,4,6-trimethylbenzoylphosphinate: polymerization rate and cytocompatibility. *Biomaterials*, 30(35), 6702–7.

[129] Li, C.Y.; Stevens, K.R.; Schwartz, R.E.; Alejandro, B.S.; Huang, J.H.; Bhatia, S.N. (2014). Micropatterned cell-cell interactions enable functional encapsulation of primary hepatocytes in hydrogel microtissues. *Tissue engineering. Part A*, 20(617), 2200–2212.

[130] Ki, S.C.; Shih, H.; Lin, C.C. (2013). Facile preparation of photodegradable hydrogels by photopolymerization. *Polymer (Guildf)*, 54(8), 2115–2122.

[131] Lin, C.C.; Ki, C.S.; Shih, H. (2015). Thiol-norbornene photoclick hydrogels for tissue engineering applications. *Journal of Applied Polymer Science*, 132(8).

[132] Ifkovits, J.L.; Burdick, J.a. (2007). Review: photopolymerizable and degradable biomaterials for tissue engineering applications. *Tissue Engineering*, 13(10), 2369–85.

[133] Nguyen, K.T.; West, J.L. (2002). Photopolymerizable hydrogels for tissue engineering applications. *Biomaterials*, 23, 4307–4314.

[134] Kloxin, A.M.; Kloxin, C.J.; Bowman, C.N.; Anseth, K.S. (2010). Mechanical properties of cellularly responsive hydrogels and their experimental determination. *Advanced Materials*, 22(31), 3484–3494.

[135] Lin, T.Y.; Ki, C.S.; Lin, C.C. (2014). Manipulating hepatocellular carcinoma cell fate in orthogonally cross-linked hydrogels. *Biomaterials*, 35(25), 6898–6906.

[136] Hoffmann, J.C.; West, J.L. (2013). Three-dimensional photolithographic micropatterning: a novel tool to probe the complexities of cell migration. *Integrative Biology*, 5(5), 817–27.

[137] Hahn, M.S.; Miller, J.S.; West, J.L. (2006). Three-dimensional biochemical and biomechanical patterning of hydrogels for guiding cell behavior. *Advanced Materials*, 18(20), 2679–2684.

[138] Mosiewicz, K.A.; Kolb, L.; Van Der Vlies, A.J.; Martino, M.M.; Lienemann, P.S.; Hubbell, J.A.; Ehrbar, M.; Lutolf, M.P. (2013). In situ cell manipulation through enzymatic hydrogel photopatterning. *Nature Materials*, 12(11), 1072–1078.

[139] Liu, V.L.; Chen, A.A.; Cho, L.M.; Jadin, K.D.; Sah, R.L.; DeLong, S.; West, J.L.; Bhatia, S.N. (2007). Fabrication of 3D hepatic tissues by additive photopatterning of cellular hydrogels. *FASEB Journal*, 21(3), 790–801.

[140] Heo, J.; Thomas, K.J.; Seong, G.H.; Crooks, R.M. (2003). A microfluidic bioreactor based on hydrogel-entrapped E. coli: cell viability, lysis, and intracellular enzyme reactions. *Analytical Chemistry*, 75(1), 22–6.

[141] Ikami, M.; Kawakami, A.; Kakuta, M.; Okamoto, Y.; Kaji, N.; Tokeshi, M.; Baba, Y. (2010). Immuno-pillar chip: a new platform for rapid and easy-to-use immunoassay. *Lab on a Chip*, 10(24), 3335–40.

[142] Beebe, D.J.; Moore, J.S.; Bauer, J.M.; Yu, Q.; Liu, R.H.; Devadoss, C.; Jo, B.h. (2000). Functional hydrogel structures for autonomous flow control inside microfuidic channels. *Letters to Nature*, 404, 588–590.

[143] Lim, H.L.; Hwang, Y.; Kar, M.; Varghese, S. (2014). Smart hydrogels as functional biomimetic systems. *Biomaterials Science*, 2(5), 603.

[144] Gonen-Wadmany, M.; Oss-Ronen, L.; Seliktar, D. (2007). Protein-polymer conjugates for forming photopolymerizable biomimetic hydrogels for tissue engineering. *Biomaterials*, 28(26), 3876–86.

[145] Kyburz, K.a.; Anseth, K.S. (2013). Three-dimensional hMSC motility within peptide-functionalized PEG-based hydrogels of varying adhesivity and crosslinking density. *Acta Biomaterialia*, 9(5), 6381–92.

[146] Weber, L.M.; Lopez, C.G.; Anseth, K.S. (2010). The effects of PEG hydrogel crosslinking density on protein diffusion and encapsulated islet survival and function. *Journal of Biomedical Materials Research*, 90(3), 720–729.

[147] Toomey, R.; Freidank, D.; Rühe, J. (2004). Swelling behavior of thin, surface-attached polymer networks. *Macromolecules*, 37(3), 882–887.

[148] Quesada-Pérez, M.; Maroto-Centeno, J.A.; Forcada, J.; Hidalgo-Alvarez, R. (2011). Gel swelling theories: The classical formalism and recent approaches. *Soft Matter*, 7(22), 10536–10547.

[149] Flory, P.J.; Rehner, J. (1943). Statistical mechanics of cross-linked polymer networks I. Rubberlike elasticity. *The Journal of Chemical Physics*, 11(1943), 512.

[150] Flory, P.J.; Rehner, J. (1943). Statistical mechanics of cross-linked polymer networks II. Swelling. *The Journal of Chemical Physics*, 11(11), 521–526.

[151] Flory, P.J. (1942). Thermodynamics of high polymer solutions. *The Journal of Chemical Physics*, 10(1), 51–61.

[152] Huggins, M.L. (1942). Some properties of solutions of long-chain compounds. *Journal of Physical Chemistry*, 46(1), 151–158.

[153] Huggins, M.L. (1942). Theory of solutions of high polymers. *Journal of the American Chemical Society*, 64(7), 1712–1719.

[154] Donnan, F.G. (1924). The theory of membrane equilibria. *Chemical Reviews*, 1(1), 73.

[155] Rička, J.; Tanaka, T. (1984). Swelling of ionic gels: quantitative performance of the donnan theory. *Macromolecules*, 17(12), 2916–2921.

[156] Goponenko, A.V.; Dzenis, Y.A. (2016). Role of mechanical factors in applications of stimuli-responsive polymer gels - Status and prospects. *Polymer (United Kingdom)*, 101, 415–449.

[157] Shibayama, M.; Tanaka, T. (1993). Volume phase transition and related phenomena of polymer gels. *Advances in Polymer Science*, 109, 1–62.

[158] Canal, T.; Peppas, N.a. (1989). Correlation between mesh size and equilibrium degree of swelling of polymeric networks. *Journal of Bomedical Materials Research*, 23, 1183–1193.

[159] Schwartz, M.P.; Rogers, R.E.; Singh, S.P.; Lee, J.Y.; Loveland, S.G.; Koepsel, J.T.; Witze, E.S.; Montanez-Sauri, S.I.; Sung, K.E.; Tokuda, E.Y.; Sharma, Y.; Everhart, L.M.; Nguyen, E.H.; Zaman, M.H.; Beebe, D.J.; Ahn, N.G.; Murphy, W.L.; Anseth, K.S. (2013). A quantitative comparison of human HT-1080 fibrosarcoma cells and primary human dermal fibroblasts identifies a 3D migration mechanism with properties unique to the transformed phenotype. *PLoS ONE*, 8(12).

[160] Fairbanks, B.D.; Schwartz, M.P.; Halevi, A.E.; Nuttelman, C.R.; Bowman, C.N.; Anseth, K.S. (2009). A versatile synthetic extracellular matrix mimic via thiol-norbornene photopolymerization. *Advanced Materials*, 21(48), 5005–5010.

[161] Dietrich, M.; Le Roy, H.; Brückner, D.B.; Engelke, H.; Zantl, R.; Rädler, J.O.; Broedersz, C.P. (2018). Guiding 3D cell migration in deformed synthetic hydrogel microstructures. *Soft Matter*, 14(15), 2816–2826.

[162] Son, K.H.; Lee, J.W. (2016). Synthesis and characterization of poly(ethylene glycol) based thermo-responsive hydrogels for cell sheet engineering. *Materials*, 9(10).

[163] Adrian, R.J. (2005). Twenty years of particle image velocimetry. *Experiments in Fluids*, 39(2), 159–169.

[164] Marel, A.K.; Zorn, M.; Klingner, C.; Wedlich-Söldner, R.; Frey, E.; Rädler, J.O. (2014). Flow and diffusion in channel-guided cell migration. *Biophysical Journal*, 107(5), 1054–64.

[165] Angelini, T.E.; Hannezo, E.; Trepat, X.; Marquez, M.; Fredberg, J.J.; Weitz, D.A. (2011). Glass-like dynamics of collective cell migration. *Proceedings of the National Academy of Sciences*, 108(12), 4714–4719.

[166] Vader, D.; Kabla, A.; Weitz, D.; Mahadevan, L. (2009). Strain-induced alignment in collagen gels. *PLoS ONE*, 4(6).

[167] Roca-Cusachs, P.P.; Iskratsch, T.T.; Sheetz, M.P.M.P. (2012). Finding the weakest link: exploring integrin-mediated mechanical molecular pathways. *Journal of Cell Science*, 125, 3025–3038.

[168] Doyle, A.D.; Yamada, K.M. (2015). Mechanosensing via cell-matrix adhesions in 3D microenvironments. *Experimental Cell Research*, 1–7.

[169] Hadjipanayi, E.; Mudera, V.; Brown, R.a. (2009). Guiding cell migration in 3D: A collagen matrix with graded directional stiffness. *Cell Motility and the Cytoskeleton*, 66(3), 121–128.

[170] Raeber, G.P.; Lutolf, M.P.; Hubbell, J.A. (2007). Mechanisms of 3-D migration and matrix remodeling of fibroblasts within artificial ECMs. *Acta Biomaterialia*, 3(5), 615–629.

[171] Johnson, B.D.; Beebe, D.J.; Crone, W.C. (2004). Effects of swelling on the mechanical properties of a pH-sensitive hydrogel for use in microfluidic devices. *Materials Science and Engineering C*, 24(4), 575–581.

[172] Anseth, K.S.; Bowman, C.N.; Brannon-peppas, L. (1996). Mechanical properties of hydrogels and their experimental determination. *Biomaterials*, 17(17), 1647–1657.

[173] Brau, R.R.; Ferrer, J.M.; Lee, H.; Castro, C.E.; Tam, B.K.; Tarsa, P.B.; Matsudaira, P.; Boyce, M.C.; Kamm, R.D.; Lang, M.J. (2007). Passive and active microrheology with optical tweezers. *Journal of Optics A: Pure and Applied Optics*, 9(8).

[174] Cicuta, P.; Donald, A.M. (2007). Microrheology: a review of the method and applications. *Soft Matter*, 3(12), 1449.

[175] MacKintosh, F.C.; Schmidt, C.F. (1999). Microrheology. *Current Opinion in Colloid & Interface Science*, 4, 300–307.

[176] Cuchiara, M.P.; Allen, A.C.B.; Chen, T.M.; Miller, J.S.; West, J.L. (2010). Multilayer microfluidic PEGDA hydrogels. *Biomaterials*, 31(21), 5491–7.

[177] Sears, C.; Kaunas, R. (2016). The many ways adherent cells respond to applied stretch. *Journal of Biomechanics*, 49(8), 1347–1354.

[178] Li, Y.; Huang, G.; Li, M.; Wang, L.; Elson, E.L.; Lu, T.J.; Genin, G.M.; Xu, F. (2016). An approach to quantifying 3D responses of cells to extreme strain. *Scientific Reports*, 6, 1–9.

[179] Storm, C.; Pastore, J.J.; MacKintosh, F.; Lubensky, T.; Jamney, P.A. (2005). Nonlinear elasticity in biological gels. *Nature*, 435(May), 191–194.

[180] Klebe, R.J.; Caldwell, H.; Milam, S. (1990). Cells transmit spatial information by orienting collagen fibers. *Matrix*, 9(6), 451–458.

[181] Raeber, J.; Lutolf, J.A.; Hubbell, G.P. (2008). Part II : Fibroblasts preferentially migrate in the direction of principal strain. *Biomech. Model. Mechanobiol.*, 7, 215–225.

[182] Eastwood, M.; Mudera, V.C.; Mcgrouther, D.A.; Brown, R.A. (1998). Effect of precise mechanical loading on fibroblast populated collagen lattices : Morphological changes. *Cell Motility and the Cytoskeleton*, 40(January), 13–21.

[183] Raeber, J.; Mayer, J.A.; Hubbell, G.P. (2008). Part I : A novel in-vitro system for simultaneous mechanical stimulation and time-lapse microscopy in 3D. *Biomech. Model. Mechanobiol.*, 7, 203–214.

[184] Wang, L.; Li, Y.; Chen, B.; Liu, S.; Li, M.; Zheng, L.; Wang, P.; Lu, T.J.; Xu, F. (2015). Patterning Cellular Alignment through Stretching Hydrogels with Programmable Strain Gradients. *ACS Applied Materials and Interfaces*, 7(27), 15088–15097.

[185] Foolen, J.; Deshpande, V.S.; Kanters, F.M.W.; Baaijens, F.P.T. (2012). The influence of matrix integrity on stress-fiber remodeling in 3D. *Biomaterials*, 33(30), 7508–7518.

[186] Winer, J.P.; Oake, S.; Janmey, P.A. (2009). Non-linear elasticity of extracellular matrices enables contractile cells to communicate local position and orientation. *PLoS ONE*, 4(7).

[187] Van Oosten, A.S.; Vahabi, M.; Licup, A.J.; Sharma, A.; Galie, P.A.; MacKintosh, F.C.; Janmey, P.A. (2016). Uncoupling shear and uniaxial elastic moduli of semiflexible biopolymer networks: Compression-softening and stretch-stiffening. *Scientific Reports*, 6, 1–9.

[188] Wen, Q.; Basu, A.; Janmey, P.A.; Yodh, A.G. (2012). Non-affine deformations in polymer hydrogels. *Soft Matter*, 8(31), 8039–8049.

[189] Wu, P.H.; Giri, A.; Sun, S.X.; Wirtz, D. (2014). Three-dimensional cell migration does not follow a random walk. *Proceedings of the National Academy of Sciences*, 111(11), 3949–3954.

[190] Rodríguez, D.; Morrison, C.J.; Overall, C.M. (2010). Matrix metalloproteinases: What do they not do? New substrates and biological roles identified by murine models and proteomics. *Biochimica et Biophysica Acta - Molecular Cell Research*, 1803(1), 39–54.

[191] Baker, A.H.; Edwards, D.R.; Murphy, G. (2002). Metalloproteinase inhibitors: biological actions and therapeutic opportunities. *Journal of Cell Science*, 115(19), 3719–3727.

[192] Chang, S.W.; Flynn, B.P.; Ruberti, J.W.; Buehler, M.J. (2012). Molecular mechanism of force induced stabilization of collagen against enzymatic breakdown. *Biomaterials*, 33(15), 3852–3859.

[193] Adhikari, A.S.; Chai, J.; Dunn, A.R. (2011). Mechanical load induces a 100-fold increase in the rate of collagen proteolysis by MMP-1. *J. Am. Chem. Soc.*, 133(6), 1686–1689.

[194] Adhikari, A.S.; Glassey, E.; Dunn, A.R. (2012). Conformational dynamics accompanying the proteolytic degradation of trimeric collagen I by collagenases. *J Am Chem Soc*, 134(32), 13259–13265.

[195] Wyart, M.; Liang, H.; Kabla, A.; Mahadevan, L. (2008). Elasticity of floppy and stiff random networks. *Physical Review Letters*, 101(21), 215501.

[196] Sheinman, M.; Broedersz, C.P.; MacKintosh, F.C. (2012). Nonlinear effective-medium theory of disordered spring networks. *Physical Review E - Statistical, Nonlinear, and Soft Matter Physics*, 85(2), 021801.

[197] Broedersz, C.P.; Mackintosh, F.C. (2014). Modeling semiflexible polymer networks. *Reviews of Modern Physics*, 86(3), 995–1036.

[198] Moschakis, T. (2013). Microrheology and particle tracking in food gels and emulsions. *Current Opinion in Colloid and Interface Science*, 18(4), 311–323.

[199] Yamaguchi, N.; Chae, B.s.; Zhang, L.; Kiick, K.L.; Furst, E.M. (2005). Rheological characterization of polysaccharide-poly(ethylene glycol) star copolymer hydrogels. *Biomacromolecules*, 6(4), 1931–1940.

[200] Kimble, H.; Barton, M.J.; Jun, M.; Park, S.; Nguyen, N.T. (2016). Cell stretching devices as research tools: engineering and biological considerations. *Lab Chip*, 16, 3193–3203.

[201] Arnold, M.; Cavalcanti-Adam, E.A.; Glass, R.; Blümmel, J.; Eck, W.; Kantlehner, M.; Kessler, H.; Spatz, J.P. (2004). Activation of integrin function by nanopatterned adhesive interfaces. *ChemPhysChem*, 5(3), 383–388.

[202] Balzer, E.M.; Tong, Z.; Paul, C.D.; Hung, W.C.; Stroka, K.M.; Boggs, A.E.; Martin, S.S.; Konstantopoulos, K. (2012). Physical confinement alters tumor cell adhesion and migration phenotypes. *FASEB Journal*, 26(10), 4045–4056.

[203] Rehfeldt, F.; Engler, A.J.; Eckhardt, A.; Ahmed, F.; Discher, D.E. (2007). Cell responses to the mechanochemical microenvironment-Implications for regenerative medicine and drug delivery. *Advanced Drug Delivery Reviews*, 59, 1329–1339.

[204] Laevsky, G.; Knecht, D.A. (2001). Under-agarose folate chemotaxis of Dictyostelium discoideum amoebae in permissive and mechanically inhibited conditions. *BioTechniques*, 31(5), 1140–1149.

[205] King, J.S.; Veltman, D.M.; Insall, R.H. (2011). The induction of autophagy by mechanical stress. *Autophagy*, 7(12), 1490–1499.

[206] Röttgermann, P.J.; Hertrich, S.; Berts, I.; Albert, M.; Segerer, F.J.; Moulin, J.F.; Nickel, B.; Rädler, J.O. (2014). Cell motility on polyethylene glycol block copolymers correlates to fibronectin surface adsorption. *Macromolecular Bioscience*, 14(12), 1755–1763.

[207] Théry, M.; Piel, M. (2009). Adhesive micropatterns for cells: a microcontact printing protocol. *Cold Spring Harbor protocols*, 2009(7).

[208] Pelham, R.J.; Wang, Y.L. (1997). Cell locomotion and focal adhesions are regulated by substrate flexibility. *Proc. Natl. Acad. Sci. USA*, 94, 13661–13665.

[209] Discher, D.E. (2005). Tissue cells feel and respond to the stiffness of their substrate. *Science*, 310(5751), 1139–1143.

[210] Wolf, K.; Wu, Y.I.; Liu, Y.; Geiger, J.; Tam, E.; Overall, C.; Stack, M.S.; Friedl, P. (2007). Multi-step pericellular proteolysis controls the transition from individual to collective cancer cell invasion. *Nature Cell Biology*, 9(8).

[211] Wolf, K.; Te Lindert, M.; Krause, M.; Alexander, S.; Te Riet, J.; Willis, A.L.; Hoffman, R.M.; Figdor, C.G.; Weiss, S.J.; Friedl, P. (2013). Physical limits of cell migration: control by ECM space and nuclear deformation and tuning by proteolysis and traction force. *The Journal of Cell Biology*, 201(7), 1069–84.

[212] Brown, M.A.; Wallace, C.S.; Anamelechi, C.C.; Clermont, E.; Reichert, W.M.; Truskey, G.A. (2007). The use of mild trypsinization conditions in the detachment of endothelial cells to promote subsequent endothelialization on synthetic surfaces. *Biomaterials*, 28(27), 3928–3935.

[213] Palecek, S.P.; Loftus, J.C.; Ginsberg, M.H.; Lauffenburger, D.A.; Horwitz, A.F. (1997). Integrin-ligand binding properties govern cell migration speed through cell-substratum adhesivness. *Nature*, 385, 537–540.

[214] Tse, J.M.; Cheng, G.; Tyrrell, J.A.; Wilcox-Adelman, S.A.; Boucher, Y.; Jain, R.K.; Munn, L.L. (2012). Mechanical compression drives cancer cells toward invasive phenotype. *Proceedings of the National Academy of Sciences*, 109(3), 911–916.

[215] Ben-David, U.; Siranosian, B.; Ha, G.; Tang, H.; Oren, Y.; Hinohara, K.; Strathdee, C.A.; Dempster, J.; Lyons, N.J.; Burns, R.; Nag, A.; Kugener, G.; Cimini, B.; Tsvetkov, P.; Maruvka, Y.E.; O'Rourke, R.; Garrity, A.; Tubelli, A.A.; Bandopadhayay, P.; Tsherniak, A.; Vazquez, F.; Wong, B.; Birger, C.; Ghandi, M.; Thorner, A.R.; Bittker, J.A.; Meyerson, M.; Getz, G.; Beroukhim, R.; Golub, T.R. (2018). Genetic and transcriptional evolution alters cancer cell line drug response. *Nature*, 560(7718), 325–330.

[216] Selvaggi, L.; Pasakarnis, L.; Brunner, D.; Aegerter, C.M. (2018). Magnetic tweezers optimized to exert high forces over extended distances from the magnet in multicellular systems. *Review of Scientific Instruments*, 89(4).

[217] Baudoin, R.; Corlu, A.; Griscom, L.; Legallais, C.; Leclerc, E. (2007). Trends in the development of microfluidic cell biochips for in vitro hepatotoxicity. *Toxicology in Vitro*, 21, 535–544.

[218] Li, Y.S.; Harn, H.J.; Hsieh, D.K.; Wen, T.C.; Subeq, Y.M.; Sun, L.Y.; Lin, S.Z.; Chiou, T.W. (2013). Cells and Materials for Liver Tissue Engineering. *Cell Transplantation*, 22(1), 685–700.

[219] Pasparakis, G.; Manouras, T.; Argitis, P.; Vamvakaki, M. (2012). Photodegradable polymers for biotechnological applications. *Macromolecular Rapid Communications*, 33(3), 183–98.

[220] Majima, T.; Schnabel, W. (1991). Phenyl-2,4,6-trimethylbenzoylphosphinates as water-soluble photoinitiators. Generation and reactivity of O=P(C6H5)(O-) radical anions. *Makromol Chem.*, 192, 2307–2315.

[221] Larsen, E.K.U.; Mikkelsen, M.B.L.; Larsen, N.B. (2014). Protein and cell patterning in closed polymer channels by photoimmobilizing proteins on photografted poly(ethylene glycol) diacrylate. *Biomicrofluidics*, 8(6), 064127.

Danke!

Ich bedanke mich bei allen die zur Entstehung dieser Arbeit beigetragen haben und mich in all den Jahren begleitet und unterstützt haben. Im Besonderen gilt mein Dank:

Joachim Rädler für die Betreuung meiner Doktorarbeit und die Diskussionen die mein Blick auf die grundlegenden Fragestellungen gelenkt haben und mich immer dazu anregten weiter zu denken.
Roman Zantl, für die Möglichkeit meine Arbeit in einem Unternehmen durchzuführen, die große Freiheit bei der Entwicklung dieser Arbeit und seinem stetem Interesse und wertvollem Input.
Chase Broedersz, der nicht nur die Zweitkorrektur meiner Arbeit übernimmt, sondern mir auch einen Einblick in die theoretische Physik gewährte. Danke für die sehr spannende Kooperation bei der ich viel gelernt habe.
Dem gesamten **Lehrstuhl Rädler**, der mir, obwohl ich meist bei ibidi war, das Gefühl gegeben hat dazu zugehören und mir bei jeglichen Fragen zu Abläufen an der Uni oder physikalischen Fragestellungen geholfen hat. Ich habe mich an der Uni immer sehr wohl gefühlt. Ein besonderer Dank auch an **Margarete** und **Margrit** die mir bei verwaltungstechnischen Fragen immer geholfen haben.
Meinen Bürokollegen an der Uni, **Alex, Daniel, Tobias, Judith, Benedikt, Matthias, Christoph, Anita, Sophia** und **Merlin**. Es lag bestimmt nicht an euch dass ich relativ selten vorbei geschaut habe.
Allen **ibidis** für die Unterstützung in den letzten Jahren. Sowohl der Produktion die mir Slides in rauen Mengen zur Verfügung gestellt hat, der Verwaltung die bei Fragen stets zur Stelle war, dem Vertrieb der mir so manchen Tipp gab und natürlich der Forschungs-/Entwicklungsabteilung mit der ich viel über meine Daten diskutieren konnte.
Meinen Bürokollegen bei ibidi, **Anita, Lena, Verena, Shokoufeh, Lea** und den vielen anderen Studenten die im Laufe der Jahre im Büro vorbei geschaut haben. Wir hatten immer eine tolle Atmosphäre, bei der weder Arbeit noch Spaß zu kurz gekommen sind.
Meinen Korrekturlesern **Verena, Anita, Christoph, Matthias** und **Sophia** ohne die wohl noch so mancher Fehler in der Arbeit stecken würde.
Außerdem **Hugo LeRoy** und **David Brückner** für die angenehme Zusammenarbeit bei dem theoretischen Model, **Hanna Engelke** für die Möglichkeit das Mikroskop

zu benutzen, **Max Albert** für die Herstellung der Chrommaske, **Johannes, Maxi, Daniel** und **Tobi** für die Unterstützung in allen IT Fragen, **Daniel Rüdiger** für seine Zeit bei den Rheometermessungen, **Kristian Franzes' Labor** in Cambridge für die Möglichkeit mein Hydrogelsystem auch mal in einem anderen Labor zu testen, **Lea** für die vielen Diskussionen über das mehr oder weniger erfolgreiche Polymerisieren von Hydrogelen und **Trung** für seine Hilfe mit dem TEng-Slide.
Allen **meinen Freunden**, die in der Freizeit für den nötigen Ausgleich gesorgt haben.
Meiner gesamten Familie für die immerwährende Unterstützung in allen Bereichen meines Lebens.
Und natürlich **meinem Mann**, der sich so manche Höhen und Tiefen in den letzten Jahren anhören durfte, mich immer unterstützt hat und mein steter Rückhalt im Leben ist.